UNIVERSITA' DEGLI STUDI DI VERONA

DEPARTMENT OF

DIAGNOSTIC AND PUBLIC HEALTH

GRADUATE SCHOOL OF

NATURAL SCIENCES AND ENGINEERING

DOCTORAL PROGRAM IN

NANOSCIENCES AND ADVANCED TECHNOLOGIES

XXXII cycle, 2019

TITLE OF THE DOCTORAL THESIS

ADVANCED NEUROIMAGING METHODS AND BIOMARKERS APPLIED TO PRECLINICAL MODELS OF MULTIPLE SCLEROSIS AND AMYOTHROPIC LATERAL SCLEROSIS

S.S.D. FIS/07

Coordinator: Prof. TAGLIARO FRANCO

Tutor: Prof. MARZOLA PASQUINA

Doctoral Student: Dott.ssa RACHELE PODDA

Index

48

Abstract

New paradigms are developed in magnetic resonance imaging for the advanced diagnosis of neurodegenerative diseases. In particular, multiple sclerosis (MS) and amyotrophic lateral sclerosis (ALS) preclinical research poorly focuses on functional connectivity in brain. Available animal models of MS and ALS are extensively used for analysis such drug testing and discovery of underlying mechanisms of pathogenesis. These diseases present, since neuronal lesions formation and neuroinflammation, a multilevel heterogeneity in mechanism of neurodegeneration and brain connectivity still not well understood. Moreover, they play a key role in pharmacological research, from the identification of a therapy target to the in vivo validation of the efficacy. More recently alterations in synchronized brain activity at rest in MS patients have been reported. At the best of our knowledge, functional imaging has not been applied yet in the assessment of new therapies in the preclinical models for MS and ALS. In this study, we aim to develop an innovative platform based on functional MRI in the resting state (rsfMRI), for the pre-clinical evaluation of new markers in MS and ALS. Moreover, the advancing in MRI techniques could assess new criteria of sensitivity and specificity in diagnosis; an additional analysis on diffusion MRI outcomes in MS preclinical models is added to this study.

Introduction

1. Advances in MRI for detecting markers in healthcare and research

The word *biomarker* is an umbrella term that depicts a "*characteristic that is objectively measured and evaluated as an indicator of normal biological processes, pathogenic processes, or pharmacologic responses to a therapeutic intervention*", as defined by the Biomarkers Definitions Working Group (NIH, 1998). This definition broadens as large as the progress in clinical and preclinical fields follows the discovery of new methods, instruments and analysis processes. A biomarker is everything that can be defined as robust, reproducible, and unambiguous, that is related to a clinical sign, or support a clinical accepted score in depicting a disease or establish a clinical onset.

They can be prognostic, diagnostic or acquired at specific timepoints. When clinical trials and research deal with diseases which effects are prolonged in time, or they are treated for the whole lifespan, new markers, named as surrogate biomarkers can be crucial to check therapies effects in trial phase and avoid false negative results from previously assessed measurement (Strimbu and Tavel, 2011).

Surrogates, by definition are " *laboratory measurement or physical sign that is used in therapeutic trials as a substitute for a clinically meaningful end point that is a direct measure of how a patient feels, functions or survives and is expected to predict the effect of therapy*" (Temple. 1999).

They were introduced because of the necessity to supplement relevant information due from other biomarkers; moreover new techniques in imaging could provide useful primary outcome measures. In magnetic resonance imaging (MRI), biomarkers are related to quantitative values derived from advanced methods of signal detection, or they are related to indirect measures that need to be correlated with other biomarkers, or other techniques. MRI provide in-vivo as well ex-vivo results; in one image is possible to investigate features of pathology, and it is possible to discover other findings related to a disease not only qualitatively, but also dynamically, i.e. across time.

MRI is well known as technique in check-ups and differential diagnosis when other instruments lack of resolution, to investigate or discriminate di per se tissues in details, non-invasively. MRI outcomes are also combined with other instruments, such as computerized axial tomography, single photon emission computer tomography, ultrasound imaging. In particular, the detection of pathological features in tissues, vessels or organs can be enhanced by means of specific contrast agents.

While other imaging techniques can achieve a preliminary diagnosis without MRI, following an event with poorly understood clinical signs, or with confounding symptoms at its acute stage, remains challenging. Moreover, it becomes crucial defining biomarkers and their surrogates also to assess the correct strategy for surgery and pathologies that need fast treatment. In addition, contrast agents normally used in clinics not always are specific and they do not determine directly the progress of diseases. Often the definition of biomarkers is oriented towards molecules that can interact with a treatment, or change during the progress of a disease; to date biomarkers are investigated on univocal “objects” that possess unambiguous features, or exhibit specific activity. Some antigen tests remain controversial (Hall, 2017), and not all the neuropathologies have clear markers in vivo.

Biomarkers related to functional brain decline are poorly correlated with other parameters for diagnosis. To note, in neurodegenerative diseases derived from autoimmunity or genetic mutation processes, clinical scores or endpoints in disability scale are the result of values from multiple tests. In particular, neuropathologies related to accidents (e.g. stroke), injuries (concussion), systemic inflammation (autoimmunity, viral infection secondary effect), iatrogenic effects (surgery) or aggressive treatments (radiotherapy, chemotherapy, immunomodulatory drugs), that lead to progressive neurodegeneration, are not well understood. Thus remains important to address efforts to prevent neurological disabilities in patients, as well as the research of new biomarkers that could state a difference between healthy and compromised nervous system, from different points of view. For example, neuroimaging techniques can assess the morphology, the microstructure, the microenvironment of the brain and its lesions (Tab.1.1).

Different metrics can be diffusion metrics within the tracts, counted number of tracks, connection probability between brain regions. In case of functional neuroimaging, metrics can refer for example to correlation coefficient, or quantify how signals covary between regions belonging to a particular functional network.

Method	**Neurodegenerative feature**				
	Neuronal/axonal loss	**Myelin disruption**	**Gliosis**	**Iron content**	**Connectivity**
T1 w	***Atrophy***; diameter, area, volumes, automated volume analysis				
T2 w	***Atrophy***		***Signal increase***	***Signal decrease***; R_2 increase	
NM-MRI	***Signal decrease***; volume, signal intensity				
MTI	MTR	MTR			
Diffusion imaging	MD, FA, AD, FW	FA, RD	MD, FW		Structural
Iron-sensitive sequences				***Signal decrease, anatomical structures*** (DNH); different metrics	
^{1}H-MRS	NAA, NAA/Cho, NAA/Cr	Cho			
rs-fMRI					Functional
ASL					Functional

Table 1.1 Adapted from Heim, Krismer et al, 2017. Qualitative markers are in italic, while their outcomes are in bold; Abbreviations: *AD* axial diffusivity, ASL arterial spin labelling; *Cho* choline, *rCBF* regional cerebral blood flow, *Cr* creatine, *DNH* dorsolateral nigral hyperintensity, *^{1}H-MRS* proton magnetic resonance spectroscopy, *FA* fractional anisotropy, *FW* free water, *MD* mean diffusivity, *MTI* magnetization transfer imaging, *MTR* magnetization transfer ratio, *NAA N*-acetylaspartate, *NM-MRI* neuromelanin-sensitive MRI, *R2* T2 relaxation rate, *R2** T2* relaxation rate, *RD* radial diffusivity, *rs-fMRI* resting-state functional MRI.

In preclinical research, when rodent central nervous system is main research focus, studies are conducted to discover features to assess if experimental therapeutic interventions are more successful in preventing and delaying disease, without clinical manifestation, heterogenic signs or before a true clinical outcome.

Nowadays neuroimaging neuropathology correlations can be improved by means of new computational methods. Image processing, as well as image analysis from different MRI methods can extract new useful metrics to understand clinical course of brain pathologies, both in human and rodents. The aim of the study reported in this manuscript is to assess robustness of new MRI techniques for different rodent models of pathologies with poor clinical signs at their prodromal stages in brain. In this study, early biomarkers in neuroimaging are investigated by means of different MRI methods. In particular, two available models of multiple sclerosis (MS) are used, to unravel immunity outcomes in mouse brain, i.e. if they can be clearly assessed with in vivo and ex vivo imaging. Moreover, also amyopthropic lateral sclerosis (ASL) model is taken in account to assess MRI markers, to understand the development of the disease in rodents brain.

1.2 MRI findings on Multiple Sclerosis and Amiotrophic Lateral Sclerosis

1.2.1 Multiple Sclerosis preclinical associated models

To compare, morphological biomarkers can measure longitudinally brain atrophy in multiple sclerosis and volumetric and numerical analysis of plaques, in T_2 and T_1 contrast enhanced imaging.

MS affects the central nervous system (CNS). This disease lead to myelin, oligodendrocytes, axons and neurons damage. Nowadays MS is considered as a generalized neurodegenerative process that involves not only the CNS. MS diagnosis follows assessed criteria (for a general disability scale and measures, see Uitedaag, 2018). Generally, MS is discovered because of deambulatory issues, optic nerve or spinal cord inflammation in patients, and confirmed with a MRI scout scan. Routinary imaging of the brain after the diagnosis is used to monitor the progression of this disease, but it does not exclude a cumulative neurodegeneration process. Original benchmarks to avoid false-positive diagnosis rely in cerebrospinal fluid, combined to the assessment of brain lesion across time and space (Polman, Stephen et al, 2005). Moreover, it can be distinguished in relapsing-remitting and chronic MS, thus the need to eliminate alternative conditions persist, by means of differential diagnosis. Biomarkers are used to assess MS and exclude for example, neuromyelitis optica, by means of specific serum antibody (Lennon V, Wingerchuk D, et a., 2005). MS diagnosis, considering revised criteria, is satisfied with at least one gadolinium-enhancing lesion or nine T_2 hyper-intense lesions without gadolinium enhancing. Also infratentorial, juxtacortical lesion, with at least three periventricular lesions are added to demonstrate dissemination of lesion in space (Barkhof, Filippi M, Miller DH, et al., 1997; Tintoré, Rovira, Martinez, 2000). These criteria open considerations on other MRI findings, also incorporating spinal cord imaging, that can be used as criteria for the disease assessment in time. New techniques focuses on sensitivity and specificity, such as diffusion weighted imaging, and functional connectivity in the brain as non-invasive inspection of changes in normal, healthy brain activity.

Main used preclinical models for MS are based on experimental autoimmune encephalomyelitis (EAE) development. They can be classified accordingly to method used to induce the disease. Major EAE induced in mice used are myelin oligondendrocyte (MOG) mediated by pertussis toxin, PLP protein mediated, adoptive cell transfer (for a general overview, see Hart, Ganz and Weissert, 2011) EAE toxic demyelination cuprizone is extensively used for myelin damage studies (Torkildsen et al., 2008).

The interaction between the immunopathological and neuropathological features permits to consider different approximative mimicking MS EAE models across laboratory species.

Induced EAE in mice shares features that are related to human outcomes in MS condition; these are inflammation, demyelination, axonal degeneration and gliosis. Up to date, these processes are still investigated. For example, inflammatory demyelination is not directly implied in perilesional axonal damage (Singh, Dallenga, Winkler et al., 2017), or axon transection in EAE is restored by reactive oxygen species and nitric oxide species (ROS/NOS) scavengers (Sorbara, Wagner, Ladwig et al., 2014). Moreover, in humans CD8 cells drive the autoimmune disease in MS, while CD4 are the major infiltrates in EAE model. Thus this "immunological" gap, as well the susceptibility to EAE induction and the response variability, suggest to focus on to the specific aspects of tailored preclinical model, to improve the selection of therapies. Moreover, if immunological aspects of each EAE model used were clarified, not all the treatments were successfully translated to humans (Segal, 2008) and some therapies with the progression of MS decay in efficacy (Hemmer, Mulau, 2016).

The variability in EAE neuroimmunology creates an opportunity to explore in a different manner inflammation and de-myelination. The possibility to robust clinical scores, with a standardized method, has brought research efforts towards the analysis of all the weaknesses inherent to EAE models from the immunological point of view, more than focusing on intrinsic protective mechanisms and brain dysfunctions in rodents.

EAE mice models have been investigated by means of other MRI techniques, such as magnetization transfer ratio (Aharoni, Sasson et al, 2013), voxel based morphometry (Hamilton, 2019), T_2 weighted imaging with contrast agent (Belloli, Zanotti, Murtaj et al., 2018). Diffusion imaging, as well as functional and resting state MRI methodologies are used in human studies (Cortese, Collorone, Cicarelli et al, 2016), but at the time this study started no reports in EAE mouse brain use resting state functional imaging at low magnetic field, or ex-vivo diffusion imaging at higher magnetic field. MRI investigation on EAE models are conducted both in-vivo and ex-vivo, to investigate myelin damage during the disease course. A summary of MRI on EAE cuprizone model highlight also some ex-vivo structural study, but a majority of papers focused on some regions, such corpus callosum, cingulate and cortex. (Tab. 1.2). At the time of this work, ex-vivo MRI in EAE mice is poorly investigated, but research in neuroimaging values focused on myelin change during the disease is still ongoing. All aim to detect disease biomarkers, or retrospective metrics, in human MS, especially to monitor lesions course.

Reference	***In-/Ex-vivo***	***Acquisition***	***Analysis***	***Methods***
Chandran et al. (2012)	*In*	*MS*	*CC, Cg, EC*	*T2w, DTI*
Falangola et al. (2014)	*In*	*MS*	*CC*	*DKI*
Fjær et al. (2013)	*In*	*3D*	*CC, GM, Cbl, Ctx*	*T2w, MTR*
Guglielmetti et al. (2016)	*In*	*MS*	*CC, Ctx*	*T2w, DKI*
Jelescu et al. (2016)	*In*	*SS*	*CC*	*T2w, MTR, DKI*
Merkler et al. (2005)	*In*	*3D*	*CC, EC*	*T1w, T2w, MTR*
Song et al. (2005)	*Ex*	*MS*	*CC, EC, OT, CP*	*DTI*
Sun et al. (2006)	*In*	*MS*	*CC*	*DTI*
Tagge et al. (2016)	*In*	*3D*	*Cbr*	*T2w, MTR*
Thiessen et al. (2013)	*Both*	*SS*	*CC, EC, Ctx*	*T1/2, qMT, DTI, MWF*
Torkildsen et al. (2009)	*In*	*MS*	*Lesion volumes*	*T2w*
Turati et al. (2014)	*In*	*SS×2*	*CC, EC*	*qMT*
Wood et al. (2016)	*Ex*	*MS*	*CC, Cbl*	*T1w,T2w, DTI, MWF*
Wu et al. (2008)	*In*	*MS*	*CC*	*T2w, DTI*
Xie et al. (2010)	*In*	*MS*	*CC*	*DTI*
Zhang et al. (2012)	*Both*	*3D/MS*	*CC, Ctx*	*T2w, MTR, DTI*

Tab.1.2. Review of cuprizone mice volume analysis and MRI methods. adapted from Wood, Simmons et al., 2016. Cbl, Cerebellum; Cbr, Cerebrum; CC, Corpus Callosum;

EC, External Capsule; Ctx, Cortex; Cg, Cingulum; DKI, Diffusion Kurtosis Imaging; DTI, Diffusion Tensor Imaging; CP, Cerebral Peduncles; MS, Multi-slice; MTR, Magnetisation Transfer Ratio; MWF myelin water fraction; OT, Optic Tracts; qMT, Quantitative Magnetisation Transfer; SS, Single-slice; T1w, T_1 Weighted; T2w, T_2 Weighted; T1, T1 Map; T2, T2 Map;

1.2.2 Amyotrophic lateral sclerosis (ALS) preclinical associated models

ALS is a neurodegenerative disease that involves the motor neuron, a network in CNS that involves spinal cord and primary motor cortex in brain. Neuropathological outcomes are degeneration of upper and or lower motor neurons. Onset symptoms refers to progressive weakness and progressive paralysis of other muscular districts also involved in breathing, causing ALS to be a fatal and incurable disease (Mitchell and Borasio, 2007). Moreover, other symptoms related to ALS are associated to extra-motor areas in brain, such as behavioural and cognitive changes, with concomitant psychiatric disorders observed at the onset of the disease (Zucchi, Ticozzi and Mandrioli, 2019).

Is it widely recognized that ALS bear autonomic and extra-motor disabilities and this diagnosis is distinguished in subtypes, with shared symptoms with fronto-parietal dementia and parkinsonism (Talbot et al., 1995; Neary, Snowden, Mann, 2000). Pure motor neuron involvement is overcame by clinical, pathological and genetic features of ALS, that should be considered as a multisystem disorder.

In ALS, to date, only electromyography supports the diagnosis, while animal models have not been able to predict response to emerging treatments in humans, but clinical endpoints in MRI have been explored in research, by means of functional MRI (fMRI), diffusion imaging, without replication in larger cohorts and in absence of symptoms (Menke, 2017).

Despite ALS has sporadic etiology, a part of patients inherits a familial form that is related to a gene encoding superoxide dismutase 1 protein (SOD1, see Fridovich, 1986). Human Cu-Zn superoxide dismutase mutation differs from binding site expression (Wang, Xu, Gonzales et al, 2002).

Different animal models can reproduce ALS features. They can be subdivided in different phenotypes and carry mutations such as fused in sarcoma RNA-binding protein *FUS*, *SOD1*, *TARDBP*, ubiquilin 2 - *UBQLN2*, VAMP-associated protein B - *VAPB* and valosin-containing protein – *VCP*.

Also there are other physiological ALS models, obtained by means of mutagen N-ethyl-N-nitrosourea (ENU, Joyce et al., 2014) (Tab.1.3).

Gene mutation	**Clinical outcomes in mice**	**Reference**
FUS Delta14	MN loss, diffuse MW	Devoy et al., 2017
SOD1(93A)	MN loss, diffuse MW, end stage paralysis	Gurney et al., 1994
UBQLN2	MW,forelimb/hind atrophy	Deng et al., 2011
VAPB	MN loss, MW, forelimb/hind atrophy, end stage paralysis	Nishimura et al., 2004
VCP	MW, forelimb/hind atrophy	Yin et al., 2012

Table 1.3. Schematic reference showing pathology in ALS models related to carried mutated gene. MW: muscle weakness, MN: motor neuron.

The first transgenic line and most studied ALS model is from mouse carrying a point mutation in amino acid position 93 of the SOD-1 protein (93A) (Gurney, Pu, Chiu et al., 1994), with a life expectancy up to 150 days.

MRI on SOD (93A) focused on spinal cord structural changes (Fogarty, Mu, Noakes et al., 2016), or diffusion properties (Niessen, Angenstein, Sander et al. 2006). Also research focused on brainstem at 4.7T magnetic field, from morphological point of view (Zang, Yang, Wang et al., 2004), and T_2 relaxation time (Bucher, Braunstein, Niessen et al., 2007). T_2 weighted imaging has already shown its potential as biomarker in pre-symptomatic mice at motor , hypoglossal and facial nuclei lesion enhancement (Evans, Serres, Khrapitchev et al. 2014), and correlates with diffusion tensor imaging metrics associated to histological findings of vacuolization and cranial motor neuron T_2 hyperintensity (Caron, Micotti, Paladini et al. 2015).

Up to date, also behavioural studies were conducted on SOD93A, without imaging or functional connectivity investigation (Kreilaus , Guerra , Masanetz et al., 2019).

With these assumptions, new biomarkers in rsfMRI can be explored as pre-emptive findings in such pathologies to a better understanding of the SOD93A animal model comparable to ALS.

To a better understanding of MRI methods used, the basic principles and methods are further discussed, as well as how they are applied to three different neuropathological disease models.

1.3 Principles of MRI

The first human body scan was proposed by Damadian in 1971, while the MRI technique was initially named zeugmatography (Lauterbur, 1975), leading to the physical basis of non-invasive in-vivo structural analysis of soft tissues. The MRI instrument is a combination of different units. It can be subdivided as follows:

a) static magnetic field, that is conventionally fixed along z-axis;
b) x, y, and z-gradients coils and amplifiers, that apply linear magnetic fields along space directions
c) a shim unit, to avoid field inhomogeneities during the acquisition;
d) radiofrequency electronics block, coupled with an analogic to digital converter;
e) computer, operator controlled and latest display of the generated signals (Fig.1).

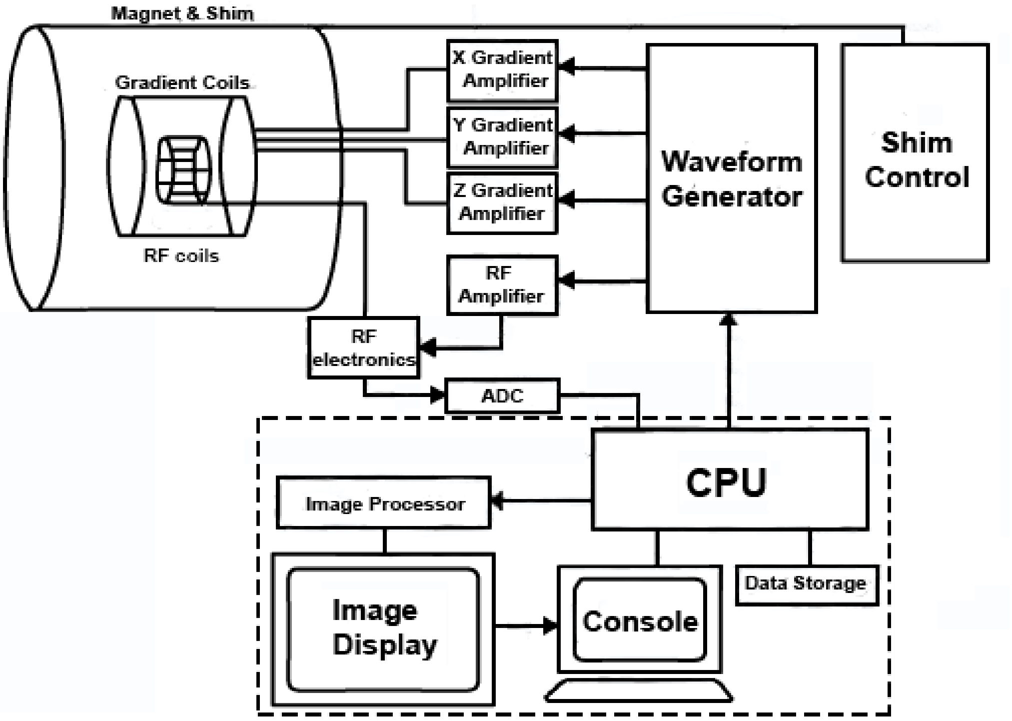

Figure 1.1 Schematic representation of a MRI scanner (tomograph). Adapted from https://www.rdm.ox.ac.uk/.

MRI relies in quantomechanics principles, applied first in biochemistry and organic chemistry (for extensive explanations, see Keeler, 2005 and Levitt, 2008). This permits the fine detection of nuclei with determined gyromagnetic ratio, especially hydrogen protons because of higher abundance in biological samples, when they are subjected to a fixed magnetic field along an axis. The phenomenon of resonance occurs if radiofrequency excitation pulse satisfies Larmor equation. Emitted or absorbed energy by atomic nuclei is registered and specific signals rise in the frequency spectra. If field gradients are applied in time coincidence with a proper radiofrequency pulse to a sample in a fixed magnetic field, nuclear species from the sample change their magnetizations, that later decay to reach the energetic equilibrium. The time constants for this decay processes phenomena are named relaxation times, T_1 and T_2 respectively. Relaxation times properties give the possibility to differentiate various tissues in the body, i.e. generate contrast, that is affected also by magnetic field strength, temperature and signal to noise ratio (SNR). The constant magnetic field power is expressed in Tesla units (T); for humans, the most used electro-magnet has a field of 1.5 T or 3T, valuable for clinical purposes, while research combines also human scanners with 7T field. For preclinical research, more options are available, from 7 T up to 16.1 T systems dedicated to rodents, non-human primates mostly, for high-resolution images.

A good tissue contrast is achieved by means of an appropriate pulse sequence. Major parameters to set for the MRI acquisition are the repetition time (TR), echo time (TE), flip angle and inversion time. Briefly, the combination of set TR, TE, flip angle are required to acquire MR signal. TR is the amount of time between first RF pulse and the same repeated and applied to the selected slice, while TE is crucial for the measurement of spins in phase, because it is the time between the 90° RF pulse and MR signal sampling, corresponding to maximum of the echo. TE is a value between the 90° excitation pulse and echo peak given by excited nuclei, expressed in milliseconds. Inversion time is set for water and fat suppression and it represents the period between an inversion pulse of 180° (when macroscopic magnetization is not aligned to the constant magnetic field, named refocusing pulse) and the 90° pulse. Flip angles values define the rotation of net magnetization to the main magnetic field. Signal values are dependent of flip angle also: for example, for a T1 weighted image, a small flip angle maintains the longitudinal magnetization, while the in-plane (z) magnetization is tilted in the x-y planes. If the TR is short, the z-magnetization cannot fully recover. As the result of preselected parameters, the free induction decay signal (FID) is acquired and processed by the analogic to digital converter. Planes in a selected slice are defined as phase encode and frequency encode. The frequency encoding is dependent from FID sampling, while the final resolution of the image is dependent from the matrix size, magnetic field strength and voxel size. To a better understanding of events occurring inside the scanner, an MRI experiment can be decomposed in the pulse diagram (Collins, 2016, for in-depth fundamentals).

The MR image is the result of a Fourier transform of the varying signals, in the temporal domain, that are decoded back into the frequency domain. When magnetic gradients are applied, they cause a phase shift of the protons involved, upon the proton RF. The generated signal can be located and encoded in two dimensions. Unprocessed signal is stored in the k-space, a formalism introduced to indicate a matrix in which the k-x axis contains the frequency data sets and the k-y axis the phase encoded ones (Likes, 1979; Twieg & Ljunggren, 1983).

The sample is scanned along three directions, and sliced in volumes, with the same length. This means that the obtained image contains informations not only of the acquired MR signal, but also about spatial resolution, data size, field of view (FOV). The spatial resolution of an image is defined by voxels. Voxels can be imagined as solids in which the depth is represented by the slice thickness. Data size is defined by matrix size (MTX), and it is dependent from frequency encoding step number. FOV is the covered area by phase matrix and frequency encoding. In-plane voxel size is obtained dividing the FOV by the matrix size. Thus means that resolution decreases when the voxel size increases, and when FOV increases in both directions.

Depending on the metrics that can be obtained from contrasts, a variety of sequences is available for in-vivo and ex-vivo imaging.

1.3.1 MRI sequences

Mostly used pulse sequences can be inserted in two MRI macro group methods, namely spin and gradient echo imaging. All methods achieve echoes, i.e. the energy emitted by nuclei after excitation, as magnetic resonance signal, translated after in an image.

Spin echo or multi-echo sequences are used for anatomical imaging, tissue morphology and qualitative abnormalities during pathologies. Susceptibility artifacts or noise are lowered by means of one or more 180° RF pulses, after the 90° pulse. Spins are refocused, generating signal echoes. Methods can vary accordingly to instrument manufacturing or commercial implementation. For example, fast or turbo spin echo sequences include the Rapid Acquisition with Refocused Echo (RARE, Hennig et al., 1986).

In the same group, multi echo imaging permits to measure the T2 relaxation time. The sequence used is a spin echo, multi echo multi slice (MEMS).

Gradient echo imaging, instead of spin echo, lacks of 180° refocusing pulse, because of magnetization tilting by a flip angle between 0 and 90°. An echo is generated by means of bipolar gradient pulses, because of spin dephasing by applying a negative pulse gradient, followed by spin rephasing, achieved by an applied opposite gradient. T_2 weighted imaging by GE are more sensitive to field inhomogeneities, compared to SE.

A GE sequence weighted in T_1 is the three dimensional Magnetization Prepared Rapid Acquisition Gradient Rapid Echo (3D MPRAGE). It is an inversion recovery sequence (by an applied 180° inversion pulse) followed by a GRE imaging sequence, in which a secondary phase encoding, towards slice selection direction, is introduce to produce 3D images. In this case, higher magnetic fields, respect to transmitted field, cause spatial inhomogeineities that are corrected with double imaging and two inversion times, namely MP2RAGE (Marques et al., 2010). Inversion time is used for fluid suppression, or T_1 weighted images.

The earliest GE sequence, nowadays applied for diffusion, perfusion and functional MRI, was developed to achieve Echo Planar Imaging (EPI), (Stehling, Turner and

Mansfield, 1991) and it is characterized by a periodic frequency encoding gradient reversing.

The short sequence time permits faster data acquisition, that is with one TR the possibility to fill k-space lines, while other pulse programs utilize also phase encoding step for signal sampling. Drawbacks are related to image resolution, which is dependent from ramp gradient sampling. The machine requires high field strength and good hardware; major artifacts are due to gradients, as phase accumulation across the scheme sequence, and the results are not only in image distortion but also the water fat shift in the phase encoding direction. This method is useful in brain and other techniques that requires fast imaging, such as functional MRI in humans and small animals.

1.3.2 Functional MRI

Functional MRI (Amaro & Barker, 2006) is a method to see where neural activity is present, using protocols with fast scanning at low space resolution. This technique is used to determine insights in both basic workings and malfunctions of the brain, and represents an innovative approach in experimental psychology and neurophysiology. The monitored brain response by fMRI has been extended to other purposes, enabling the possibility of investigated activated areas of the brain with specific spatial localization. It is important to recall that the interaction between gradients and neuroimaging has to be considered, i.e. artifacts generated by sequence used, head movement, cerebral blood flow.

Brain perfusion changes result in observable alterations in the distribution of de-oxyhemoglobin/haemoglobin in the red blood cells. The contrast generated in MRI, is named blood oxygenation level dependent (BOLD): working tissues “dissolve” CO_2 when working, thus low pH environment leads to positive charge in the histidine-heme complex, with consequent oxygen release in the bloodstream. This paramagnetic effect was observed in brain vessels (Ogawa, 1990). The MRI contrast is dependent from the different magnetic susceptibility of blood inside the vessels, which is non-parallel oriented to the static magnetic field. The overall processes, in GE sequences, generates effects in the water signal, which is detected

as contrast in brain. Therefore BOLD contrast is related to the hemodynamic response and neuronal activity can be monitored by MRI (Logothetis et al., 2001). Studying the already know mechanism of neurovascular coupling, local variation of blood supply can be correlated to anatomical regions. The structural part in an fMRI experiment is provided by a T_2w high resolution image of the same subject.
If it is easier to distinguish a difference in hemodynamic response between task-evoked imaging and rest-imaging, because the latter one informs about the first, and it is demonstrated that increased brain activity corresponds to a higher oxygen demand, that results in MRI initial signal attenuation (dip) followed by an increase. The susceptibility between blood and tissue changes because of different ratios of oxygenated and de-oxygenated blood (fig.1.2).

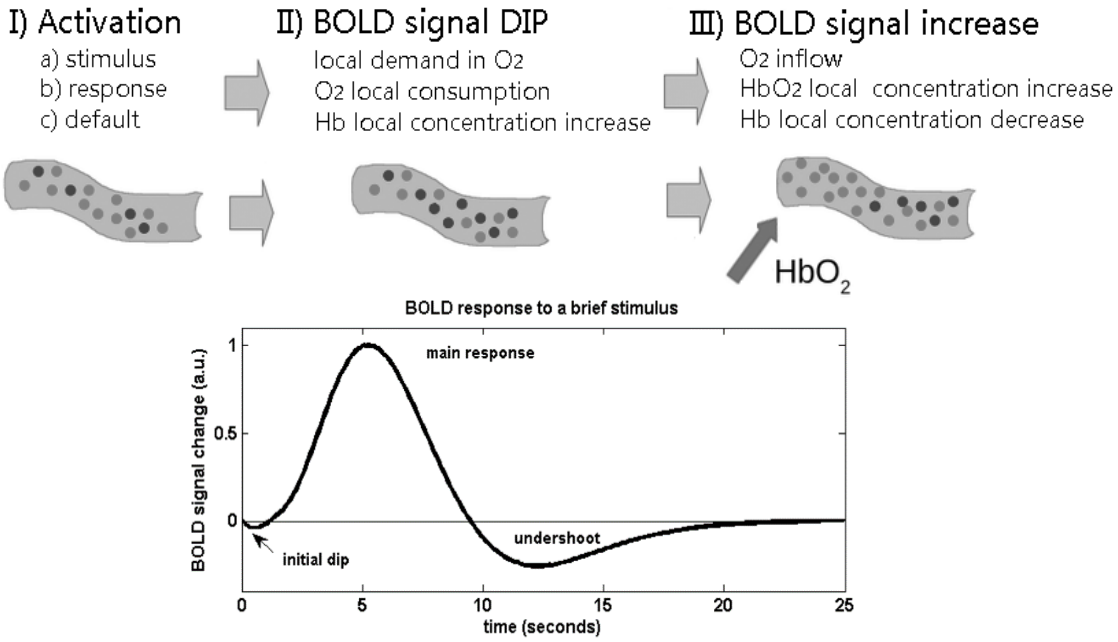

Figure 1.2. Bold effect (adapted from Barth, Poser, 2011); I, II, III corresponds to BOLD response steps in change. HbO2 oxigenated haemoglobin, Hb de-oxygenated haemoglobin.

The origin of resting state functional MRI (rsfMRI) has derived from BOLD signal noise source studies and vascular variability investigation in brain, in fMRI paradigms. Resting state functional connectivity was observed first in humans (Biswal, 1995).

The hypothesis of common hemodynamic “substrate” both in task and rest imaging was assessed focusing on sensorimotor cortex, that exhibited a constant activity correlated to visual and auditory cortices tract (Hampson, 2002).

RsfMRI is based in BOLD contrast also, but studies the low signal fluctuations in brain activity, with frequencies in the range of 0.01-0.02 Hz, that can observed during cognitive task or neurological/psychiatric disorders.

Moreover, long-range connection between functional areas are related to resting state, and both positive and negative correlations between regions showed spontaneous low frequencies, even if not anatomically correlated; one latter hypothesis is related to neuron subsets and Na+/K+ ion concentrations, that produce membrane voltage fluctuations (Krishnan, González and Bazhenov, 2018).

To investigate the brain from the functional point of view can provide new findings about neuronal networks at long scale level. Studies that benefits from rsfMRI outcomes are related to behaviour, neurosciences applied to psychology, or neurodegenerative diseases with non evident signs at prodromal stage, i.e. ALS, (Ogura, Watanabe, Kawabata, 2019) and Parkinson (Westphal, Simmons 2017; Chen, 2015) (Heim, De Marzi, Seppi, 2017).

Since the first studies conducted on resting state, basal brain activity can be subdivided in networks, that are anti-correlated one to each other. A major hypothesis consider an intrinsic brain network and an extrinsic one, but they are not always equivalent and they do not always correlate when task are performed (Mennes, Kelly, Colcombe et al., 2013). The intrinsic network corresponds to default mode network (DMN), that is present also in rodents (Stafford, Jarrett, Dominguez et al., 2014).

From module stability maps in resting state experiments from a high cohort of C57 mice, functional hubs were extracted from brain. Anatomically, they can be distinguished in default mode network (Retrosplenial cortex, cingulate area, tegmental area, prefrontal cortex are involved), lateral cortical (somatosensory lateral area; motor area; frontal area), hippocampal (ventral and dorsal gyrus of hippocampus; thalamic portion and dentate gyrus of hippocampus), Basal forebrain (sensorimotor area, nucleus accumbens); Ventral Midbrain network (comprehends tegmental decussation, Amygdala, Hypothalamus) and Thalamic network (ventral thalamic area).

Interestingly, the DMN is connected more than the lateral cortex network, with other hubs of connectivity. Thus means that the two modules can be considered as two major intrinsic and extrinsic networks as in human brain, to be further investigated (Liska, Galbusera, Schwarz et al., 2015).

2. Materials and Methods

This chapter covers in detail all methodologies used for the performed studies. In particular, it is subdivided in different sections that specify in detail animal modesl used, MRI modality and analysis. Each sub-sections can be referred to the results reported in chapter n.3. Reagents are reported in the appendix of this thesis. All experiments performed are reported in figure 2.1 for a better understanding. MRI methods used for each study were followed by different image analysis procedures.

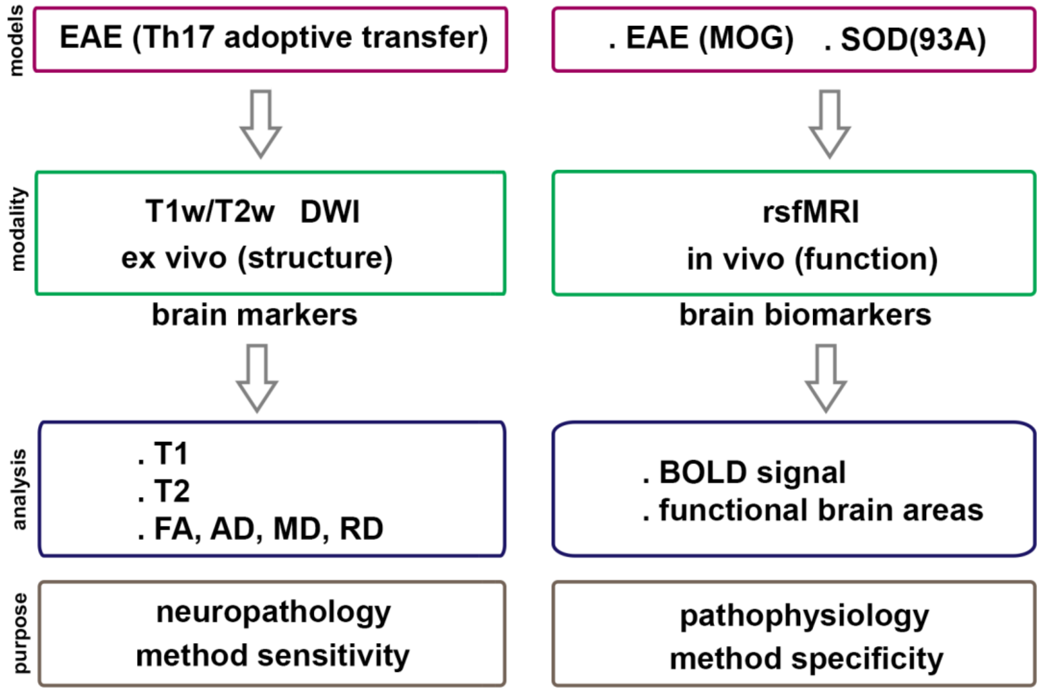

Fig.2.1 Workflow for each study, purple boxes represents available models, used methods in green boxes, analysis of different outcomes in MRI are shown in blue boxes, while main purpose is in grey boxes; to note, each mouse model was studied with the same number of controls (2). AD, axial diffusivity; BOLD blood oxygen level dependent signal, EAE, experimental autoimmune encephalitis T cell 17 mediated; EAE (MOG), experimental autoimmune encephalitis - myelin oligodendrocyte glycoprotein mediated; FA fractional anisotropy, MD, mean diffusivity, RD, radial diffusivity; rsfMRI, resting-state functional MRI; T1 relaxation time, spin-lattice; T2 relaxation time, spin-spin.

2.1 EAE induction by Th17 adoptive transfer

2.1.1 Selection of 2D2 positive mice for cell extraction

For the EAE induction in C57BJL6 mice, T-helper 17 cells from 2D2 positive mice were intraperitoneally (i.p.) injected at the clinical neuroscience site in the Centre Hospitalier Universitaire Vaudoise Facility (Epalinges site, Lausanne, CH). Mice colonies were obtained from 2D2/BJ6 starting couples (Jackson Laboratories), crossed with C57BlJ6 wild type strain. Newborn at 1 month of age were genotyped by means of flow cytometry. This immunofluorescent staining assay on red blood cells (RBC) is an alternative method, instead of DNA extraction, because of the free availability of a cytometer inside the facility (BD FACS LSR II Diva, Bethesda, US). Two drops of blood for each subject were collected by means of submandibular punction, with sterile lancets (Goldenrod, GR 4mm, Braintree scientific, US), in ethylene-diamine-tetra-acetic acid (EDTA) tubes, and immediately transferred in Eppendorf tubes containing 100 uL of RBC lysis Buffer 1X. Tubes were spinned at 4°C and kept in ice. Some blood drops were kept for unstained control. After a centrifugation at 400g for 4’, lysis was stopped by adding 200 uL of PBS and the cells were spinned again at 400G for 4’. The supernatant was discarded and the pellet was first re-suspended in 50uL of lysis buffer and transferred in FACS plate for an incubation of 5’ at room temperature. Lysis was immediately stopped by adding 100ul of PBS 1x and the whole content was spinned at 400G for 4’. Supernatant was again removed by pipetting and cell pellets were re-suspended in 10µL blocking solution, made with blocking agent (purified antimouse monoclonal antibody CD16/32, eBioscience, in 1/100 in FACS buffer) and samples were incubated on ice for 15‘ prior to immunostaining. The antibody is responsible for blocking CD16/CD32 interactions with the Fc domain, named also receptors, of immunoglobulins and is specific to the common epitope of CD16/CD32. It is used for blocking non-specific binding of immunoglobulin to Fc receptors. (Buchwalow, 2011).

Antibody mix for surface staining was added to the sample, for each mouse, for the amount of 10uL volume in FACS wells, that contained the conjugates to detect CD4 expression with the associate integrin: CD4-PE and V3α3.2-APC, in dilution 1/100 respectively. The FACS plate was kept for 15 minutes on ice, away from the light, then it was spinned at 400G for 4 minutes. The surnatant was removed and for each well was added paraformaldeylde (PFA) 1% on phosphate buffer saline (PBS) at pH 7, for 30 minutes on ice. The last step before flow cytometry consisted in centrifugation again at 400G for 4', a FACS buffer wash of the plate, followed by spinning the sample at 400G for 4'. After surnatant removal, pellet was resuspended in 200uL FACS buffer. After FACS qualitative analysis, mice were splitted in new cages and classified as 2D2 positive and 2D2 negative in order to obtain CD4 cells that exhibits encephalopathogenic properties after correctly polarization.

2.1.2 In vitro differentiation and proliferation of effector T-cells

To obtain effector T cells, two signals are required. The first one is provided by means of interaction of TCR/CD3 complex with major histocompatibility complex (MHC) molecule: to present this, in the cellular colture specific antibodies are added. The second signal is co-stimulation, provided via interaction of specific cluster of differentiations (CDs) and interleukins of T cells with other CDs from antigen presenting cells. Freshly isolated splenocytes contains 1-2% of myeloid derived dendritic cells (DC). DC express CD80 constitutively, thus representing the best adapted to perform functions of antigen presenting cells (APCs). After DC irradiation, they remain live in the culture during several days. DCs bind anti-CD3 antibodies via Fc-receptors, thus T cells in the culture are with both ligands, necessary for activation. After 1 to 2 hours, T cells will be express CD40L on them because of the signal given by the interaction of TCR/CD3. Interacting with CD40 on the APCs, this ligand induces additional expression of CD80 and CD86 on APCs, including the ones which did not express CD80 and CD86 before. CD40/CD40L interaction turn on production of anti-apoptotic molecules in APCs, allowing their better survival in culture. CD28 co-stimulation induces production of anti-apoptotic molecules, IL-2 and CD25 in T lymphocytes. CD25 expression has a role in the formation of receptors with high affinity to IL-2 in T cells proliferation of T cells becomes more autonomous and less dependent from co-stimulation for at least 48 hours. These processes take place in CD4 and CD8 T cells. In order to obtain CD4 T cells, because this process affects also CD8 cells, CD4 are isolated and re-stimulated to reach T-helper 17 status. The molecular requirements and the methods from naïve cells are summarized in figure 2.1 and the presented protocol was adapted from previous literature (Jaeger et al., 2009).

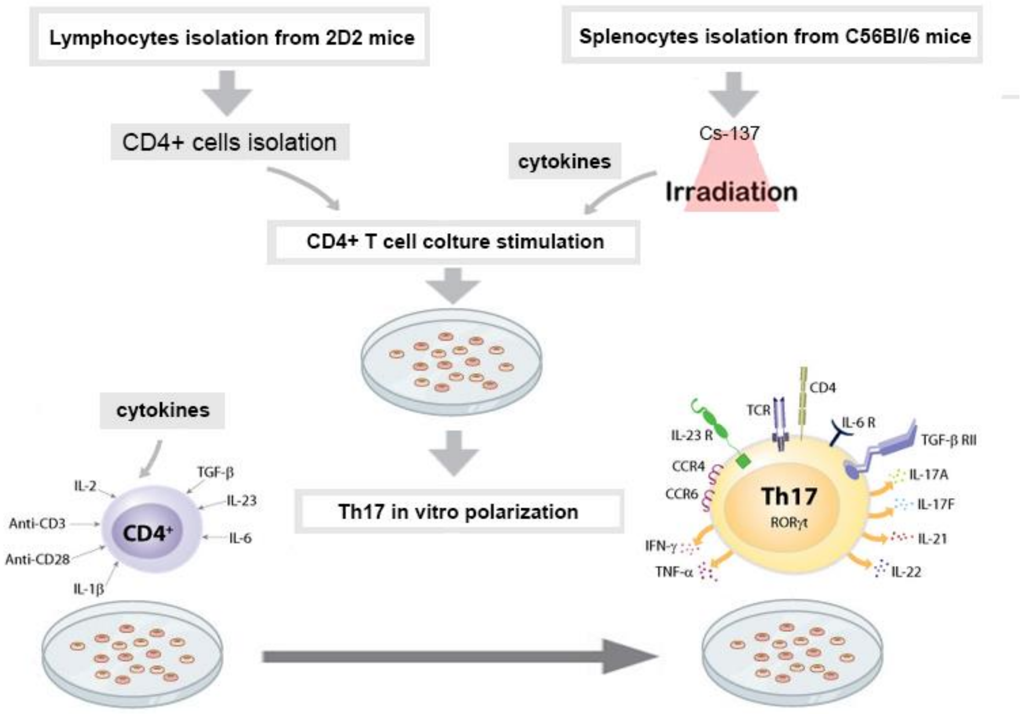

Figure 2.1. B cell differentiation and T-cell polarization method used driven by different molecules. Th17 exibit receptors and express different specific factors. Adapted from R&D Biosystems, 2012.

2D2 mice of 10-12 weeks were deeply anesthetized in order to reach the surgical protocol for sacrifice, with a mixture of barbituric in saline solution (pentobarbital 100 mg/gr in NaCl physiological solution per mice). After cervical dislocation, spleen, axillary and inguinal lymphnodes were collected to achieve the maximum harvesting of B-cells. At the same time, the 2D2 negative mice spleen and lymph nodes were collected in order to obtain the correct factors for T-cells culture stimulation.

2D2 positive and negative mice organs were subjected to mechanical extraction via cell strainer with a 70uM filter (FALCON). Once organ tissues and fat were separated by thawing, the cell strainer was washed with clone media. The enriched washing in cells was collected in falcon tubes of 50mL volume. The obtained cells suspension for the pooled mice were incubated on ice with 5mL of RBC Lysis buffer for 5 minutes, and the lysis immediately stopped by adding a volume of PBS twice the lysis solution. Cell enriched media falcon tubes were spinned at 150G for 10 minutes and re-suspended. Cellular concentration was counted with Burker camera to calculate the exact amount of reagents for magnetic separation needed.

The 2D2 negative mice pool was used to destroy B-cells master regulators and break the membrane to obtain MHC molecules with stimulating cytokines.

CD4 population of B-cells was extracted from the 2D2 positive mice cell suspension. Magnetic columns with nano-sized beads were used (MACS™, Myltenyi biotec, DE), because column-free methods require high concentrations of labelling reagents with the risking of non-specific labelling of the target cell fraction. CD4 population is not stimulated by the nano-sized microbeads and they do not overload with the desired cells in the solution.

The following scheme was adapted from CD4+ T cell isolation kit and the quantities were meant for 10^8 cells (Table 2.1). Upscale was done accordingly with the number of cells in the cell suspension. To avoid column clogging, volumes containing more than 10^8 cells were split in more than one column or diluted. MACS conjugates antibodies were added to the cell suspension and cells were subjected to positive selection with a first eluition. When the columns were removed from the magnetic support, the second eluition was collected, enriched in CD4+ naïve cells (Fig 2.2., D)

	Volumes for 10^8 cells
1st addition of MACS Buffer	400µL
T cell isolation biotin cocktail	100µL
Incubation on ice for 5’	
2^{nd} addition of MACS Buffer	300µL
Anti biotin microbeads	200µL
Incubation on ice for 10’	

Table 2.1. Volumes of reagents used for CD4+ isolation with MACS columns. Steps are followed for each row in sterility under biological hood.

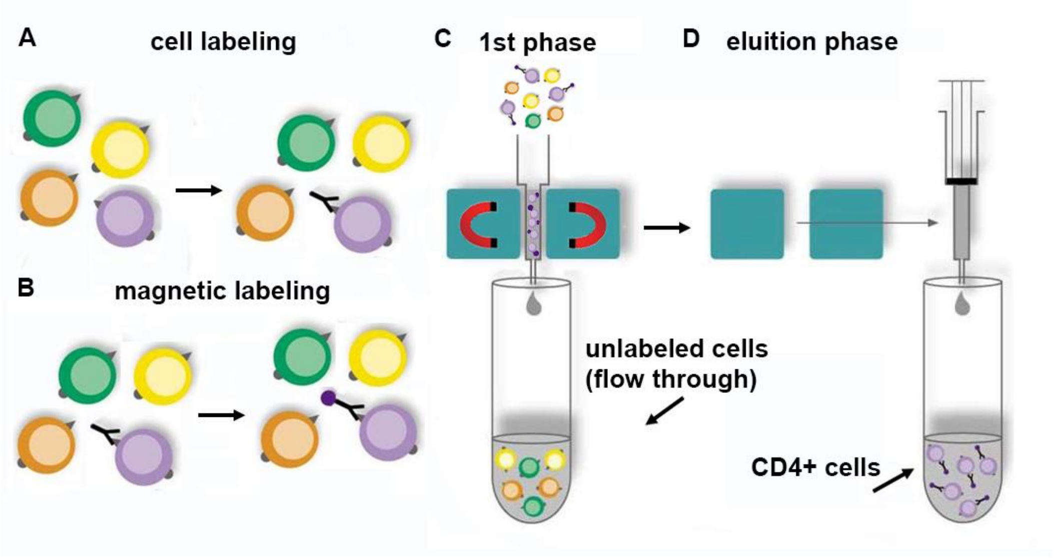

Figure 2.2: CD4+ isolation steps, MACS technology (adapted from Grützkau, Radbruch, 2010); . Magnetically labelled cells in two steps (A and B) are retained in the column (C), while unlabeled cells flow through. After a washing step, the column is removed from the magnetic field of the separator (D), and target cells are eluted from the column.

First, the columns were primed with 3ml of buffer (MACS LS column). As soon as the tank was empty, cell suspension enriched with nanobeads coated with CD4+ antibody was applied. The second flow through is enriched in CD4+ T cells, and to a better collection and concentration of them, the columns were washed again with 3 mL of MACS buffer.

Eluition collected was spinned down at 150G for 10’ and the pellet resuspended in fresh clone media. T-cells were counted in the solution to make a suspension of $4*10^6$ cells/mL. The suspension was cultured at $2*10^6$ cells/mL in coated-6-well plates (NUNCLON Delta, corning Thermo Fisher, DE) and incubated for 48 hrs at 37% with 5% CO_2 concentration.

The single cell suspension from 2D2 negative mice spleens was incubated on ice and irradiate at 30Gy with a Cs-137 source, preheated at 225kV, 13mA, 810 times, for 7 minutes. The splenocytes were coltured at 10^7 mL^{-1} in clone media, to prepare a suspension in concentration $2*10^7$ mL^{-1}. A cytokines mix that consisted in mIL-12 (20ng/mL) anti CD3 (5µg/mL), anti-IL-4 (40µg/mL) was added, in a volume twice the concentration of the harvested cells.

Both CD4T+ and irradiated splenocytes were mixed to obtain an homogeneous suspension, in ratio 2:1 of volume respectively, and distributed to 6-well plates for cell culture. The plates were incubated for 48 hours at 5% CO_2; afterwards the wells were pooled and an interleukine as polarization factor was added to the suspension, hIL-2, at concentration of 4ng/mL.

The differentiation was monitored for 48 hours, and clone media changed with fresh one and/or the colture splitted to avoid clusters. After an initial phase of proliferation and blasting, cells reached a plateau.

At this point, the colture was re-stimulated with anti-CD3 (stock 6.9mg/ml) and anti-CD28 (stock 4.33mg/ml) at 2ug/mL, in order to obtain polarized Th17 cells, at the concentration of $2*10^6$ mL^{-1}. The latter stimulation factors were added as coating on new 6-well plates.

After an other incubation of 48 hours, viability and differentiation were controlled by means of FACS intra and extra-cellular staining. Th17 once polarized express both specific surface receptors unlike non stimulated CD4+ population and cytokines. The antibody-fluorochrome conjugates were set before the staining and the panel with respectives dilution factors is reported in table 2.2 . First step in FACS staining is to prepare cells in order to receive fluorescent conjugates. For one sample, 100 uL of cell suspension was washed in PBS, then resuspended with fix solution. The solution was transfered in a FACS plate and incubated for 30’ at 4°C, protected from light.

Method	**Reagents**				
	Antibody-conjugate	DF	**Extracellular staining**	Antibody-conjugate	DF
Viability Staining	CD45-AmCyan (BV510)	1/100		CD45-AmCyan (BV510)	1/100
	CD3-APC eFluor780	1/100		CD3-APC eFluor780	1/100
	CD4- alexafluor 700	1/160		CD4- alexafluor 700	1/160
	CD44-alexafluor 647	1/200		CD44-alexafluor 647	1/200
	FACS buffer	N/A		FACS buffer	N/A
Intracellular Staining	*Antibody-conjugate*	DF			
	Il-17 PECy7	1/100			
	IFN-g-FITC (AF 488)	1/400			
	RORgT BV421	1/100			
	Perm/Wash buffer	N/A			

Table 2.2. FACS panel for flow cytometry assay of Th17 cell viability and differentiation. FACS buffer is calculated per volume and mixed with diluted antibodies. DF: dilution factor.

For extracellular FACS staining, to avoid interference with other membrane receptors, one step was added before adding the conjugates to the sample. The amount of cell suspension was pre-treated with an antibody that block low chain receptors (FcR) in concentration half the volume of the sample (αFcR-Ab/CD16CD32, 1:100 in FACS buffer (PBS 1X, in bovine serum albumin 1%). The plate was incubated on ice, not exposed to light, for 20’ and it was washed with FACS Buffer twice after two spinning cycle at 500G, for 5’.

For intracellular FACS staining, cells suspension was first permeabilized with a series of reagents (transcription factor staining kit FoxP3, for 20’ at 4°C. The cells were washed after a centrifugation at 500G for 10’. Cell permeabilization was kept with wash buffer PBS + 0.1% NaN_3 + 5% fetal bovine serum at each step. Immediately after, the antibody cocktail from the FACS designed panel was added to the solution. Cells were resuspended in 200uL of fixing reagent after a centrifuge at 500G for 10’.

Results from FACS staining are reported in the next section. Once the reference measures checked the viability and the differentiation of the cell coltured, incubated Th17 plates were pooled and diluted in clone media for intraperitoneal injection. The suspension concentration was calculated to obtain 3-5x10^6 cytokines producing cells, per mouse.

2.1.3 MRI acquisition in EAE induced by Th17 cell transfer in mice: Diffusion, T1 and T2 weighted imaging

To elucidate brain alterations at structural level in the used preclinical model that exhibits neuronal and axonal damage across brain sections, diffusion weighted, 3D T_1 weighted and T_2 weighted sequences were chosen for in-vivo and ex-vivo experiments. This study focused on the investigation of brain lesion driven by immunological inflammation, in which we expected, at the chronic stage myelin damage and tissutal alterations at the boundaries of major plaques.

All the experiments were carried at the CIBM - Centre de Imagerie Biomedicale, a facility of - Ecole Federale Politecnique de Lausanne (EFPL campus, CH). The CIBM hosts a 9.4T system (Varian), supported by adjacent animal preparation suite for physiological monitoring and surgical interventions, and 14.1 T/26 cm system (Magnex Scientific, Oxford, UK) interfaced to a Varian Direct Drive console (Palo Alto, CA, USA) equipped with 12-cm inner-diameter actively-shielded gradient set with a maximum gradient of 400 mT/m in 120 ls. For the ex vivo study, a total of 20 C57BLJ6 mice of 8 weeks were used: 10 mice were injected with 200 uL i.p. of Th17 pre-coltured cells; 10 mice were assigned as controls and not immunized.

First, the pilot in-vivo study was conducted to test the feasibility of methods and adjust parameters, to achieve the higher number of diffusion coefficients and the best resolution in mouse brain. For the in-vivo experiment, five C57BL6J mice were scanned at two time points, after one week of acclimatisation in the animal facility, the latter at the disease onset. Only two images were acquired in-vivo, i.e. T_2 maps and DWI for each mouse. EAE score was assessed as reported in table 2.3.

Because of the severity of the disease, EAE mice were sacrificed and perfused after the second MRI acquisition, then the collected brains were imaged for ex-vivo experiments to achieve MRI protocol optimization.

EAE typical signs	*score*
No disease	0
Decrease tail tone	1
Hind limb weakness, partial paralysis	2
Complete hind limb paralysis	3
Front and hind limb paralysis	4
Moribund state	5

EAE atypical signs	*score*
No disease	0
Mild balance defects	1
Severe balance effects that cause spontaneous falling over	2
Very severe balance defects that prevent walking	3
Inability to move body weight into a different position	4
Moribund state	5

EAE combined signs: sum of atypical and typical scores

Body weight	*score*
Loss of 5-10%	1
Loss of 10-20%	2
Loss of >20%	3

Table 2.3 . EAE disease score reference. Because of heterogeneity of symptomatic signs, the pathology is checked by combined disease score points.

Acquired images showed low SNR in vivo for both scanners at that time. In order to add more b-values in DWI, and T_1/T_2 mapping, final acquisitions were performed only ex-vivo at 9T.

2.1.4 EAE in vivo diffusion weighted imaging acquisition

First steps were related to setup correct experimental parameters to optimize SNR in brain (volume transmitter/head surface helmet receiver coils) in both scanners. Animals were placed inside the scanner under 1.5% isoflurane, maintaining 54 breath rate per minute and 25 °C body temperature, constantly monitored by small animal monitor sensors and a rectal probe.

In vivo multi-slice T_2 weighted imaging was performed using fast spin echo with an effective echo time (TE) of 52 ms, and a repetition time (TR) of 5000 ms, FOV $11.2 \times 11.2\ mm^2$, data matrix 256^2, slice thickness 0.8 mm.

In vivo diffusion-weighted images consisted in a pulse gradient stimulated echo with the following parameters (3DGRE): TR = 4000 ms, TE = 22 ms, FOV $11.2 \times 11.2\ mm^2$, data matrix 256^2, slice thickness 0.8 mm. This pilot study explored several b values, with a gradient duration of 4 ms applied along the readout direction, in the X axis. Eight b-values plus no weighted reference were applied, to avoid more than 30 minutes of total scan time (0, 250, 320, 510, 754, 830, 900, 1000), FOV length in read out direction 1.8 cm, FOV length in phase encoding directions 1.2 and 1.12 cm, slice thickness of 112, matrix (readout number of points) 256 x 86 x 64, 2 averages, number of slices 21.

Representative SNR outcome in T2w images for 14.1 T is reported in Figure 2.3.

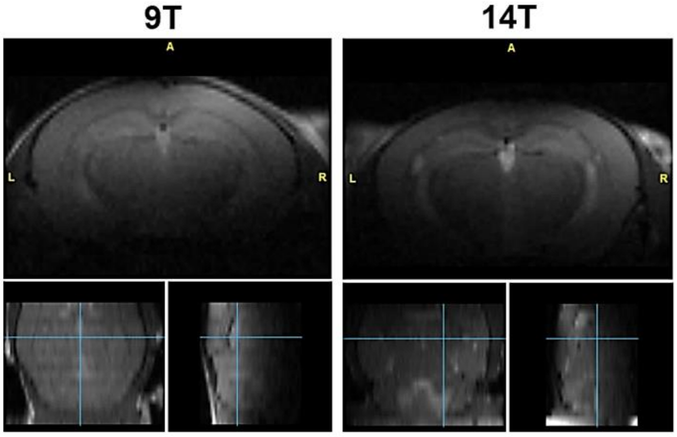

Figure 2.3. Representative T2w weighted images of mouse brain with surface coil helmet in-vivo, at 9 T (first column) and 14.1T (second column), coronal, axial and sagittal section, hippocampus centered. SNR was higher for T1w images, but not suitable for DWI and T2w protocols.

The final experiments were performed using only the 9.4 T scanner, which exhibited better SNR (Signal-to-Noise Ratio) in 3 out of 4 sequences for in-vivo and ex-vivo imaging.

2.1.5 EAE ex-vivo imaging preparation

Animals were pre-anesthetized with a mixture of ketamine/xylazine before reaching the anesthetic depth for surgery. Perfusion consisted in two steps; once thoracotomy was performed to expose the heart, blood was washed out with PBS 1X for a total volume of 15mL, followed immediately by fixation with PFA 4% in normal saline solution. Pressure was maintained constant, using a connected Gilson peristaltic pump, pre-set for small rodents perfusions, with 2mL/min flow.

Mouse heads were dissected in order to remove skull and surrounding structures, spleen and the whole spinal cord collected for further reference. All the organs were immersed in PFA 4% in phosphate buffer for at least 4 hours, then they were left in PBS 1X, pH 7.2.

After remaining in fixative solution, brains were transferred for a week in sterile PBS 1X with 2% sodium azide, to preserve tissue integrity from mould contaminations. Immediately before time scan sessions, the specimens were transferred to Fomblin Y LVAC 06/6 (perfluoropolyether, Solvay, US), to avoid any spurious signals from the solution, and further they were degassed for air bubbles removal, to reduce magnetic susceptibility artifacts. The overall MRI pipeline is depicted in Fig. 2.4.

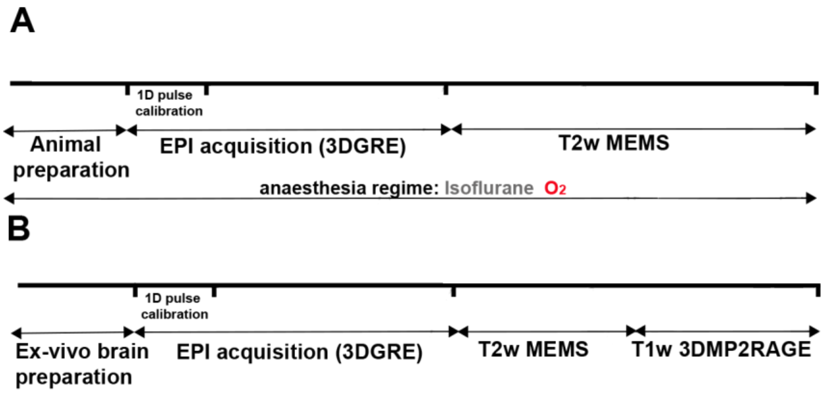

Figure2.4. MRI pipeline applied in the experimental model of EAE induced by Th17 adoptive transfer (A) preliminar in –vivo experiments. B) ex-vivo high resolution experiments.

2.1.6 DWI and T1/T2 weighted ex-vivo image acquisition

First, one-dimension pulse sequence was acquired for system calibration. Frequency lock and signal were checked before local shimming. After a scout image to position the brain correctly, the final protocol was set with the following parameters:

T1w images were acquired by means of 3D MP2RAGE sequence with the following setup: TE delay 4 seconds, TR 4 seconds, spoil time 4 sec; matrix size (readout number of points) 256 x 64 x 28; slice thickness: 112 um, contiguous; TE 0.005 sec, TR 4.8 sec, FOV length in phase encode direction 1.2 cm; FOV length in read out direction 1.8 cm.

T2w images were acquired by means of MEMS sequence, at 24 different Echo Times (ms) : 8.8, 17.6, 24, 26.4, 35.2, 44, 52.8, 61.6, 70.4, 79.2, 88, 96.8, 105.6, 114.4, 123.2, 132, 140.8, 149.6, 158.4, 167.2, 176, 184.8, 193.6, 202.4, 211.2; TR 5.5 ms; Slice thickness 400 um, number of slice 24, matrix size readout number of points 256; FOV length in phase encode direction 1.2 cm, FOV length in read out direction 1.8 cm.

Diffusion weighted images consisted in 3DGRE sequence setup: TE 0.04 sec, TR 0.025, 28 GE cycles, linear encoding, 16 b-values plus no weighted reference (0, 10, 60, 130, 200, 250, 320, 390, 440, 510, 580, 630, 700, 770, 830, 900, 1000 s/mm^2), 2 averages, number of slices 21, FOV length in read out direction 1.8 cm, FOV length in phase encoding directions 1.2 and 1.12 cm, slice thickness of 112, matrix (readout number of points) 256 x 86 x 64.

2.1.7 DWI and T_1/T_2 ex-vivo weighted image processing

All acquired in-vivo and ex-vivo images were analysed by means of custom scripts in matlab software environment. Metrics extracted were related to mean, parallel and perpendicular (i.e. axial and radial diffusivity, respectively) diffusivity. T_1 and T_2 weighted images were processed to obtain corresponding maps. In-vivo maps were reported previously as representative images and no further discussed in this work. Moreover, noise was corrected for DWI scans by means of B0 map for each scanned mouse. For further information, a little overview is reported in the appendix, section A.

DTI matrix was obtained from diffusion weighted images from the three gradient directions using custom matlab scripts. Diffusivity parameters, λ_1, λ_2 and λ_3 were considered as scalar indices associated to white matter fiber tracts geometry (Basser, Pierpaoli, 1998). Calculations were made using the equations reported below.

$$\lambda_1 = longitudinal\ (axial)\ diffusivity$$

$$(\lambda_2 + \lambda_3)/2 = radial\ diffusivity$$

$$(\lambda_1 + \lambda_2 + \lambda_3)/3 = mean\ diffusivity$$

$$\sqrt{\frac{1}{2}}\frac{\sqrt{(\lambda_1 - \lambda_2)^2 + (\lambda_1 - \lambda_3)^2 + (\lambda_2 - \lambda_3)^2}}{\sqrt{(\lambda_1^2 + \lambda_2^2 + \lambda_3^2)^2}} = fractional\ anisotropy$$

2.1.8 Histology in the EAE induced by Th17 cell transfer

Before ex-vivo imaging, organs were fixed for successive histology. Brain were scanned at 9.4 T, at the peak of the inflammatory stage, then processed for histological staining.

After the MRI sessions, brains and other organs were subjected to de-hydration process, that consisted in increasing alcohol concentration (EtOH, 50%, 70%, 90%, 95%) and a latter step in xylene solution twice for a total time of 1 hour. Samples were embedded in paraffin by means of a warmed paraffin bead tray, with a cooling pad module (Leica tissue embedder, DE). Spinal cord, brain sections, as well as liver and spleen for control were placed in the same tray for each mouse, following a previously described method (Steinbach and Merkler, 2009). Hardened paraffin blocks were cut in coronal sections 5µm thick, using a rotative microtome (Leica Biosystem). Serial slides were re-hydrated by means of decreasing EtOH concentrations until their immersion in distilled water. Number of lesions was detected using hematoxylin, counterstained with eosin (HE). Myelin distribution and distruption was assessed with Luxol Fast Blue (LFB), dissolved in EtOH, counterstained with periodic acid Schiff. Cell nuclei were visualized with hematoxylin; axons and nervous fibers by means of silver nitrate impregnation, (Bieschlowski, 1903). After dehydration, all the slides were mounted in Entellan (Merck Millipore, Germany).

Antibody	*Primary antibody*	*Antigen retrieval*	*Secondary antibody*
T-cells	CD3	Citrate (pH = 6)	Biotin anti-rat
T-cells	CD4	Citrate	Biotin anti-rat
Oligodendroglia	Oligo2	Citrate	
Activated macrophages	Mac3	Citrate	Biotin anti-rat

Table 2.6. antibodies used for Immunohistochemistry (IHC) and inflammatory evaluation

The severity of the disease in EAE may vary during the disease course. Inflammation at onset stage is more pronounced. In the model used, the peak of

CNS damage is dependent of Th17 viability and occurs between the 13th and 15th day post i.p. injection.

Quantitative assessments of the observed lesions were made with different immunohistochemistry staining, with a protocol adapted for mouse tissues, using the primary antibodies panel showed in table 2.6.

Nerve fibers were observed by means of Bielschowsky's silver staining.

Inflammatory foci (IF) in n spinal cord section and n brain slices were counted in HE slides. The inflammatory index was calculated as follows:

$$IF\ index = \frac{\sum_{i}^{n} IF}{n}$$

Measure of demyelinated areas was performed on LFB/PAS slides; white matter (WM) area was also measured. The degree of de-myelinization was expressed according to the following formula, where n is the number of portions analyzed (spinal cord or medulla sections mostly):

$$demyelination\ degree = \frac{\sum_{i}^{n} \frac{Demyelinated\ area}{WM\ area}}{n}$$

T-cells, macrophages and Oligodendroglia were manually counted over the whole brain area in each slide; the infiltration density was calculated using the equation reported below:

$$\frac{T\ cells}{mm^2} = \frac{\sum_{i}^{n} \frac{Number\ of\ T\ cells\ (macrophages)}{WM\ area}}{n}$$

Axonal density was also calculated for the spinal cords of EAE versus healthy controls:

$$axonal\ density = \frac{number\ of\ axons}{analyzed\ area}$$

$$axonal/fiber\ density = \frac{optical\ density}{analyzed\ area}$$

Axons can be easily counted in spinal cord cross-sections, but in the medullar/cerebellar region they are packed in nerve fibers. In this case, the cerebellar-medullar portions of the brain were evaluated by optical density obtained from blackish silver impregnation, using ImageJ software.

2.2 EAE induction by MOG injection and Ptx sensitization

After local animal care committee reviews about the protocols aforementioned, all research involving animals were carried out following the directive 86/609/EEC and dl 116/01/92 Italian legislative decree. All animals involved in these studies were stored in animal facility with food and water ad libitum, conventional animal facility.

Immunization was induced in 10 C57Bl/6 mice of 6–8 weeks old, by means of subcutaneous injection of $MOG_{33–35}$ peptide in complete Freund's adjuvant with *Mycobacterium Tuberculosis*, 300 μg and 0.8 mg/ml, respectively. Mice were also injected intravenously (i.v.) with pertussis toxin (40 ng) at the day of immunization and after 48 hours, following a previously reported method (Costantin, 1999). Score was assessed with the criteria reported in table 2.3, while mice that exhibited atypical signs (paraesthesia, lack of coordination) were excluded from the study.

EAE disease signs	*score*
No disease	0
No tail tone	1
Mild hind limb weakness	1.5
Hind limb weakness, partial paralysis	2
Complete hind limb paralysis	2.5
Front and hind limb paralysis	3
Moribund state	4

Table 2.3 EAE induced by active MOG score on C57BLJ6 mice.

2.3 SOD development and score assessment

Wild type (WT) B6SJL strain (Jackson Laboratories, ME, USA) were crossed with mouse line carrying the mutant SOD1 human gene, B6SJL-Tg(SOD1*G93A)1Gur/J GH1. The gene is driven by human promoter sequence of superoxide dismutase 1 and the mouse was designed as hemizygous B6SJL.SOD1-G93A.

Transgenic progeny was identified by polymerase chain reaction targeting the SOD1(93A) gene, as defined from jax allele datasheet. Disease development was longer than high copy number SOD1 mice and similar to previously published data (Henriques, Pitzer et al, 2010).

All mice were trained weekly to motor test, after the 50th day from birth. Motor coordination assessment included scoring signs of muscular deficit, paw grip, and rotarod task execution. Also body weight was measured to determine the correct timing of disease stages to be considered for rsfMRI acquisitions.

Motor deficit signs were evaluated following the score scale in tab. 2.4. Measures were reported by Bonafede R. and Scambi I, from Mariotti research group at Department of Neurological Sciences and Movement, University of Verona.

Onset symptoms were assessed in presence of combined body tremor, lack of hind limb extension reflex as well as three consecutive failures in motor tests. End stage symptoms included exacerbated signs of motor weakness and severe body paralysis.

At the end stage, after MRI acquisitions mice were sacrificed as they reached the humane endpoint. Objective measurements were performed twice weekly by means of paw grip extension test (PGE) and rotarod test. Previously reported protocols were used to assess clinical score and conduct PGE and rotarod test correctly (Gurney et al., 2004; Miana-Mena et al, 2005; Weydt et al, 2003). PGE test consisted by placing each mouse onto a metal grid. The grid was quickly turned up and down and the latency until the mouse let go with both hindlimbs was timed. Two attempts per mouse, with a cut-off time of 120s, were given to hold onto the inverted grid. Time spent in the rotating rod was measured also, with a cut-off of 180s. Test consisted in placing the mouse in the rotarod, increasing the rotation speed until 16 rpm. The time spent in the rod until fall was recorded, two trials per mouse.

Clinical signs	*Score*
Normal	4
Hindlimb tremors when mice is suspended by the tail	3
Normal gait disturbances and abnormalities	2
Hindlimb dragging	1
Inability to right after 30 seconds	0

Table 2.4 Disease score scale for SOD1 mice

2.4 RsfMRI acquisition in the MOG-induced EAE and in the SOD93A experimental models.

Preliminary experiments were performed in a group of n=10 C57Bl/6 female mice, never immunized, to validate the rsfMRI protocol and the processing pipeline.

Second pool of rsfMRI experiments involved two different neuropathological disease models:

i) EAE MOG/Ptx mice (n=10) and not immunized mice age-matched as controls (n=10). All mice were acquired at two time points: first was at 1st day post immunization, while the second was at 20 days. EAE were followed until the 26th day to assess the disease progression.

ii) SOD-1 (G93A) transgenic mice (n= 11) and n = 10 age-matched wild type (WT) (B6SJL) mice were used as controls (WT). All mice were scanned twice. Two acquisitions were performed, first at the disease onset and second at the end stage of the disease, in SOD and WT respectively. For SOD(G93A) mice, rsfMRI experiments were performed at first rotarod test failure, as reported in literature (Luh, Das and Bertolotti, 2018), and at severe paralysis (about 90 and 120 days from birth, respectively). All experiment were carried at University of Verona.

RsfMRI scanner setup and in-vivo pipeline consisted in a scout image, a single shot EPI sequence for motion correction, the EPI functional image and a T_{2w} high-resolution image (fig.2.5). A total number of 41 mice were used for this method.

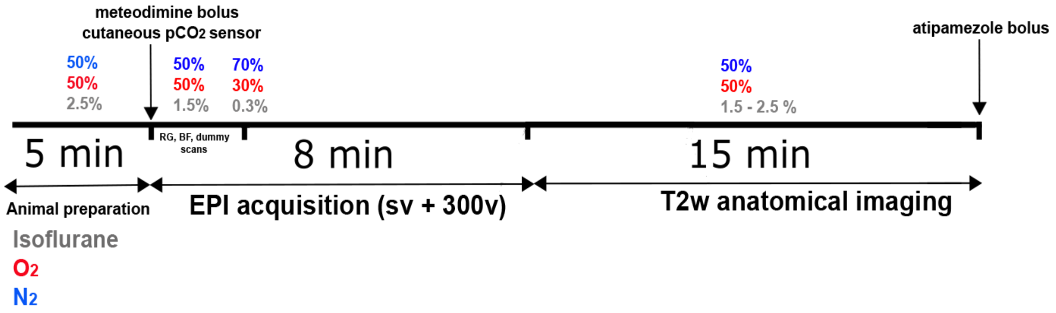

Figure 2.5 Timeline of rsfMRI experiment at 4.7T. Anaesthesia regime was modulated to create less interference with cerebral blood volume. EPI sv: single shot, tilted orientation, one single volume; EPI 300v: 300 volumes.

In vivo acquisitions were performed on a Biospec Tomograph operating at 4.7T, equipped with AVANCE II electronics (Bruker, Germany), available at Centro Piattaforme Tecnologiche (University of Verona, Italy). The capability of the self-shielded gradient was 40G/cm in intensity (BGA9, Bruker, Germany). A double coil configuration with a 7.2 cm i.d. bird cage volume coil and a helmet-shaped surface coil used as RF transmitter and receiver respectively.

The anaesthesia regimen was adjusted accordingly to previously reported studies (Shah, 2016). Mice were anaesthetized with 2 - 2.5% Isoflurane (in a mixture of O_2/N_2 50/50%) in a plexiglas induction chamber. Once the mice were positioned into the scanner, transcutaneous pCO_2 sensor and breath pads were added to monitor the physiological parameters during the experiments. Body temperature was maintained at 37–38°C through a warm water circuit embedded in the animal holder (Bruker Biospin GmbH, Ettlingen, Germany).

Instrument preparation and connected devices are depicted in Fig 2.6. Gas anesthesia was maintained inside the scanner at 2%, with a maximum of 2.5 %, accordingly to mice weight, and administered via a facemask (Fluovac, Harvard Apparatus) connected to a coaxial circuit. To avoid motions artifacts, the head was immobilized by means of ear bars, and the mouth fixed with a dedicated bite bar. Before acquisition of rsfMRI images, mice received an i.p. bolus injection of 0.3 mg/kg of medetomidine. Immediately after, gaseous anesthesia was reduced to 0.3%, with vehicles gases O_2/N_2 at 30/70%, to increase oxygen inhalation and avoid low cardiac rate due to isoflurane interference with medetomidine. The pCO_2

remained within the physiological range during the overall imaging timeline (34 – 40 mmHg). Mice that exhibited higher pCO_2 values, during the EPI acquisition, were excluded from the study.

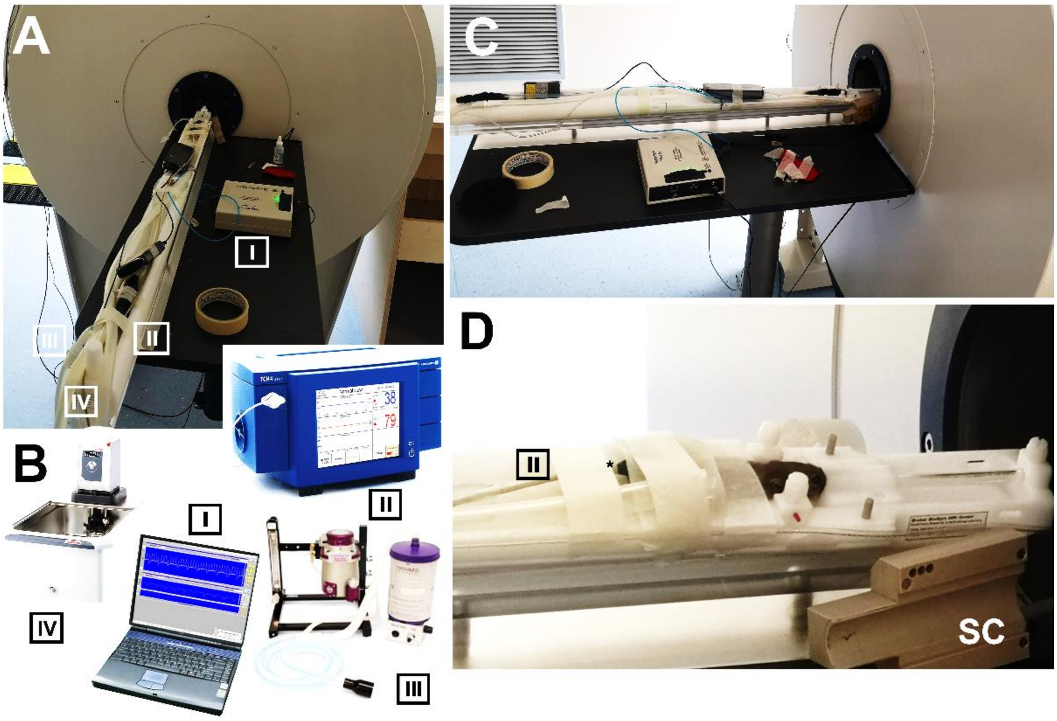

Figure 2.6. Animal preparation for imaging acquisition (A); I) control gating module coupled to laptop monitor of physiological parameters (I), pCO2 sensor (II), thermostatic warm circuit tubes connections (III) and anesthesia tubes (IV). Animal bed is connected to the respective systems (B); after placing the animal with each sensor (C), head helmet coil (SC) is ready to be positioned above the two plastic guides (D).

A scout FLASH image was acquired to ensure correct brain positioning. Magnetic field inhomogeneity was optimized with a modified shimming Bruker protocol to cover selected FOV. RsfMRI method was started first, and it consisted in two EPI sequences: one for FSL topup tool correction and one with the same parameters (except for readout direction) for BOLD imaging. Under medetomidine bolus effect, images were acquired by means of EPI sequence set as follows, TR=1200ms, TE=7.6ms, 0.313x0.313 mm in-plane resolution, 20 slices 1mm thick, 300 volumes, readout l-r. The last image of the protocol was an anatomical T_2w RARE sequence with the following parameters: TR=5760ms, TE=76ms, 0.156x0.156 mm in-plane resolution, 20 slices of 1mm of thickness. Once the imaging pipeline finished, a s.c. injection of the antidote (atipamezole 0.1 mg/kg) was administered to counteract the previously administered s.c. anaesthesia and to permit faster recovery of the animals. In order to investigate the progression of the pathology and in agreement with previously conducted fMRI experiments on an EAE rat model (Tambalo et al., 2015), and ALS SOD1(G93A) imaging (Bontempi, 2017), functional MRI experiments were conducted at two time points along the time course of the disease.

2.4.1 RsfMRI processing

All echo planar images were collected at the end of both studies in EAE and SOD. To identify functional connectivity networks in mice, FSL suite was used, with adapted mouse brain atlas for 4.7. T resolution. Timecourses were extracted focusing on low frequency signal fluctuations. Movement artifacts were removed from each scan by means of blind and indipendent inspection. Cerebellum and medulla were excluded a priori from the analysis, as well the olfactory tract and ventricles, focusing on functional cortex parcellation. Brains scans were masked, spatially smoothed, temporally filtered and normalized to be further processed for independent component analysis (ICA). Analysis with FSL was only on healthy mice preliminary pool.

For EAE and SOD study, all EPI scans were processed into SPM and AFNI (Penny, Friston et al., 2006). A warped mouse reference brain atlas (Dorr, 2008) was used, re-scaled to the resolution of rsfMRI scans. Areas with higher susceptibility corresponding to vessels and cerebral cavities filled with cerebrospinal fluid (i.e. cerebral acqueduct, ventricular system), as well as the first 4 volumes acquired in the EPI scans were removed from the analysis. Each EPI scan was registered to its anatomical image, and put in the same space. EPI were normalized, masked and smoothed before BOLD values extraction per each mouse. ROI-based timecourses were extracted by means of MarsBAR (Brett, Anton et al., 2002).

Brain mouse atlas was parcellated into sub-regions that are listed in Table 2.7

.

_A)_ Mouse brain regions (_Amg – IP)_		**_A)_ Mouse brain regions (_lo – vgtx)_**	
Abbreviation	**Long nomenclature**	**Abbreviation**	**Long nomenclature**
Amg	Amygdala	*lo*	Lateral olfactory tract
abv	Arbor vitae of cerebellum	*LSC*	Lateral septal complex/nucleus
aca	Anterior part commissure	*MB*	Midbrain
Acb	Nucleus accumbens	*mlf*	Medial longitudinal fasciculus
acp	Posterior part commissure	*MC*$^+$	Motor cortex
Au$^+$	Auditory cortex	*MO*	Medulla oblongata
BF	Basal Forebrain	*MSC*	Medial septum
BNST	Bed nucleus of stria terminalis	*mt*	Mammillothalamic tract
cb	Cerebellum	*OL*	Occipital lobe
Cg	Cingulate anterior	*Olf*	Olfactory bulb
cp	Cerebral peduncle	*opt*	Optical tract
Cpu	Caudate putamen	*PAG*	Periacqueductal grey
Cu	Cuneate nucleus	*Pas*	Parasubiculum
DG	Dentate gyrus	*Pir*	Piriform cortex
Enth	Enthorinal region	*Pn*	Pontine nucleus
fi	fimbria	*Pons*	Pons
Fro	Frontal lobe	*Ptl*	Parieto temporal lobe
Fs	Fundus of striatum	*RC*	Rhinal cortex
fx	fornix	*RS*	Retrosplenial cortex
GP	Globus Pallidus	*SC*	Superior colliculus
GrDG$^+$	Granular layer DG	*sm*	Stria medullaris
hbc	Habenular commissure	*SOIC*	Superior olivary complex
Hi	Hippocampus	*Ss*$^+$	Somatosensory cortex
Hy	Hypotalamus	*st*	Stria terminalis
IC	Inferior colliculus	*Th*	Thalamus
IO	Inferior olivary complex	*Tu*	Olfactory tubercle
IP	Inferior cerebellar peduncle	*vgtx*	ventral tegmental area

Table 2.7 Table of brain regions filled in the FSL toolbox and SPM-GiftICA pipeline. These regions were segmented and used for BOLD signal extraction and they derive from resampled reference Dorr mouse brain atlas, +: regions added from previous functional brain networks, reported in previous described literature.

2.5.2 RsfMRI statistical analysis

FSL's MELODIC tool was used after EPI images preprocessing in the preliminary study on healthy mice. In order to identify ICAs (by means of Independent component analysis) related to brain sub-networks, this was the first approach on preliminary dataset with healthy mice. Within group differences were analyzed by means of within (dual regression) and between (FSLNETS) network comparison. Moreover the pre-processed time series were input into MELODIC and used for a region-by-region analysis. This method was used to determine the feasibility of functional networks discovery at 4.7T. Analysis pipeline is shown below (fig. 2.7).

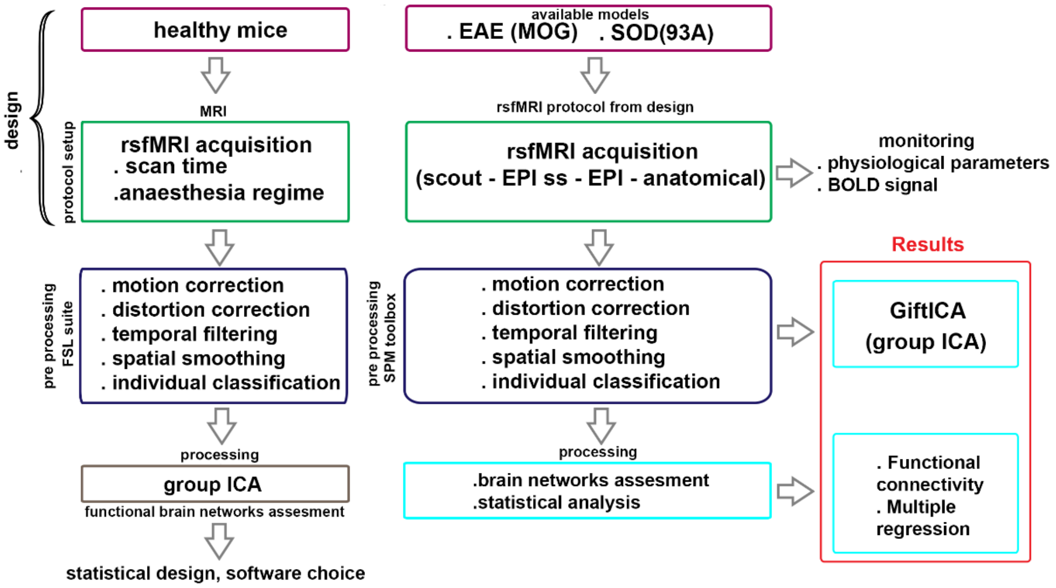

Figure 2.7. Analysis steps in software environment after rsfMRI acquisition. ICA independent component analysis. Red box shows input of statistical analysis.

The second approach, on EAE and SOD datasets, was with SPM/GIFTICA toolboxes, run in Matlab software.

A matrix with size of 54x54 correlation coefficients is therefore obtained for EAE, SOD and their respective control mice. Only positive Pearson correlations values, in selected brain region from 54 segmented areas, were accepted as significant. Statistical analysis focused on different functional/resting state networks as previously described in literature (Gozzi, 2016; Grandjean, 2020).

Once obtained correlation values, to compare which regions in brain differ between groups, multiple comparisons tests was performed, applying false discovery rate correction. Only regions with p values below 0.05 were accepted as significant.

To observe activated functional networks in these experiments, also Independent Component Analysis (ICA) approach was used, similar to the end of FSL pipeline used for the pilot study (Group ICA). Independent component analysis was performed by means of another software, with the same algorithm, named GiftICA (Bajic, 2017), inside matlab environment, after region-wise correlation analysis.

GifICA is based on ICASSO algorithm; all pre processed scans were non-spherical extracted, to proceed with analysis between each group. This choice was more flexible in independent components selection (ICs), in terms of thresholding, number of components and dual regression, as previously stated in rodent brain networks research (Bajic, 2017). Resulted ICs were per each group, that means EAE, SOD at onset, SOD at end stage and their respective controls.

3. Results

3.1. Development of Experimental Autoimmune Encephalomyelitis by adoptive transfer and ex-vivo neuroimaging correlates.

3.1.1 Phenotyping of 2D2 donor mice for Th17 cell culture

Before proceeding to lymphocytes extraction and cell differentiation to obtain Th17 population in vitro, donors were selected by means of FACS phenotyping of CD cells. Mouse colony started from 2D2 transgenic (Tg) mice, as described in the material and methods section 2.1, crossed with C57BJ6 strain. The 2D2 transgenic strain is commercially available and previously reported (Bettelli, 2003). 2D2 Tg mice express, on their T-cells, rearranged Vα3.2 and Vβ11 chains. These chains are on receptor surface (TCR) and specific to myelin oligodendrocyte glycoprotein (MOG). That means that circulating CD cells in 2D2 mice have on their surface these chains that can be detected by flow cytometry assay.

2D2 Tg line was used to to start colture of T naïve cells, following spleen and lymphnodes harvest from mice. First, blood samples were collected from jaw vein and centrifuged to prepare stainings with APC, PE conjugated fluorophores to specific antibodies.

Positive fluorescence for CD4 cells and Vα3.2 in the sample, gated for values above 10^3 arbitrary units (a.u.), indicated hemizygote 2D2 mice that can be used to harvest lymphocytes and splenocytes and start a Th17 colture in vitro (Fig.3.1).

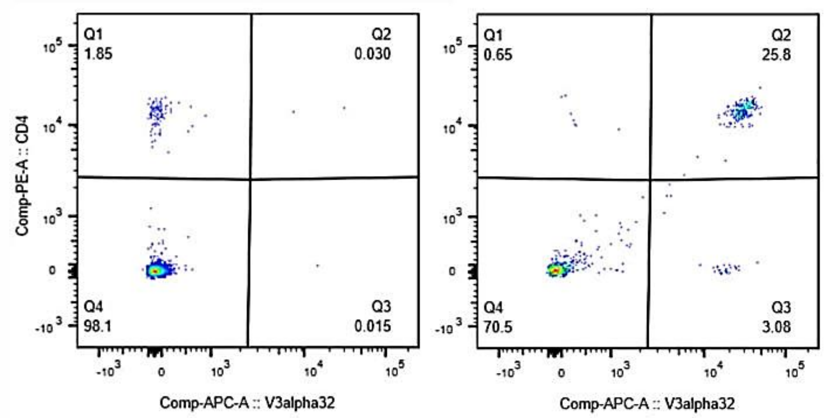

Figure 3.1 SSC/FCS plot. V3α3.2/CD4 plot are shown for two representative mice genotyped. The double positive population for CD4 and V3α.2 staining confirms 2D2 positive Tg mice (right panel). Arbitrary units in logarithmic scale.

Also cell viability and surface markers in 2D2 mice lymphocytes after cell collection, before in-vitro stimulation were assessed. CD4+ cells had higher expression as number of events in TCRb, IL-17 and RORγT. Markers of functional Th17 cells are IL-17, RORγT, that were identified again by FACS, using the reference gating reported in the aforementioned figure.

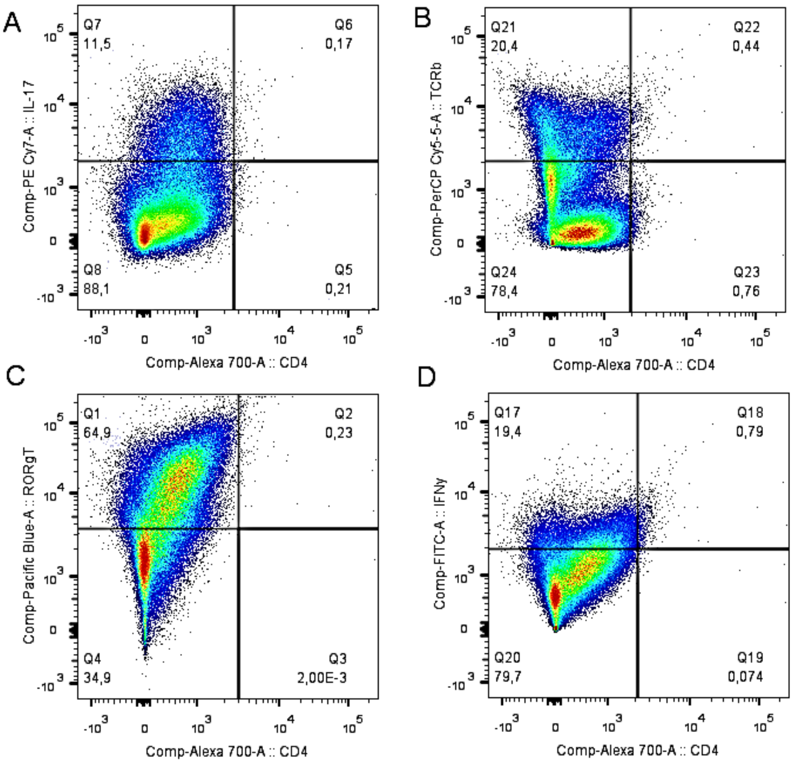

Figure 3.2 Immune cells were isolated and characterized by means of FACS stainings. Populations of CD4 (x axis) in the sample expressed cytokine IL-17 (A), surface receptor tcr (B). Also nuclear receptor RORgT is present in the sample (C) and INFγ (D). antibody conjugates are in y-axis and expressed as number of recorded events. Arbitrary units in logarithmic scale.

The correct in-vitro differentiation of CD4 into subtype Th17 was assessed with intra-cellular and membrane staining at the last step of in vitro culture, before concentration adjustment for cell injection. Th17 expression markers were consistent as previously reported in literature (Jaeger et al, 2009).

3.1.2 EAE development: clinical signs and disease score

Mice were immunized by Th17 cell i.p. injection and observed until the peak of the disease. Immunized mice developed neurological signs of EAE between the 10th and 13th day after Th17 injection. Weight was measured each day at the same hour for all cages, until sacrifice. Score was assessed using as reference an approved panel by veterinary committee, reported previously in Material and Methods, section 2.4.1. EAE mice exihibited typical and atypical clinical scores, as well as weight loss at the peak of the disease (Fig. 3.3). Atypical score included also mouth paralysis, asymmetrical ataxia, loss of spatial coordination. In particular, slight shaking were noticed before the 10th day of observation for some mice; moreover, limp tail and hind limb paralysis was not visible for all of them. EAE induced by Th17 cells injection had a sudden onset with ascend paralysis. Changes in gait balancing and posture, with the impossibility of coordinated motion, i.e walk in a right direction across the space, were classified as atypical signs.

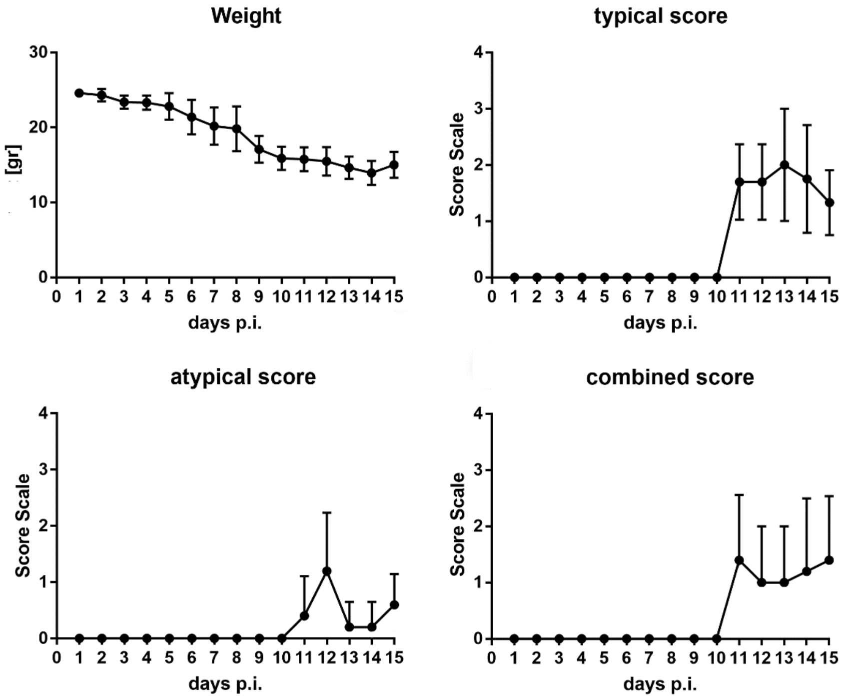

Figure 3.3. EAE mean group weight loss and scores at different time points after induction. All grades were averaged for 10 mice that were followed from the day of Th17 cell injection (d0). SEM is reported. Two mice were sacrificed at the 13th day due to high weight loss (below the 10% of their weight before immunization).

3.1.3 MRI scanner choice for ex-vivo imaging pilot study results.

First pilot study was conducted in vivo with five mice that were immunized as described in section 2. This preliminary step was made in order to choice the best experimental conditions for further studies. Immediately after the disease onset, EAE mice were subjected to optimized protocol for T1w, T2w and DW imaging by using the two available scanners operating at 9 and 14.1 T, respectively.

These acquisitions were performed at different TE, TR and b values for each scanner (14.1 and 9 T) both in-vivo and ex-vivo. Careful comparison between signal to noise ratio (SNR) obtained by the two scanners revealed that T1w images acquired at 14.1 T had better SNR than T1w images acquired at 9.T. However, the SNR in both T2w and DW images was better at 9 T than at 14.1 T (data not included in this work). Ex-vivo imaging maps for both scanner is reported in figure 3.4.

Considering that the aim of the study was to test the specificity of DW metrics in detecting lesions in EAE model, the study switched to ex-vivo imaging. DWI needs high space resolution with a consequent requirement of long acquisition times. Also the availability of scanner-time in the facility was taken in account, thus a good compromise was found in using the 9T scanner instead of the 14.1T one.

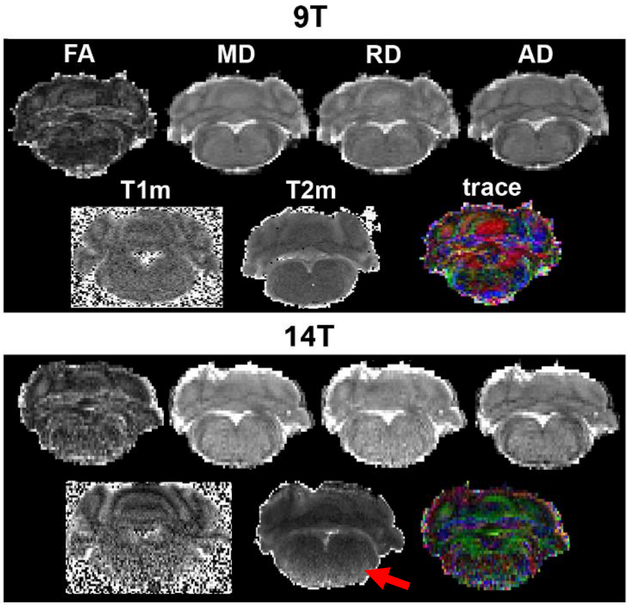

Figure 3.4 Representative maps of DW metrics obtained in ex vivo EAE mice brain, scanned at 9T and 14.1 T, same slice selection. Higher magnetic field showed dishomogeneities visible in the maps obtained (red arrow, lower part of the brain). Also, tensor trace map has poorer resolution in the three space directions.

3.1.4 Ex vivo MRI metrics in the EAE experimental model

A first raw inspection was made after computation of T1 and T2 times, FA, AD, RD and MD values. Huge ROIs were measured by splitting the cerebellar-medullar area from the brainstem-cortex one (Fig. 3.5, 3.6). Mean FA and AD were significantly different in the cerebellar and medullar regions compared to whole brain after unpaired t test.

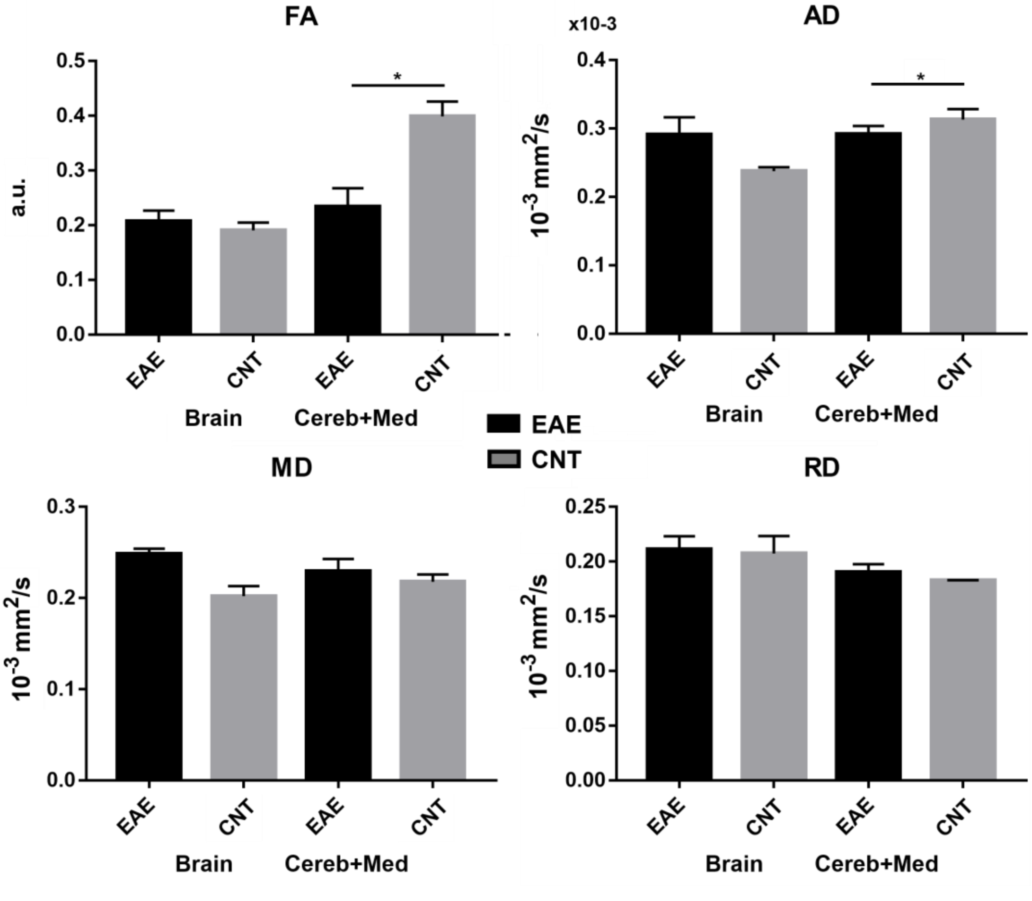

Figure 3.5. Mean Diffusion metrics in the whole brain, whole cerebellum and medullar area MRI slices (Cereb+Med) ± SEM. Values are from averaged mice in the two groups of the study. Significativity is shown in bars (* = p value < 0.05).

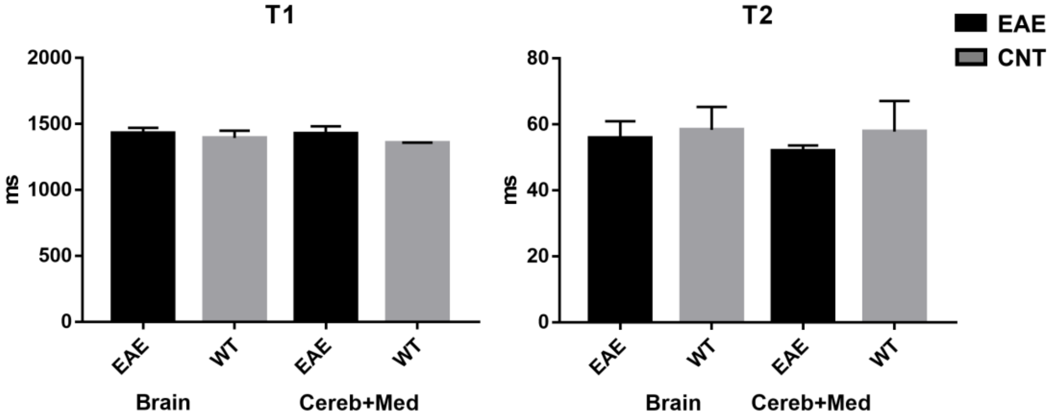

Figure 3.6. T1 and T2 times expressed in ms ± SEM, in the whole brain, whole cerebellum and medullar area MRI slices (Cereb+Med) ± SEM. Values are from averaged mice in the two groups of the study. Significativity is shown in bars, with $p = 0.1$ (p value < 0.05 was accepted as significant

In particular, we addressed the question if ex-vivo gray and white matter, as well as the specific lesion area found in histological microphotographs had changed in the pathology. ROI tracing was carefully done using an high resolution atlas of mouse brain from Allen Brain Institute (Sunkin, 2013; available at https://mouse.brain-map.org). Histological inspection of brain slices showed where the lesions where located, i.e. in the brainstem, medulla and cerebellar regions (fig 3.7). To further investigate how these metrics changed in EAE mouse brain, FA, AD, RD, MD, T_1 and T_2 values were extracted by manually drawn ROIs from ex vivo images in the EAE and CNT groups (Fig.3.8).

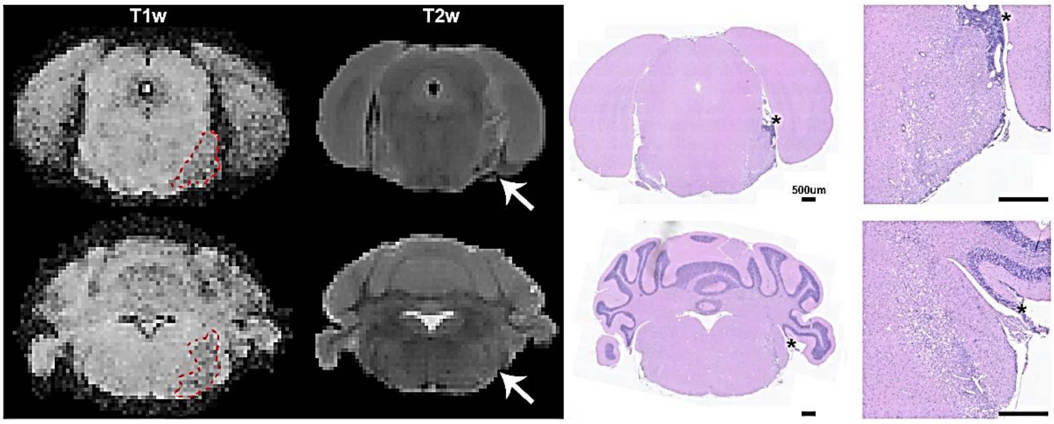

Figure 3.7. T1w and T2w images compared to respective histology, one EAE mouse from the experimental group; bregma -4.20 (1st row),-5.60 (2nd row). HE staining. Lesion likely location is

indicated in MRI images with arrows, while in HE microphotographs asterisk are at the top of the overall area in which lesion is visibile.

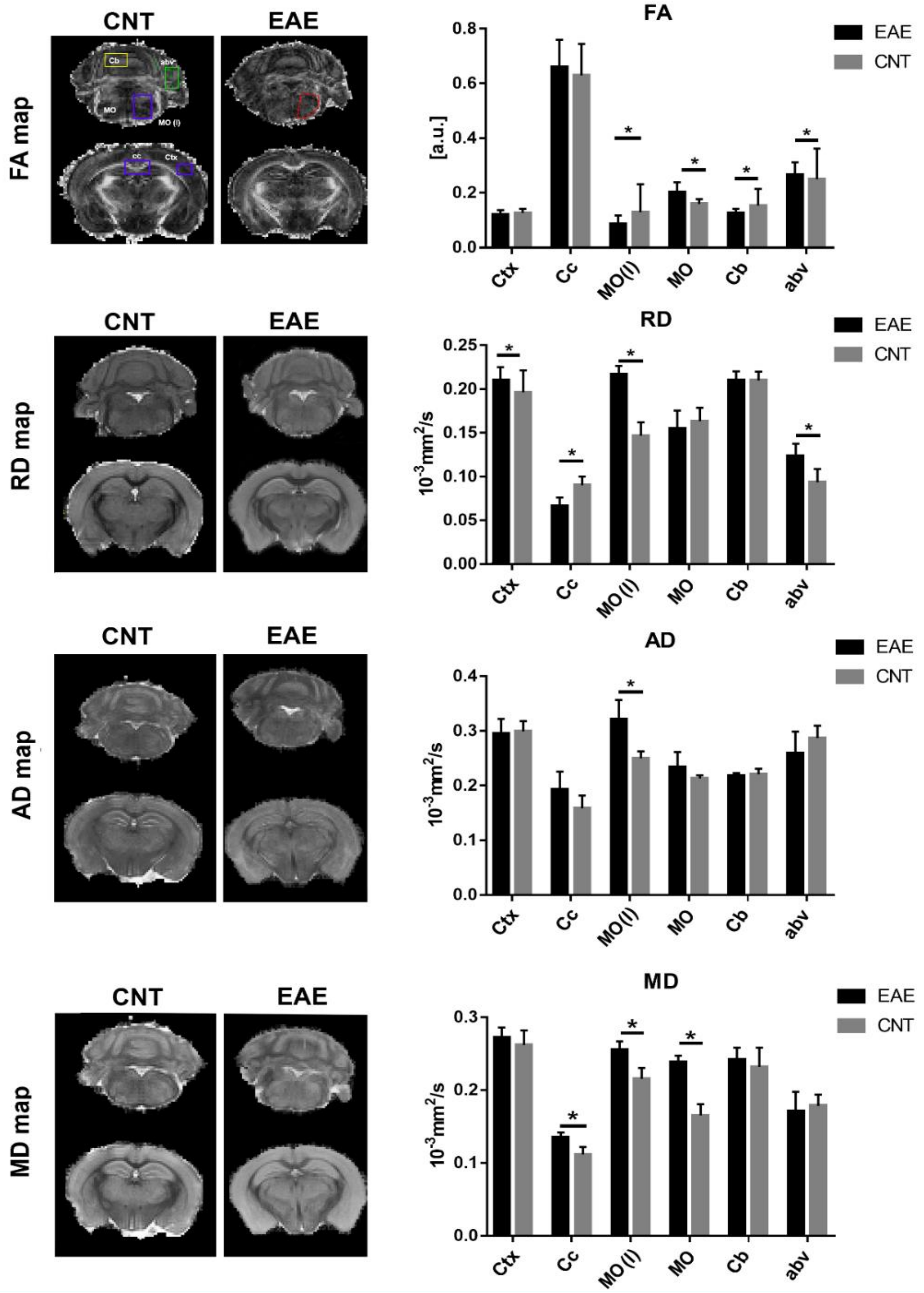

Figure 3.8 Diffusion metrics from ex-vivo acquired images. Fractional anisotropy, FA, Mean Diffusivity, MD, Radial diffusivity RD, Axial diffusivity AD, apparent diffusion coefficient ADC, T1 and T2 values extracted (with SD). Maps of representative mouse, one per per group are flanking the graphs obtained, in two different positions. Measurements are enlightened in the first

panel (left, high) in the FA maps. Ctx=Cortex, Cc= Corpus Callosum, MO= medulla Oblungata , MO(l) = lesion area in the medulla oblongata, abv = arbor vitae of cerebellum, Cb = cerebellum. Significativity is reported as p-value < 0.02 (* and thick horizontal bars).

Statistical significant alterations were detected in T_1 (limited to MO(l)) and in T_2 (in Ctx, CC MO(l) Cb, and abv). As expected a general trend toward an increase in T_2 was observed (Fig. 3.9).

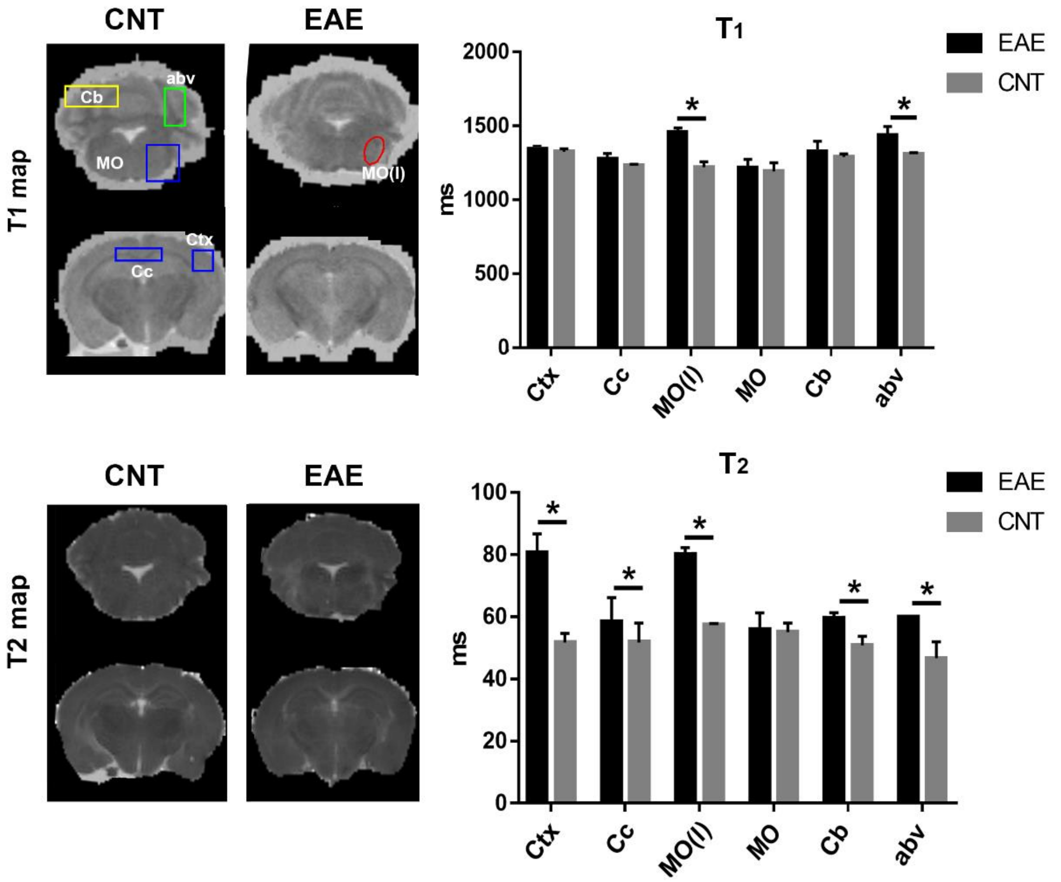

Figure 3.9. T1/T2 metrics from ex-vivo acquired images. T1 and T2 values extracted from T1 and T2 weighted images in ms (with SD). Maps of representative mouse, one per per group, are flanking the graphs obtained (EAE and CTRL idem), in two different positions. Measurements are enlightened in the first panel (left, high) in the T1 maps (coloured boxes). Ctx=Cortex, Cc= Corpus Callosum, MO= medulla Oblungata , MO(l) = lesion area in the medulla oblongata, abv = arbor vitae of cerebellum, Cb = cerebellum. Significativity is reported (*) p-value was accepted below 0.05).

3.1.5 Preliminary DTI results

Representative diffusion fiber direction maps in CNT and EAE ex-vivo mice are reported in Figure 3.15, serial slices from DWI. At qualitative visual inspection, tensor imaging did not show evident visual changes in fiber connectivity for all EAE involved. Anatomical regions where the lesion was observed by histology have different RGB maps, but a tractography approach would highlight possible differences in vivo.

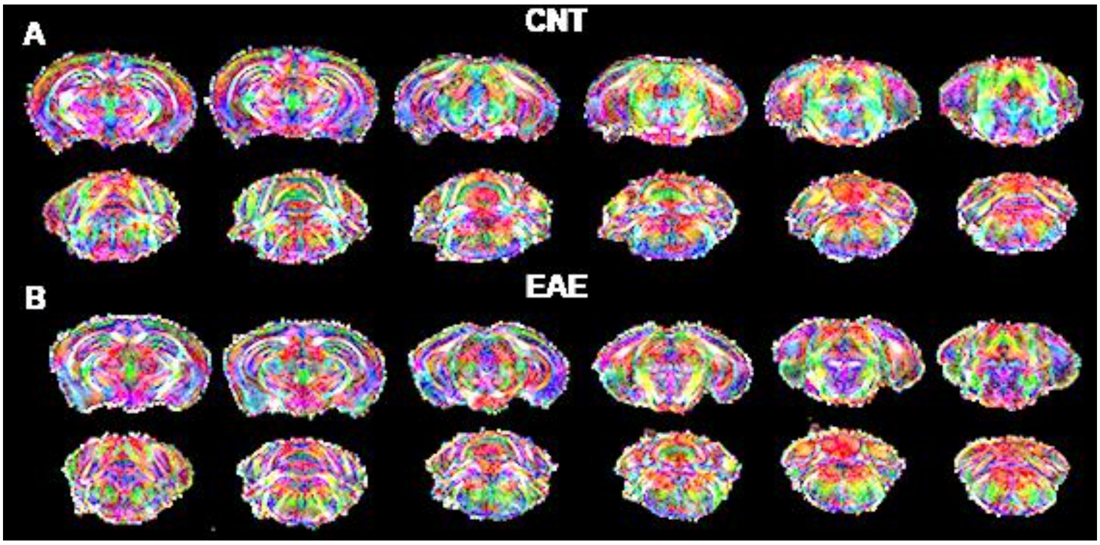

Fig.3.15. Ex-vivo diffusion fiber direction maps of two representative mice, healthy (A) and EAE (B), respectively. Color codes are red = *FA* • cos α; green = *FA* • cos β blue = *FA* • cos γ.

3.1.6 Ex vivo MRI and histological findings in the EAE model by Th17 adoptive transfer

Brain lesions in EAE mice after MRI ex-vivo study were qualitatively evaluated by means of H&E staining and compared with T1w and T2w MRI scans (Tab 3.1, Fig. 3.8). Lesions were clearly detectable in HE slices.

The localization of lesions determined in histology was therefore used to identify alterations in raw MR images. An additional criterion for lesion detection was the non-simmetrical occurrence of inflammatory foci in the brain. Results of visual inspection of H&E histology and T1w/T2w MR images are reported in Table 3.1. Representative T1w and T2w images and their corresponding histological slices are reported in Fig. 3.8 where lesions are outlined by red dotted lines.

# mouse	score	combined	# lesions	Location	T1w	T2w
E4109	1T, 2A	2	5,11,2	Cb, MO, Optic tract	+	-
E4110	2T,3A	3	3,4	MO, Cb	+	+
E4111	1T,3A	3	13,15,2	Midbrain, MO, cb	+	+
E4112	0T,3A	3	2,2,7,2	Optic tract, abv, cb, MO	+	+
E4113	3T,2A	3	2,5	Optic tract, medulla	-	-
E4114	2A,1T	2	2	MO	-	-
E4115	2T,3A	3	2, 3, 4, 2	Cb, MO, cort.spinal tract, abv	+	+
E4116	3T,2A	3	3, 6,4	Cb,MO, cereb peduncle	+	-
E4117	4T,1A	4	1,3,2	MO, cb, optic tract	+	-
E4118	2T, 2A	2	1, 10, 1	3rd V area, MO, abv	-	-

Table 3.1 First inspection of lesions in EAE mice from ex-vivo study in HE stainings. Last assigned score is reported A atypical, T typical, as well as combined per mice, before perfusion procedure. Presence of contrast variation (+) or not (-) was assessed by visual observation at the same position of histological sections. Each mouse in Switzerland has an identification number.

Lesions occurred mostly at the medullar region, as well as cerebellar arbor vitae and tissue, associated with demyelinization and nerve fiber distruption at the same location. Macrophages, CD3 and CD4 cells were present also in the peri-lesion areas (fig 3.11).

Oligo2 stained slides were also visually inspected, but there was no evident change in distribution of the expressed marker related to brain lesions at glance, with lower magnification used (images not reported).

Oligo2 expression decreased in spinal cord, and quantitatively its density changed between groups both in the brain and spinal cord segments. In the spinal cord, axonal loss, swelling and myelin loss was more evident across different sections (see Fig. 3.13).

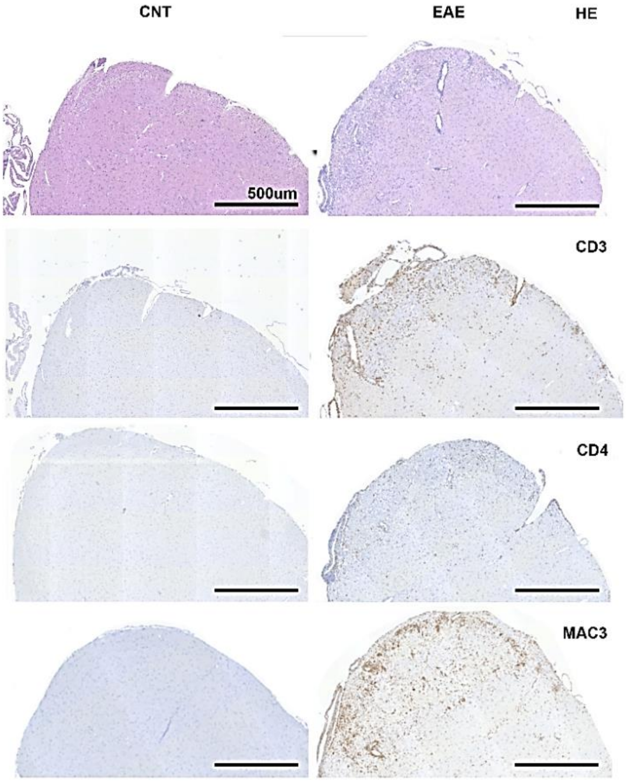

Figure 3.11 IHC of medullar lesion at macroscale, scale bar 500um, bregma -6.56.

Fiber density loss in each position was visible at lowest magnification as reduction of silver impregnation area (Fig. 3.12). At higher magnification, it was possible to detect axonal loss more pronounced in peri-lesion areas (Fig. 3.12).

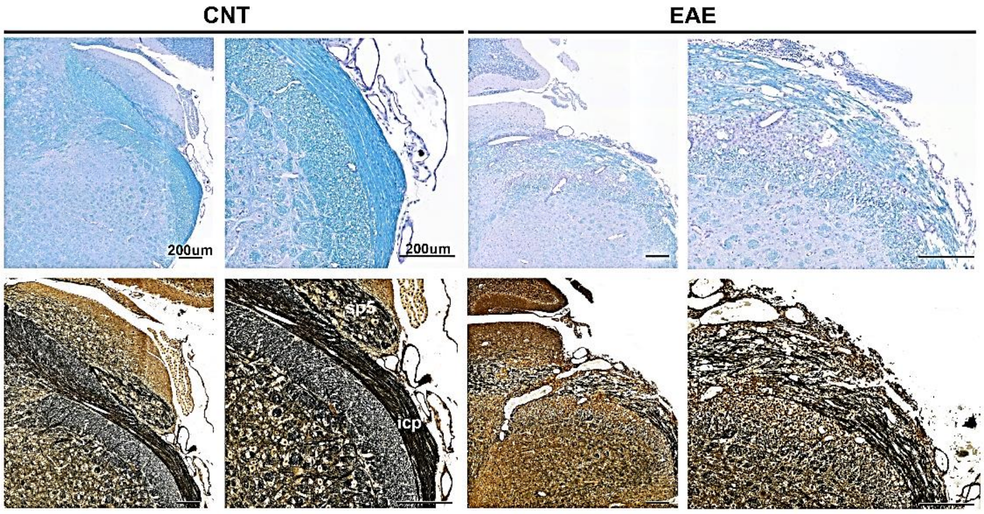

Figure 3.12. Magnified area proximal to lesion, LFB/Bieshlowski stainings bregma -6.24. sp5 = spinal trigeminal tract; icp = inferior cerebellar peduncle (proximity of the rubrospinal tract and the 4th ventricle), scale bar 200um.

Cells were manually counted to assess the degree of inflammation in the brain as inflammation density (Fig. 3.13). Two-tailed Wilcoxon unpaired t test was performed to find differences in collected brain histologies, between EAE and healthy mice.

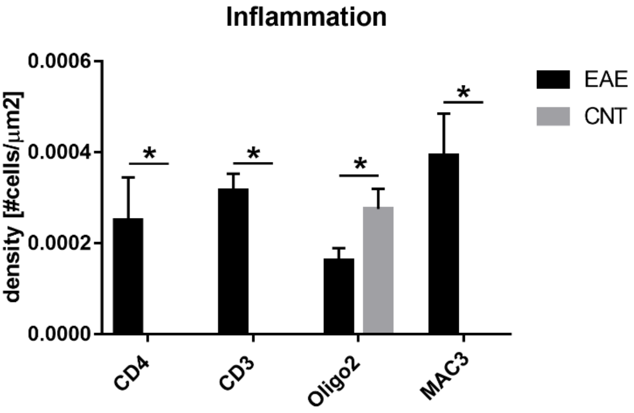

Figure 3.12 Unpaired t-test resulted in significant differences between different inflammatory cells outcomes in the whole brain sections. Infiltrates were found mostly at medullar and cerebellar level. P values under 0.05 were accepted as significant (*)

De-myelinization was more visible at the spinal cord level, enriched in neurons, by means of loss of luxol blue impregnation to lipids (Fig.3.13).

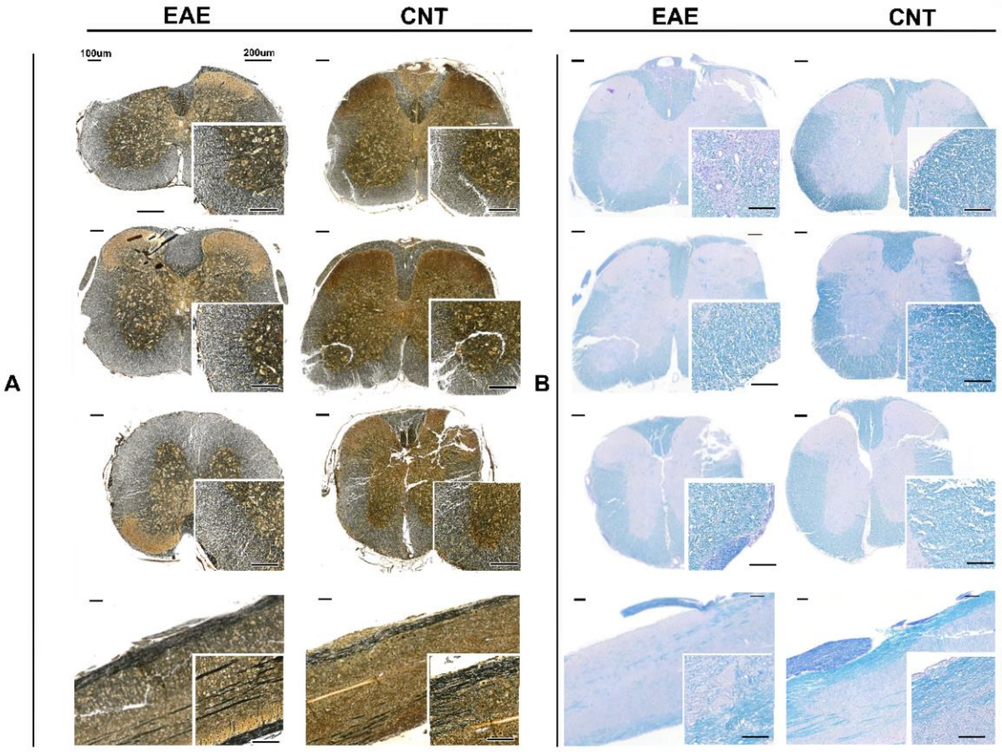

Figure 3.13 spinal cord segments for each position with two different stainings, Bieschlowski (A) and LFB/PAS (B). Scale bar are 100 and 200um, respectively. Section are reported from top to bottom in column, in the following order: cervical – lumbar – thoracic – filum terminale.

Silver staining indicated in brain areas a diminished fiber thickness, suggesting this disruption is consequence of inflammatory processes evoked by macrophages. Cells were manually counted to assess the degree of axonal loss in in the spinal cord also (fig. 3.14).

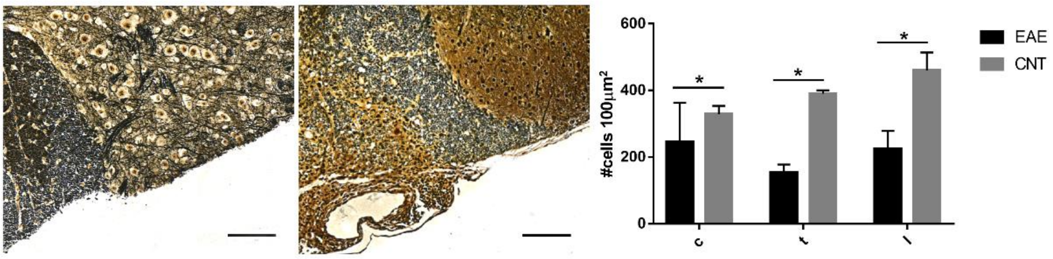

Figure 3.14. Spinal cord portion of an EAE (left) mouse vs CNT (right), Bieschlowski staining. Axonal density was calculated for each collected segment (c = cervical, t = thoracic, l = lumbar). Scale bar 100um.

Optical density (OD) values were obtained by means of color deconvolution. Original image file format from the slide scanner was first converted in RGB color type, then to 8-bit grayscale. Vector values (R,G,B) were set as follows: for Bieschlowski staining: v1 = (0.384,0.558,0.734); v2 = (0.304,0.487,0.818); v3 = (0.551, 0.555, 0.623); for Luxol Fast Blue-Period Acid Shift-Eosin v1= (0.583, 0.553, 0.595) v2=(0.648,0.626,0.431), v3 = (0.851,0.449,0.271). Visual results are reported in Figure 3.14, A, followed by calculated OD (Fig. 3.14.B). Myelin staining had a p-value < 0.05, while fiber staining had a p-value below the significance threshold set, only in the corpus callosum and filum terminale regions.

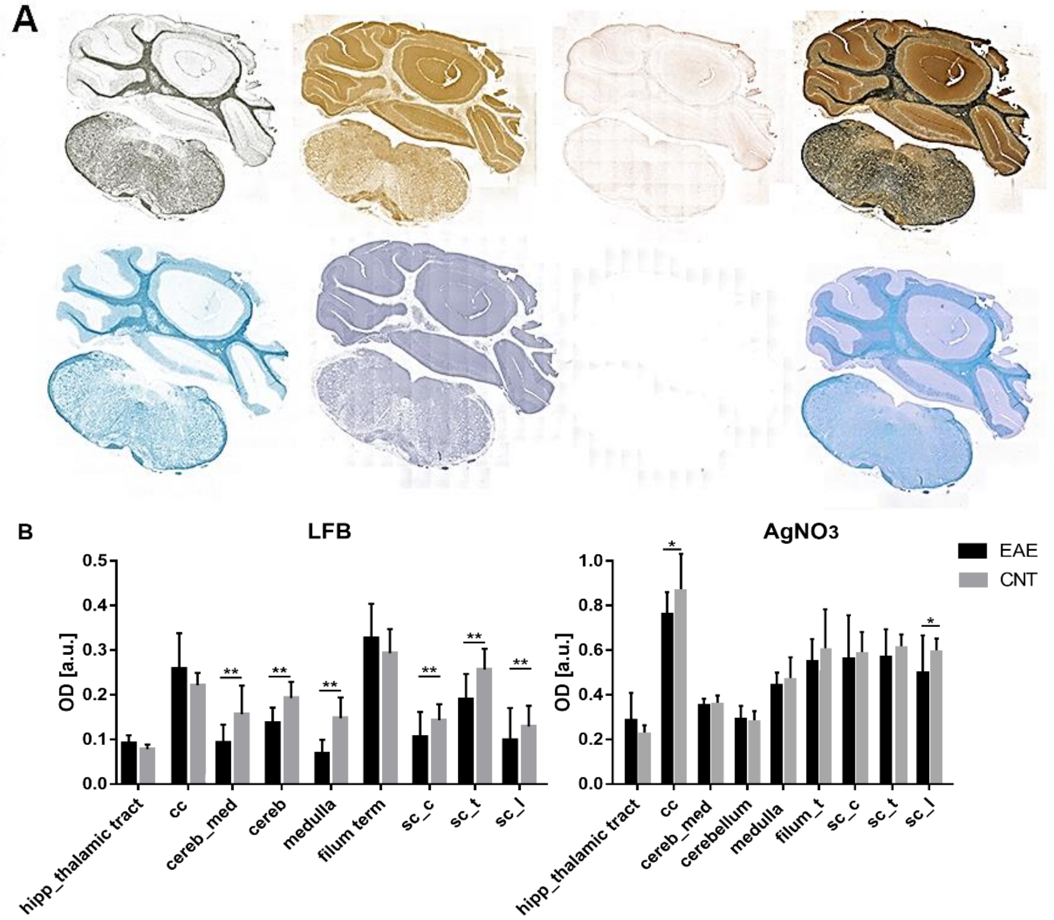

Fig.3.15. A) RGB image conversion and deconvolution for double stainings procedures in three vector components. For a healthy subject, silver staining is shown in the 1st row, while LFB/PAS in the 2nd one, contiguous slices of 5um thickness. B) Mean LFB and $AgNO_3$ optical density (OD) comparison across brain areas. Hipp, thalamic tract: whole myelin OD area at hippocampal level and thalamus. Legend: cereb_medulla is whole OD value for the slice at the posterior part of the brain containing both cerebellar area and medulla; a.u.arbitrary units, suppongo, cerebellum, medulla, sc = spinal cord segments for filum terminale, c = cervical, l = lumbar and t = thoracic. P value significativity is reported (** = 0.02, * = 0.05)

The overall optical density (OD) measured did not show statistically relevant differences, while relative axonal density in the spinal cord segments differed between groups. Macrophages were present in the spinal cord segments, in the lesions, while a decrease in Oligo2 density is spreaded all over each section in EAE mice (Fig. 3.16). Also CD3 and CD4 cells were found in the lesions, but not all the inflammatory cells are simultaneously present in all the lesions inspected by histology. Presence of axonal degeneration is associated to de-myelinization and macrophages infiltrates.

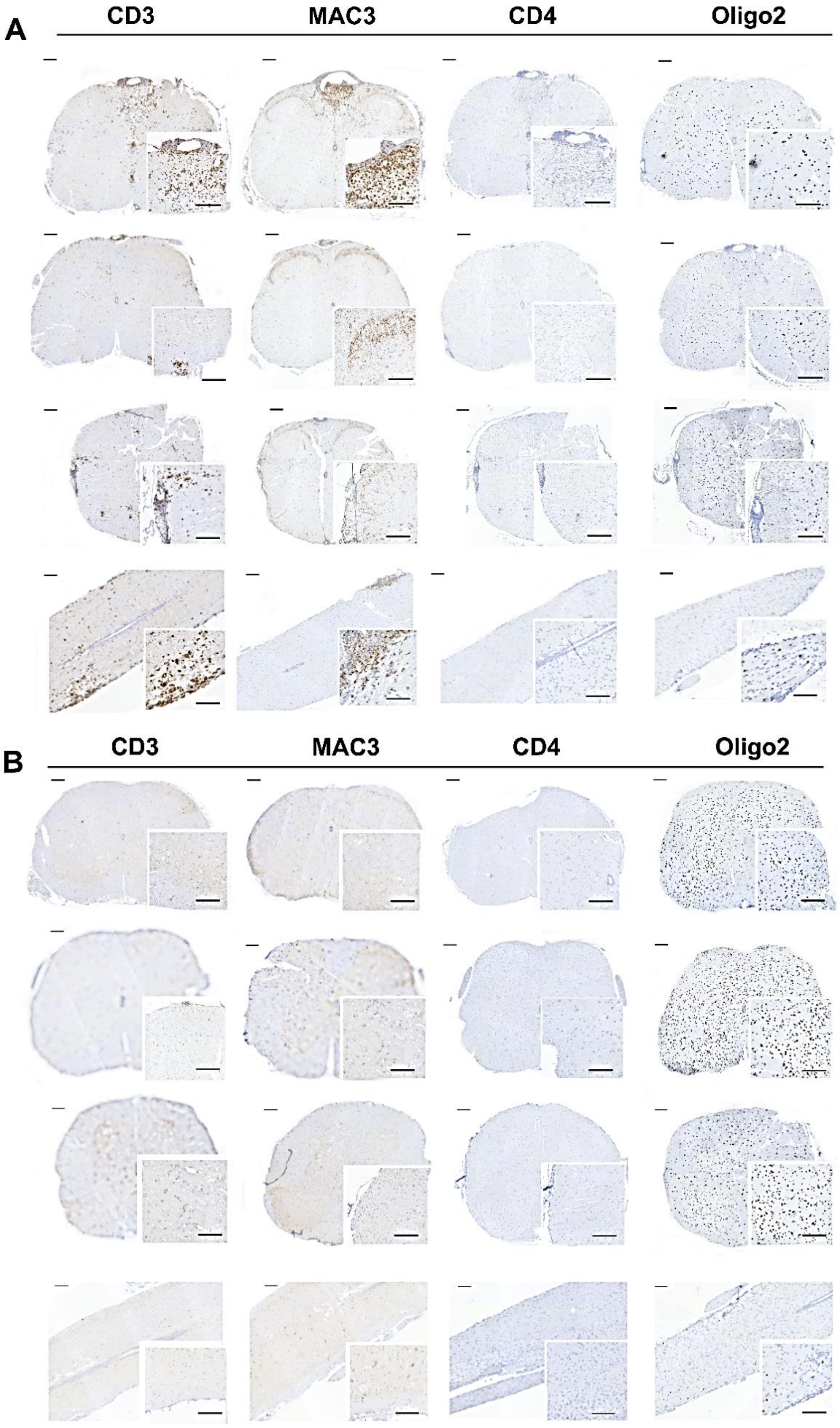

Figure 3.14 Immunohistochemistry of different spinal cord segments in two mice, one EAE (panel A) and one healthy (CNT) (panel B). Section are reported from top to bottom in column, in the following order: cervical – lumbar – thoracic – filum terminale.

3.2 RsfMRI results

3.2.1 Effect of combined anesthesia regimen on the physiological parameters under imaging acquisitions

Some preliminary considerations have to be taken in account, before proceeding to the discussion of results for each study. Because BOLD signal is dependent from cerebral blood volume, physiological parameters on mice were carefully monitored during the acquisition protocol. Different anaesthetics tests in rsfMRI experiment showed different outcomes in acquiring BOLD signal. Concentrations above 2.5% isoflurane decreased BOLD signal detection in rodents, and homotopic functional correlations in mouse brain (Bukhari and Rudin, 2018). Moreover, functional connectivity is compromised with other anaesthetics such urethane and chloral hydrate (Xie, Chung et al., 2019) because of their side effects. Medetomidine combination with low isoflurane concentration resulted more effective to maintain brain connectivity at experimental "rest" condition (Shah et al, 2003). Breath rate per minute was monitored and compared qualitatively across groups. Anaesthesia regime had a double effect: medetomidine lowers the cardiac rate if combined with isoflurane, with consequent decrease of body temperature. The first drop in temperature is caused by isoflurane inhalation, the second one because of the s.c. bolus. A mean measurement with rectal probe is reported in figure Fig. 3.2.1). Thermal water circuit linked to scanner animal bed was set at 50°.

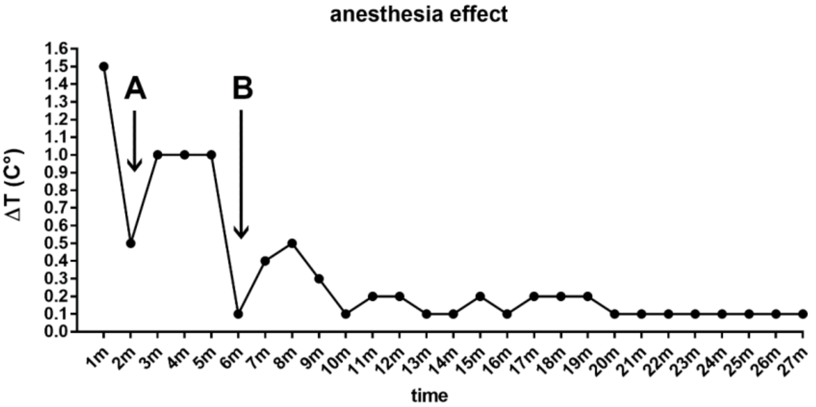

Figure 3.2.1 Temperature drop expressed in difference measured. Data sampling was in minutes (m), from rectal probe continuous monitoring. A) temperature starting drop from animal preparation with s.c. injection of medetomidine at 1.5% isoflurane. B) second temperature drop after scanner placement, effect of medetomidine, at 0.4% isoflurane.

Other relevant physiological parameters, namely the partial pressure of CO_2 in blood, respiratory and cardiac rates were continuously monitored during acquisition. Experiments in which such parameters were outside the physiological value were discarded.

Once imaging protocol was set in order to maximize signal acquisition and resolution, a first evaluation of rsfMRI method at 4.7 T was done in a group of healthy mice (n=15). Image processing was focused first on rodent anatomical atlas and functional atlas, with the same approach on FSL suite (Gozzi and Schwarz, 2016). Brain was segmented in order to extract the whole cortex and brainstem, including the hippocampal area and excluding the cerebellar-ventral medullar regions to define mouse brain networks.

The preliminary choice on the cortex and brainstem was made to compare previously reported studies (Granjean, 2017), in which resting state mouse networks focused in these macroareas. By means of independent component analysis (ICA), Indipendent Components (ICs) were found matching networks from the somatosensory, motor limbic and default mode areas compatible with functional connectivity (FC) values of healthy and EAE mice were detected in a limited number of regions.

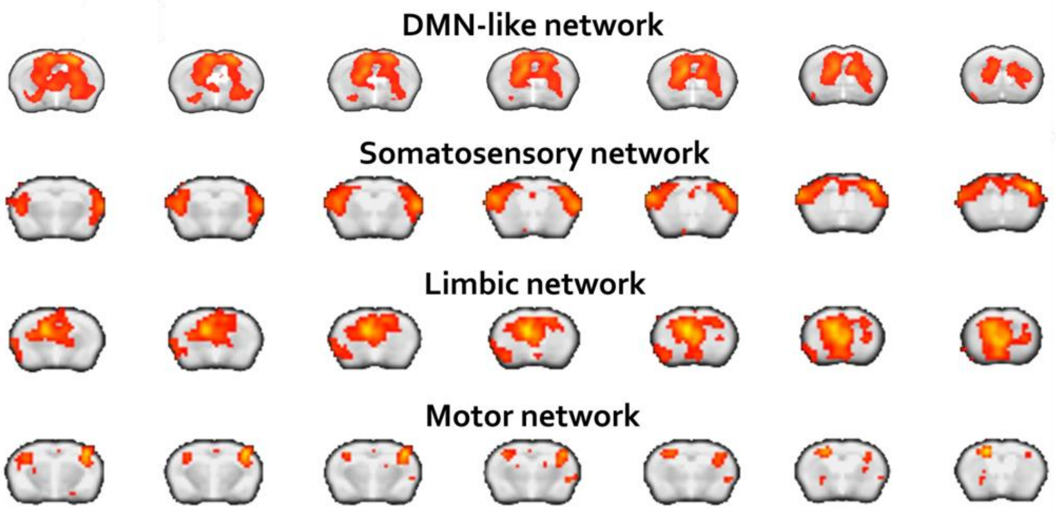

Figure 3.2.2: Functional connectivity networks after FSL analysis, in healthy mice. Bilateral areas are shown in hot color and overlapped to T2w reference brain atlas.

3.2.2 EAE by MOG/Ptx immunization score disease and rsfMRI outcomes

EAE score in mice is reported in Fig. 3.2.3. Disease signs were daily monitored and averaged until the end of the rsfMRI experiment. Major clinical signs in MOG immunized mice were hind limb paralysis and complete tail tone loss from 13 days post immunization (dpi). Partial recover from paralysis was observed at 20 dpi. Coordination along space was preserved and no signs of ataxia were present. Mice with atypical and malfunctional behaviour, such as stereotypies, circling or jumping were excluded from the study.

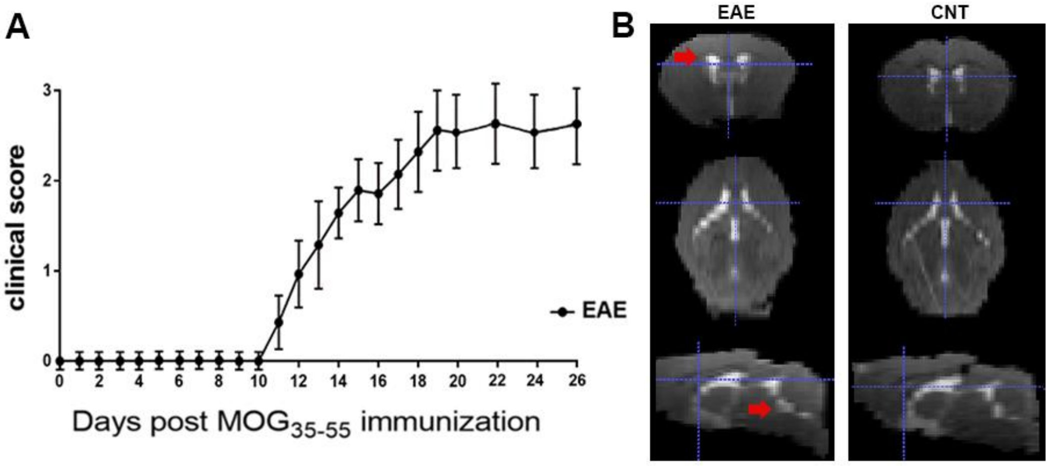

Figure 3.2.3 mean clinical score for EAE mice. Evaluations were performed before image acquisitions. B) T_2w images of one EAE versus, controls, not immunized mouse (CNT) at the peak of the disease. Change of contrast (pointed with red arrows) through the lateral ventricle (upper image) and cerebral acqueduct (lower image) is visible in EAE mice.

Control mice under anaesthesia regime during the rsfMRI protocol exhibited as well as EAE the same decrease in body temperature across MRI pipeline during anestesia protocol. Respiration rate (breaths per minute, bpm) monitored during the acquisition did not show significant variability between the two considered groups (Fig 3.2.4).

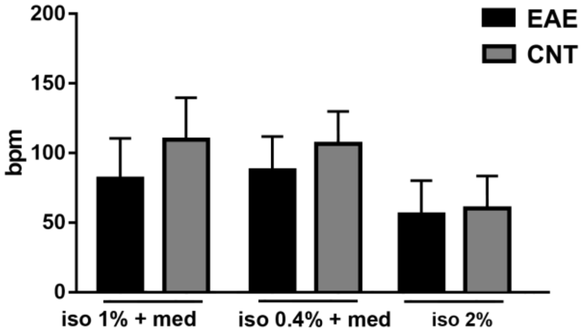

Figure 3.2.4. Breath rate per minute (bpm) expressed in y axis for the two groups as mean values + SEM. Different isoflurane concentration administered during rsfMRI experiment are shown below. EAE versus not immunized mice as controls (CNT). No statistical differences were found.

In Figure 3.2.5 the Pearson correlation coefficients for EAE and CNT are reported in a single matrix exploiting the symmetry of the matrix itself. In the following, the mean Pearson correlation coefficients will be referred to as Functional Connectivity (FC).

The FC matrices obtained for 54 ROIs showed different BOLD signal correlation patterns. It is noticeable a slightly increase in Pearson correlation coefficients in areas corresponding to the midbrain in mouse: inferior colliculus, inferior olivary complex, pontine nucleus, superior olivary complex, periaqueductal grey, medulla oblongata, midbrain, pons, interpeduncular nucleus and ventral tegmental decussation (Fig. 3.2.6).

The plain differences between obtained coefficients, as correlation values of EAE minus correlation values of CNT for each equal brain region, were also reported for visual inspection of functional connectivity networks in brain. In Figure 3.2.6 A, connectivity differences were negative in some regions, positive or near zero. For equal correlation values between EAE and CNT, it means that there are no differences in functional connectivity between the two groups, in the same area. It is possible with plain differences matrix to distinguish brain macroareas related to functional networks, not necessarily anatomical contiguous. To investigate if there were statistical significant differences in functional connectivity behaviour between not immunized mice and EAE, multiple comparisons test were performed. All considered correlations between regions were compared, applying false discovery rate correction. For multiple comparison test, p values below 0.05 were accepted as significant. First, functional connectivity differences between groups were thresholded. Brain regions which differences calculated as *EAE – CNT (correlation values)* below 0.5 were excluded. Statistical analysis focused on 10 regions, from different functional network. In Fig. 3.2.6 B multiple comparison results are reported as p values for brain areas included in basal, brainstem, cerebellum, cortex, somatosensory functional network. Also white matter areas were included, because of their correlation values differences. In particular, there was not significant changes in the white matter correlated to sensory network, while the brainstem and the cortex network connectivity were different between groups.

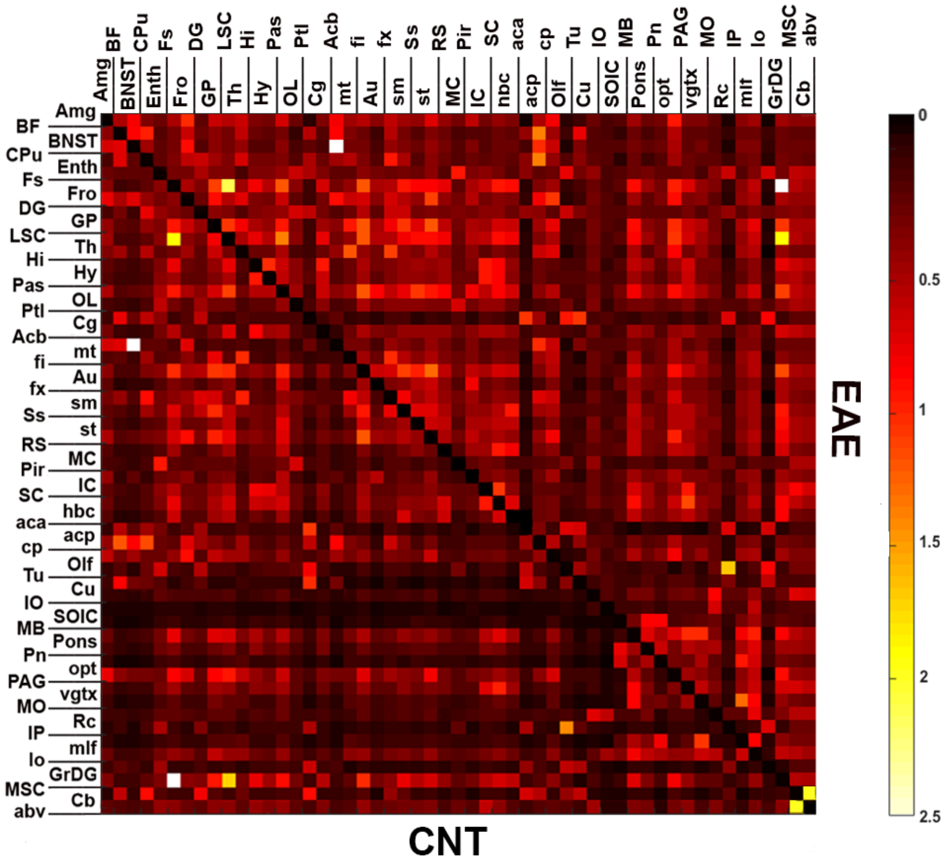

Figure 3.2.5. Pearson correlation analysis of BOLD strength signal, connectivity matrix; positive Z-Fisher transformed values. Half matrix below represents not immunized mice, as controls (CNT) while half matrix above the EAE mice, at chronic stage. Brain regions corresponded to Allen Mouse Brain Atlas, from Institute for Brain Science (AIBS), Common Coordinate Framework space (adapted for 4.7T resolution; CCF v3, © 2004 AIBS. Available from: http://www.brain-map.org/). Abbreviations are the following: *abv*= arbor vitae of cerebellum, *aca*=Anterior part commissure, *Acb*= nucleus accumbens, *acp*= posterior part commissure, *Amg* =Amygdala,

Au=Auditory cortex, *BF*= Basal Forebrain, *BNST*=Bed nucleus of stria terminalis, *cb*=cerebellum *Cg*=Cingulate anterior, *Cu*=Cuneate nucleus, *Enth*=Enthorinal region, *cp*= cerebral peduncle, *Cpu*= Caudate putamen, *DG*=Dentate gyrus, ,*fi*=fimbria, *Fro*=Frontal lobe, *Fs*= Fundus of striatum, *fx*=fornix, *GP*=Globus Pallidus, *hbc*=Habenular commissure, *Hi*=Hippocampus, Hy=Hypotalamus, *IC*=Inferior colliculus, *IO*=Inferior olivary complex, *LS*=Lateral septal complex/nucleus *MB*=Midbrain *MC*=Motor cortex, *mlf*= Medial longitudinal fasciculus ,*MSC* = medial septum, mt= mammillothalamic tract, *OL*=Occipital lobe, *Olf*=Olfactory bulb, *opt*=Optical tract, *PAG*=Periacqueductal grey, *Pas*=Parasubiculum, *Pir*=Piriform cortex, *Pn*=Pontine nucleus, *Pons*=Pons, *Ptl*=Parieto temporal lobe, *RS*= Retrosplenial cortex, *SC*= Superior colliculus, *sm*= stria medullaris, *SOIC*= Superior olivary complex, *Ss*= Somatosensory cortex, *st*=Stria terminalis, *Th*=Thalamus, Tu=olfactory tubercle, *vgtx*=ventral tegmental area.

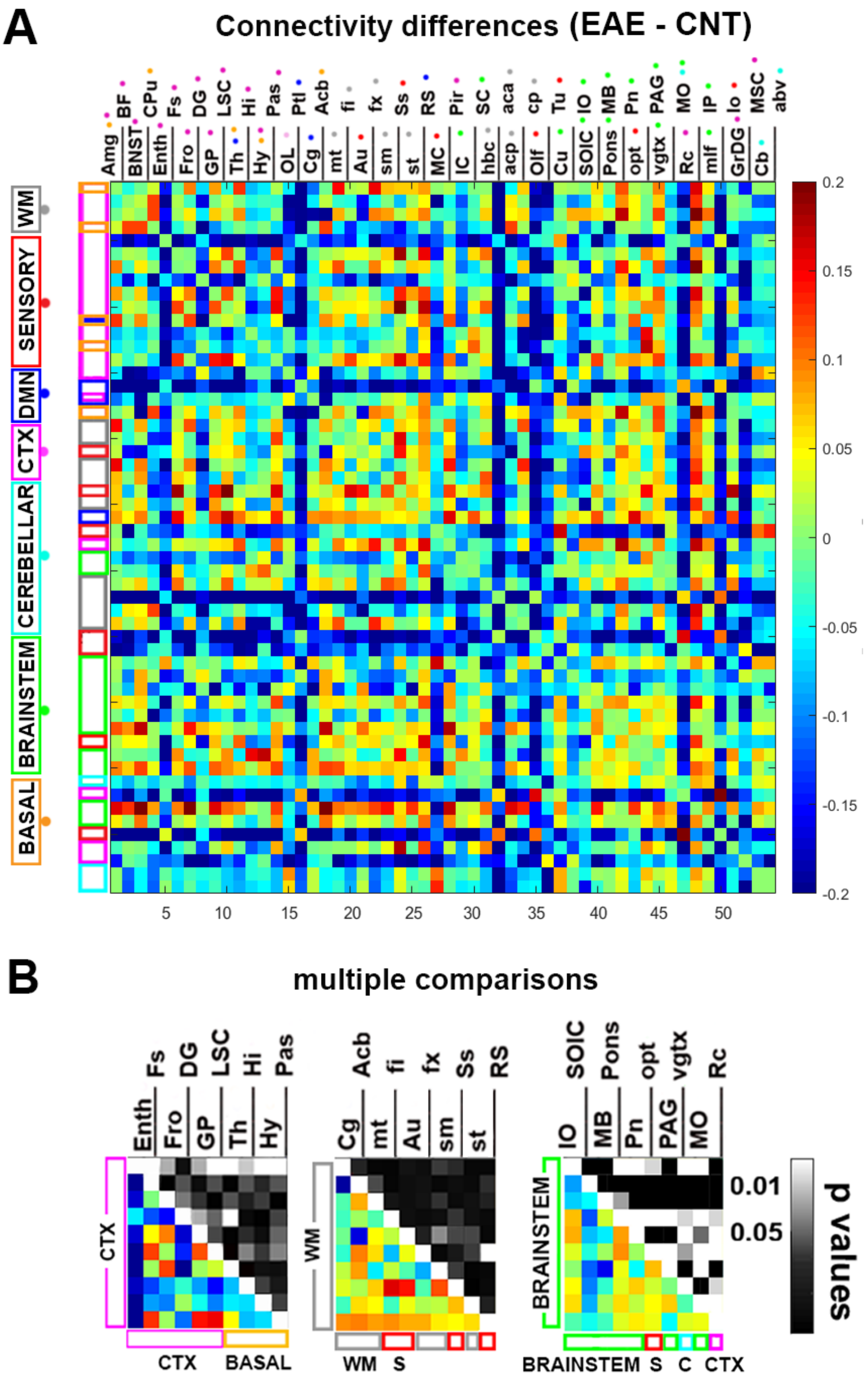

Figure 3.2.6 A) Connectivity strength differences matrix between EAE versus CNT, expressed in normalized values. B) Magnified representation of significative functional brain areas with lower triangle showing FC strength differences, in not immunized mice, versus EAE, at chronic stage. For each square, upper triangle represents p-values from multiple comparison analysis, thresolded to p = 0.05. Also functional network location (horizontal bar) vs anatomical location (vertical bar) is reported, referring to selected brain regions (short labels).

Connectivity strength was also reported for couple of regions from distinct functional networks (Fig. 3.2.7). The activity in the cortex increased in EAE mice as well as in the brainstem areas, involving the somatosensory area (indicated in the sensory network).

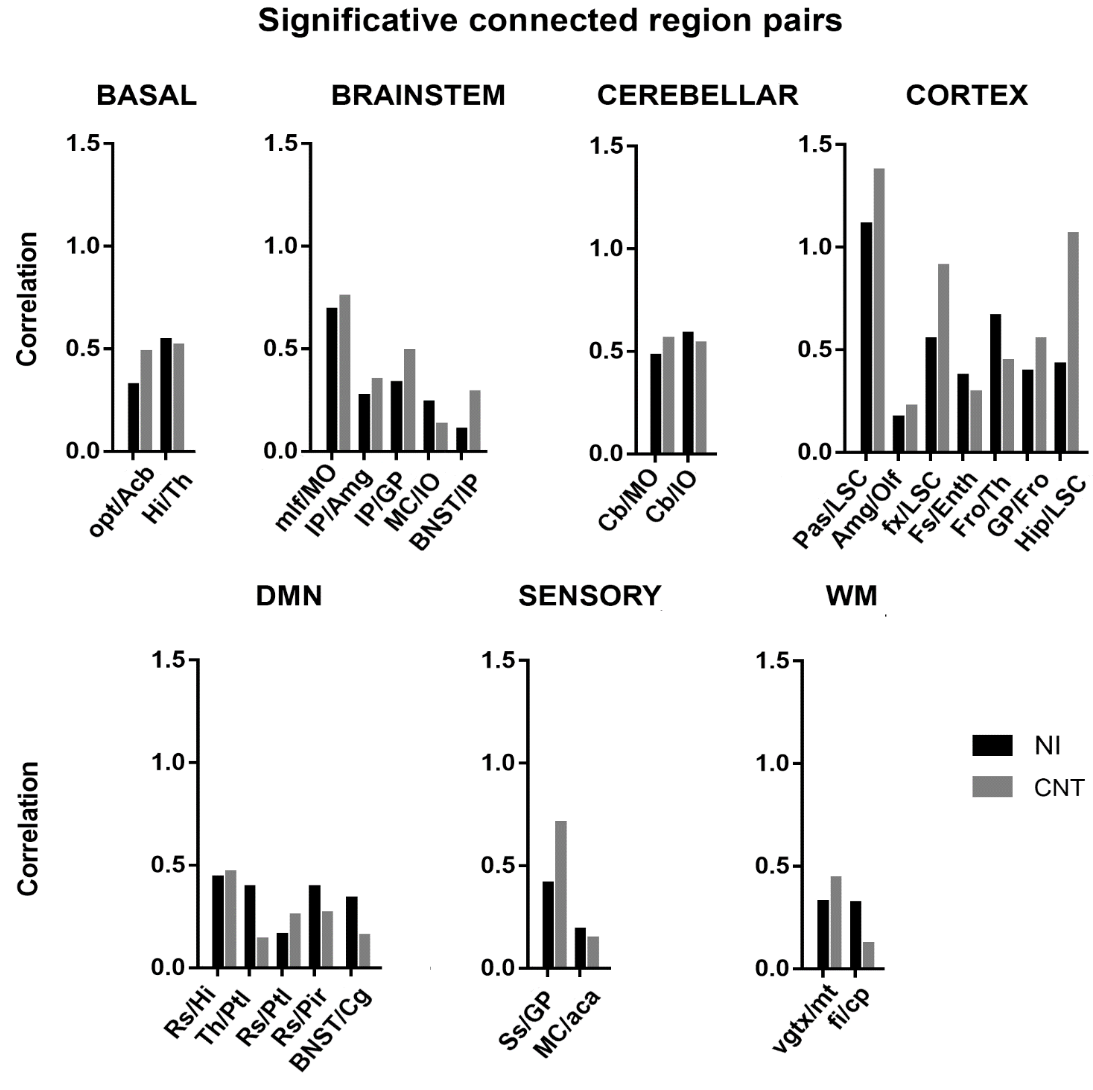

Fig. 3.2.7 Correlation strength between significant pairs of regions from different functional networks. Pearson coefficents from not immunized controls (CNT) and EAE mice were reported ad absolute values. Abbreviations are the following: *abv*= arbor vitae of cerebellum, *aca*=Anterior part commissure, *Acb*= nucleus accumbens, *acp*= posterior part commissure, *Amg* =Amygdala, *Au*=Auditory cortex, *BF*= Basal Forebrain, *BNST*=Bed nucleus of stria terminalis, *cb*=cerebellum *Cg*=Cingulate anterior, *Cu*=Cuneate nucleus, *Enth*=Enthorinal region, *cp*= cerebral peduncle, *Cpu*= Caudate putamen, *DG*=Dentate gyrus, ,*fi*=fimbria, *Fro*=Frontal lobe, *Fs*= Fundus of striatum, *fx*=fornix, *GP*=Globus Pallidus, *hbc*=Habenular commissure, *Hi*=Hippocampus, Hy=Hypotalamus, *IC*=Inferior colliculus, *IO*=Inferior olivary complex, *LS*=Lateral septal

complex/nucleus *MB*=Midbrain *MC*=Motor cortex, *mlf*= Medial longitudinal fasciculus , mt= mammillothalamic tract, *OL*=Occipital lobe, *Olf*=Olfactory bulb, *opt*=Optical tract, *PAG*=Periacqueductal grey, *Pas*=Parasubiculum, *Pir*=Piriform cortex, *Pn*=Pontine nucleus, *Pons*=Pons, *Ptl*=Parieto temporal lobe, *RS*= Retrosplenial cortex, *SC*= Superior colliculus, *sm*= stria medullaris, *SOIC*= Superior olivary complex, *Ss*= Somatosensory cortex, *st*=Stria terminalis, *Th*=Thalamus, Tu=olfactory tubercle, *vgtx*=ventral tegmental area.

For the between-group analysis, correlation matrix did not show particular pattern or huge brain network disruptions. Only some values are significant when EAE group was compared to controls at 20 days post immunization. Also independent component analysis was performed and ICs averaged per group. 25 IC were selected. GiftICA analysis showed significant components related to functional networks such as DMN and cortex (Fig. 3.2.8). Increased connectivity is found in EAE mice in other cortical areas, as well as in the brainstem. In particular, this analysis showed a connectivity component also at the extremities of the cerebellar area.

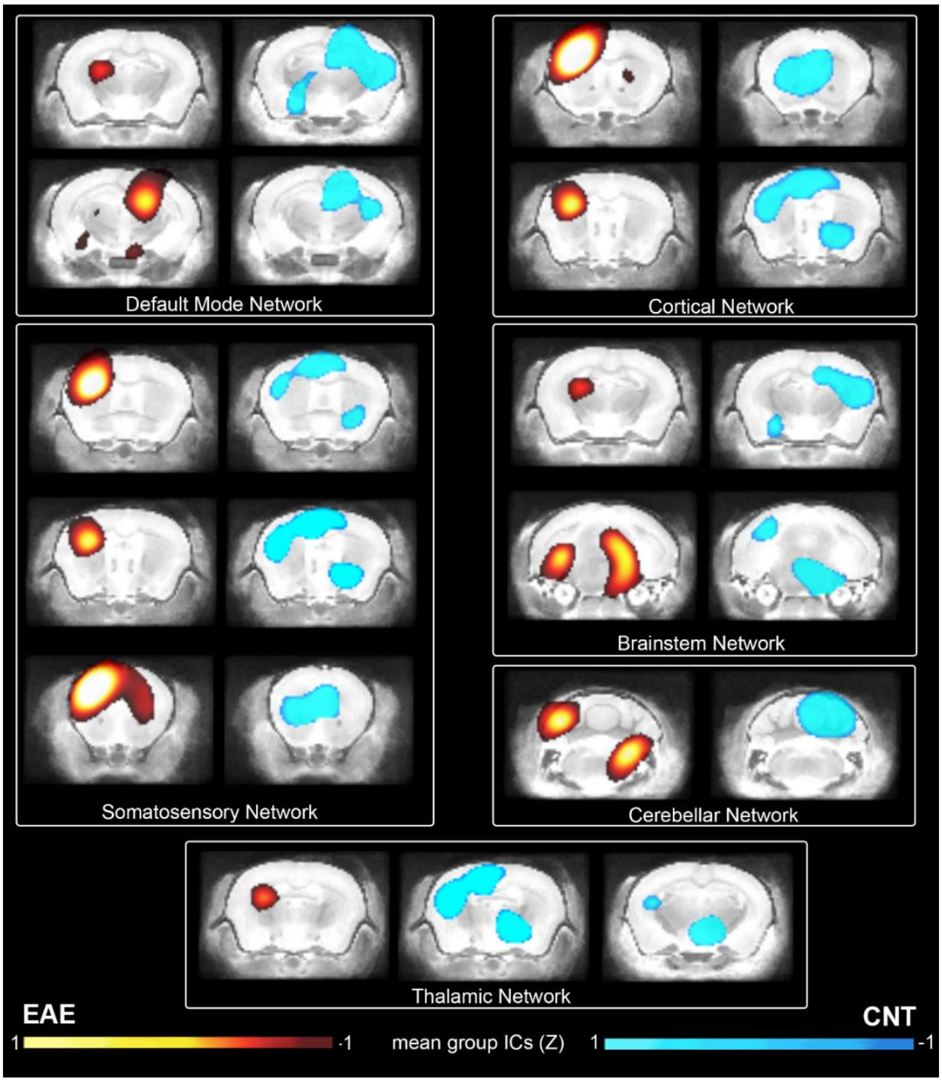

Figure 3.2.8. Functional connectivity networks by means of GiftICA. Survived Indipendent components (ICs) are shown overlayed onto the reference brain atlas. EAE mice (hot) and not immunized controls CNT (cool). ICs were Fisher z-score normalized (Z).

3.2.3 SOD-1 (G93A) transgenic mouse clinical score assessment

All animals were evaluated from the 50th day postborn, by means of the scale used in section 2.3, material and methods. PGE (paw grip extesion) and rotarod test were monitored to plan the MRI acquisitions at two different time points. Animals were considered at clinical onset at 85±5 days, end stage at 120±5 days postborn, accordingly to recorded values reported below (Fig. 3.2.3.1).

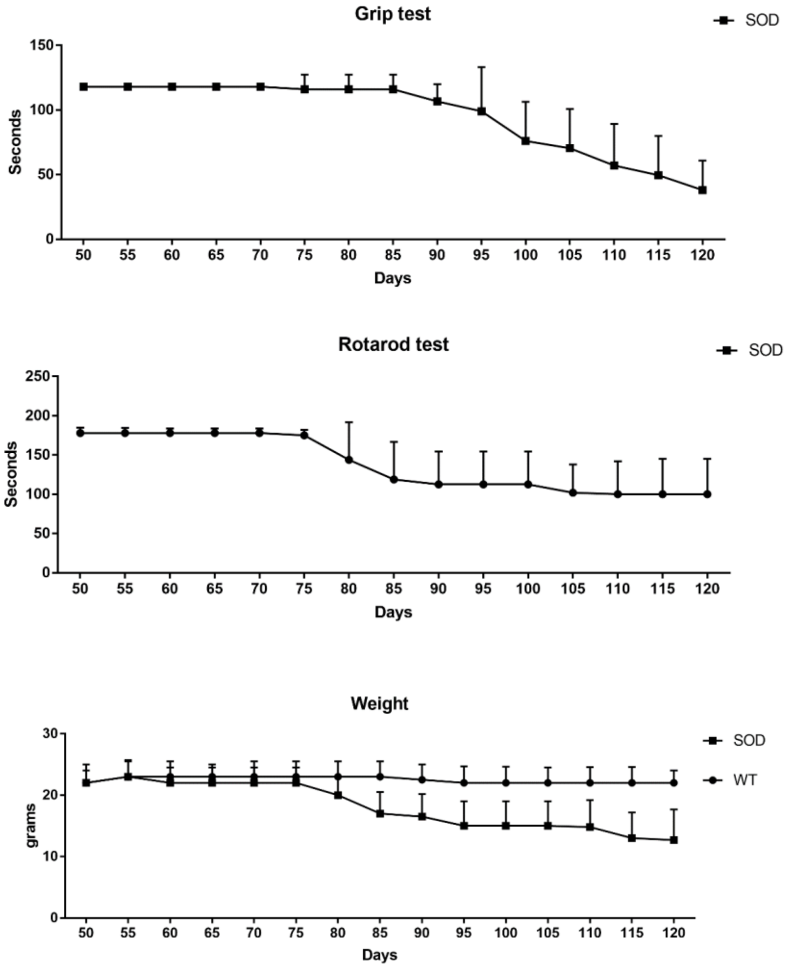

Figure 3.2.3.1. SOD1(93A) mice group monitored by means of paw grip extension (grip test) rotating rod endurance (rotarod test) expressed in seconds ± SEM during the overall study. Also weight was monitored and compared to control pool (WT).

3.2.4 rsfMRI acquisitions in SOD-1 (G93A) transgenic mouse

Physiological parameters under rsfMRI experiment, such as body temperature, breath rate and pCO_2, were monitored. The breath rate did not exhibit statistical differences between SOD-1 (G93A) transgenic mice and wild type control mice even at the end stage of the disease. No difference was also observed under different isoflurane concentrations (unpaired t-test analysis, Fig. 3.2.4.1). Body temperature and pCO_2 remained within acceptable limits. The experimental finding that no variations in physiological parameters occurred between WT and two different stage of disease in SOD mice, allows us to assume that BOLD signal was acquired without confounding parameters at free breathing regime.

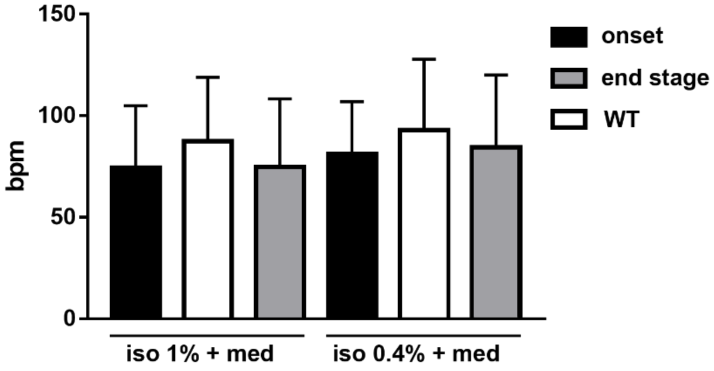

Figure 3.2.4.1 Mean values of measured breath rate per minute mice groups, SOD (at onset and endstage) WT controls, respectively, with different anesthesia regimes under rsfMRI experimental protocol.

Pathological alterations in brain of SOD-1 (G93A) mice were evaluated in T2w images that are acquired during the rsfMRI protocol after EPI acquisition (Fig. .2.4.2). Lesions appeared as hyperintense areas in T2w images in regions of the brainstem corresponding to the trigeminal and facial motor nuclei in 90- and 120-day-old mice.

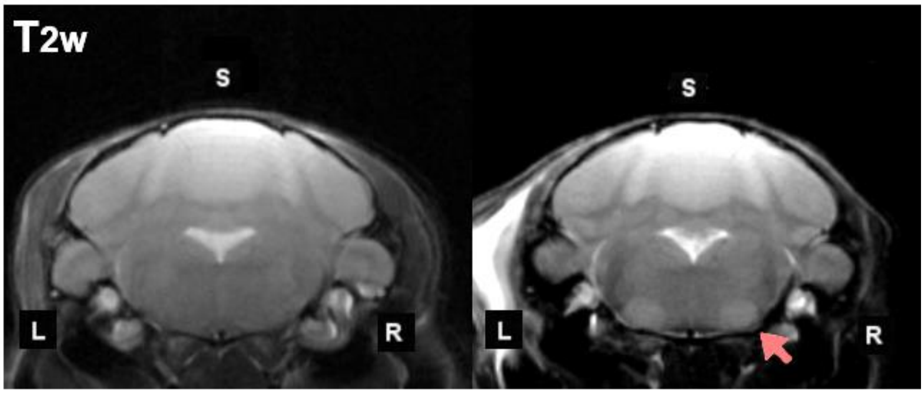

Figure 3.2.4.2. T_2 weighted images of coronal section from two representative mice. Right image show a control mouse, versus SOD at right , at onset stage. in SOD is visible a hyperintense region corresponding to interpeduncular nucleus, involved in the motor neuron system.

Correlation of BOLD signal per region across group were evaluated with $p < 0.005$ accepted as significant by means of Pearson correlation analysis. Results are reported in Figure 3.2.4.3.

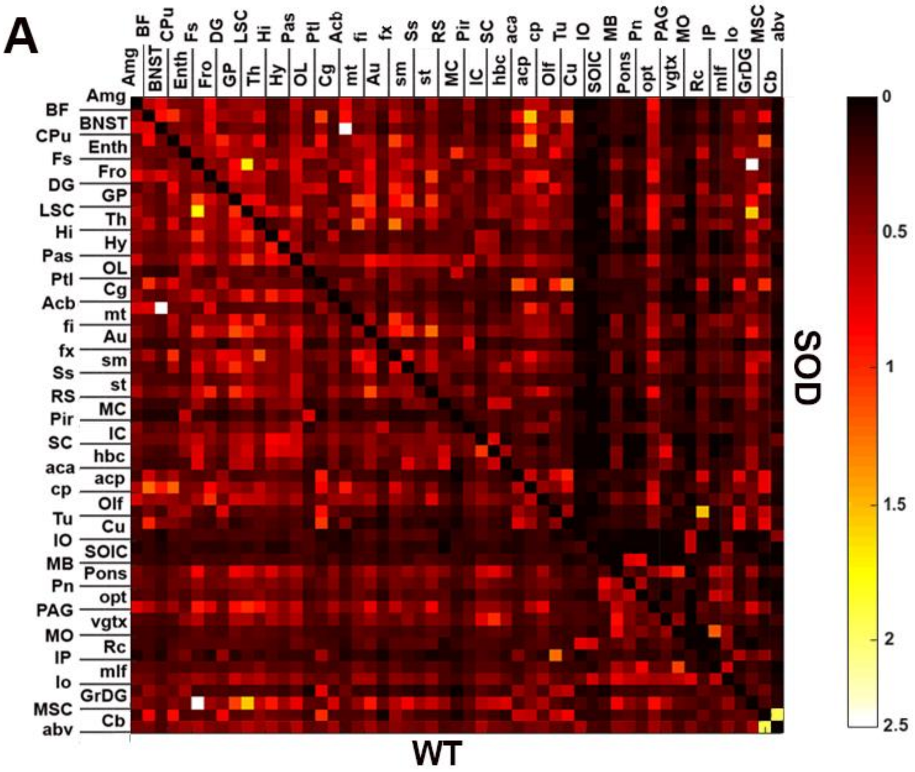

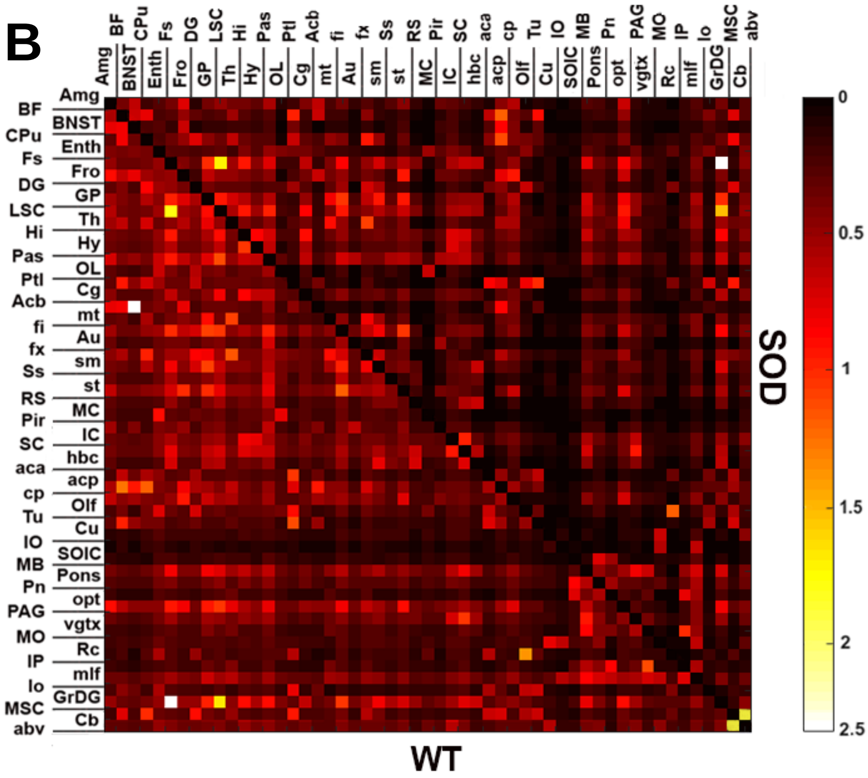

Figure 3.2.4.3. Pearson correlation matrices between different brain regions of interest, mean over all the two involved groups. The SOD group correlations are represented in the upper half of the matrix, while below were plotted correlations between brain regions in control (WT) mice, at the same age. SOD versus WT controls matrices of BOLD signal were calculated at onset stage A) and at the end stage of the disease B). Abbreviations are the following: *abv*= arbor vitae of cerebellum, *aca*=Anterior part commissure, *Acb*= nucleus accumbens, *acp*= posterior part commissure, *Amg* =Amygdala, *Au*=Auditory cortex, *BF*= Basal Forebrain, *BNST*=Bed nucleus of stria terminalis, *cb*=cerebellum *Cg*=Cingulate anterior, *Cu*=Cuneate nucleus, *Enth*=Enthorinal region, *cp*= cerebral peduncle, *Cpu*= Caudate putamen, *DG*=Dentate gyrus, ,*fi*=fimbria, *Fro*=Frontal lobe, *Fs*= Fundus of striatum, *fx*=fornix, *GP*=Globus Pallidus, *hbc*=Habenular commissure, *Hi*=Hippocampus, Hy=Hypotalamus, *IC*=Inferior colliculus, *IO*=Inferior olivary complex, *LS*=Lateral septal complex/nucleus *MB*=Midbrain *MC*=Motor cortex, *mlf*= Medial longitudinal fasciculus , mt= mammillothalamic tract, *OL*=Occipital lobe, *Olf*=Olfactory bulb, *opt*=Optical tract, *PAG*=Periacqueductal grey, *Pas*=Parasubiculum, *Pir*=Piriform cortex, *Pn*=Pontine nucleus, *Pons*=Pons, *Ptl*=Parieto temporal lobe, *RS*= Retrosplenial cortex, *SC*= Superior colliculus, *sm*= stria medullaris, *SOIC*= Superior olivary complex, *Ss*= Somatosensory cortex, *st*=Stria terminalis, *Th*=Thalamus, Tu=olfactory tubercle, *vgtx*=ventral tegmental area.

In order to get visual and qualitative findings from these data, the simple difference between between obtained Pearson's coefficients is reported below for the two disease stages, versus age-matched controls. Qualitatively we can appreciate a general decrease of FC in regions belonging to cerebellum and brainstem (see the blue part of matrix reported in Figure 3.2.4.4 A). To assess if there were statistical relevant changes between these regions, multiple comparisons test was performed for macro-regions similar to what performed in section 3.2.1. In particular, also the anatomical regions that included hyper intense T_2 weighted signal in the brainstem was added to this analysis. Brain regions in which extracellular superoxide dismutase (EC-SOD) is expressed, such as hilar region of hippocampus, i.e. dentate gyrus, thalamic region and inferior olivary complex were included in the multiple comparison analysis (Fig. 3.2.4.4 B).

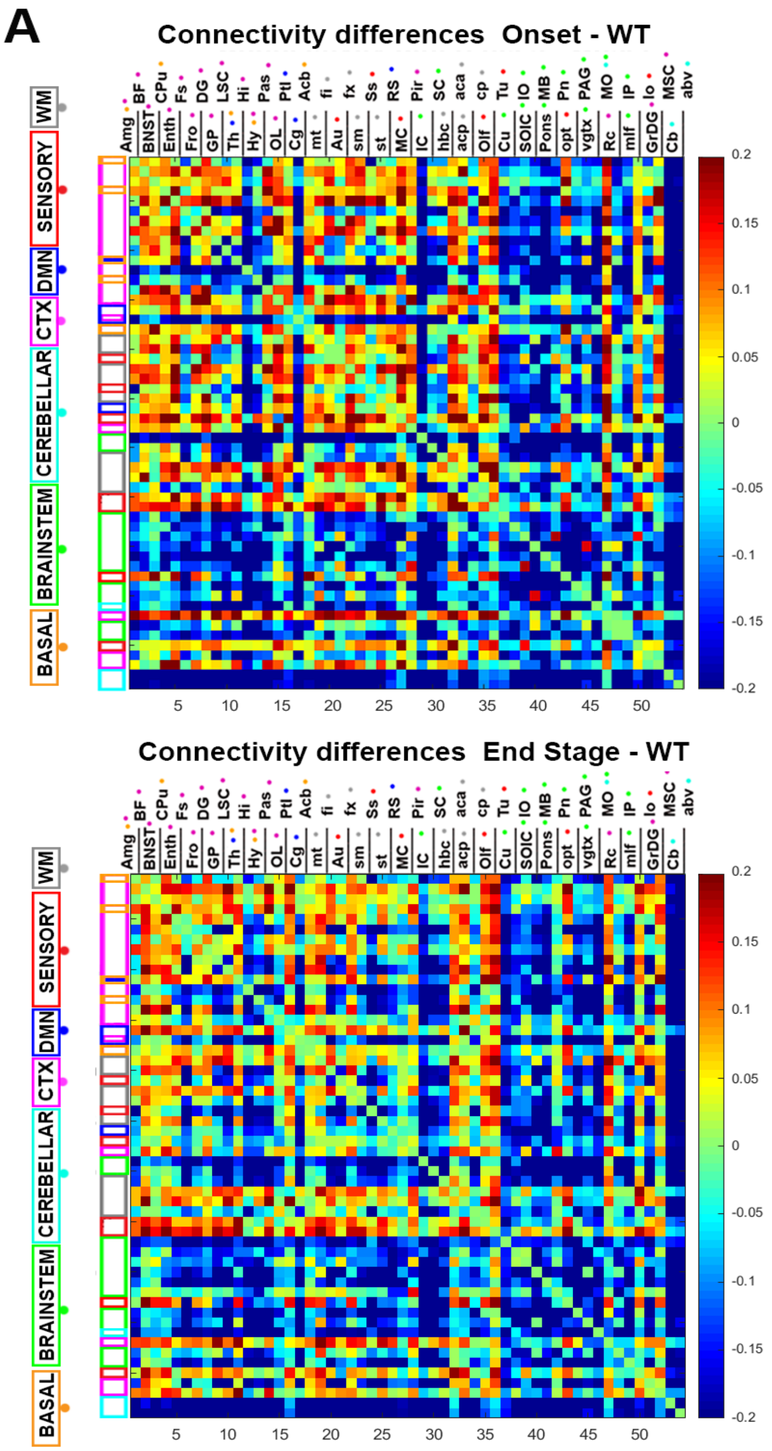

Figure 3.2.4.4. A) Connectivity differences between SOD mice and WT controls expressed as correlation values, for the two different stage of the disease (A). First symmetrical matrix represents differences between SOD at onset stage and second matrix below SOD at end stage minus WT mice age matching. Abbreviations are the following: *abv*= arbor vitae of cerebellum, *aca*=Anterior part commissure, *Acb*= nucleus accumbens, *acp*= posterior part commissure, *Amg*

=Amygdala, *Au*=Auditory cortex, *BF*= Basal Forebrain, *BNST*=Bed nucleus of stria terminalis, *cb*=cerebellum *Cg*=Cingulate anterior, *Cu*=Cuneate nucleus, *Enth*=Enthorinal region, *cp*= cerebral peduncle, *Cpu*= Caudate putamen, *DG*=Dentate gyrus, ,*fi*=fimbria, *Fro*=Frontal lobe, *Fs*= Fundus of striatum, *fx*=fornix, *GP*=Globus Pallidus, *hbc*=Habenular commissure, *Hi*=Hippocampus, Hy=Hypotalamus, *IC*=Inferior colliculus, *IO*=Inferior olivary complex, *LS*=Lateral septal complex/nucleus *MB*=Midbrain *MC*=Motor cortex, *mlf*= Medial longitudinal fasciculus , mt= mammillothalamic tract, *OL*=Occipital lobe, *Olf*=Olfactory bulb, *opt*=Optical tract, *PAG*=Periacqueductal grey, *Pas*=Parasubiculum, *Pir*=Piriform cortex, *Pn*=Pontine nucleus, *Pons*=Pons, *Ptl*=Parieto temporal lobe, *RS*= Retrosplenial cortex, *SC*= Superior colliculus, *sm*= stria medullaris, *SOIC*= Superior olivary complex, *Ss*= Somatosensory cortex, *st*=Stria terminalis, *Th*=Thalamus, Tu=olfactory tubercle, *vgtx*=ventral tegmental area.

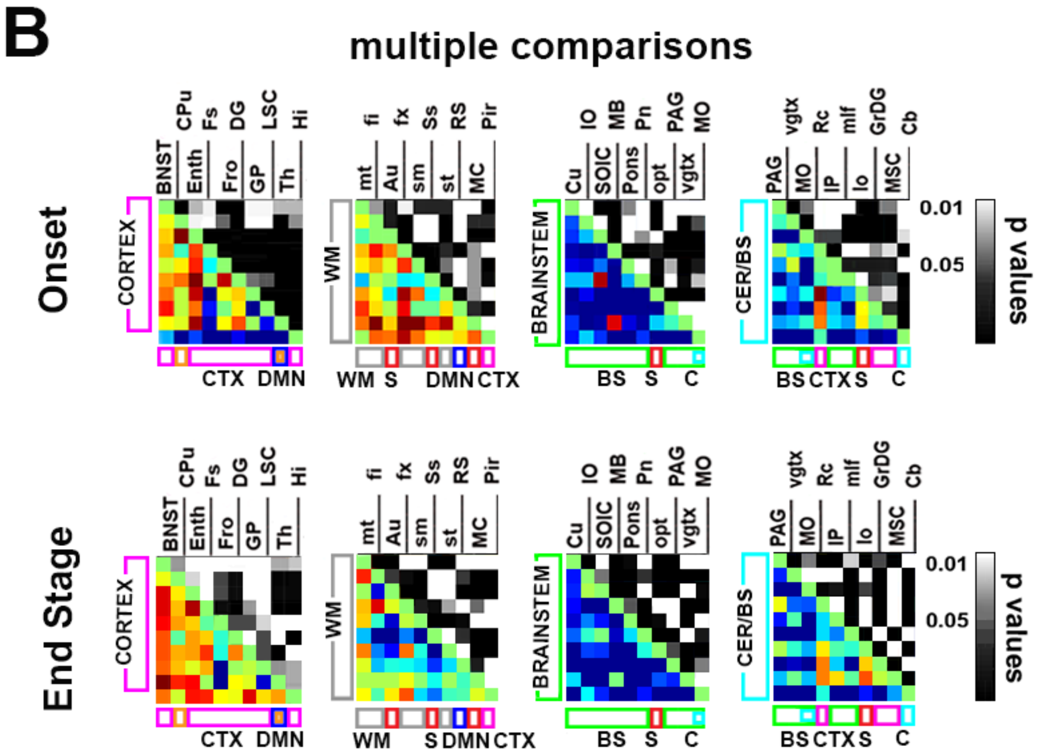

Fig. 3.2.4.4 B) multiple comparison analysis in sub areas of mouse brain between groups. For each square, upper triangle represents p-values from multiple comparison analysis, thresolded to p = 0.05. Also functional network location (horizontal bar) vs anatomical location (vertical bar) is reported, referring to selected brain regions (short labels). CTX = cortex, WM = white matter, BS = brainstem; CER/BS = cerebellar/brainstem area

A further evaluation was made comparing correlation strength between pairs of regions from different functional networks investigated. (Fig. 3.2.4.5). At the end stage of the disease, there is an increase in correlation strength in the default mode network and the cortex, except for the dentate gyrus / globus pallidus pair. A decrease in strength is visible in the cerebellar network GrDG/Cb pair, respectfully the onset stage.

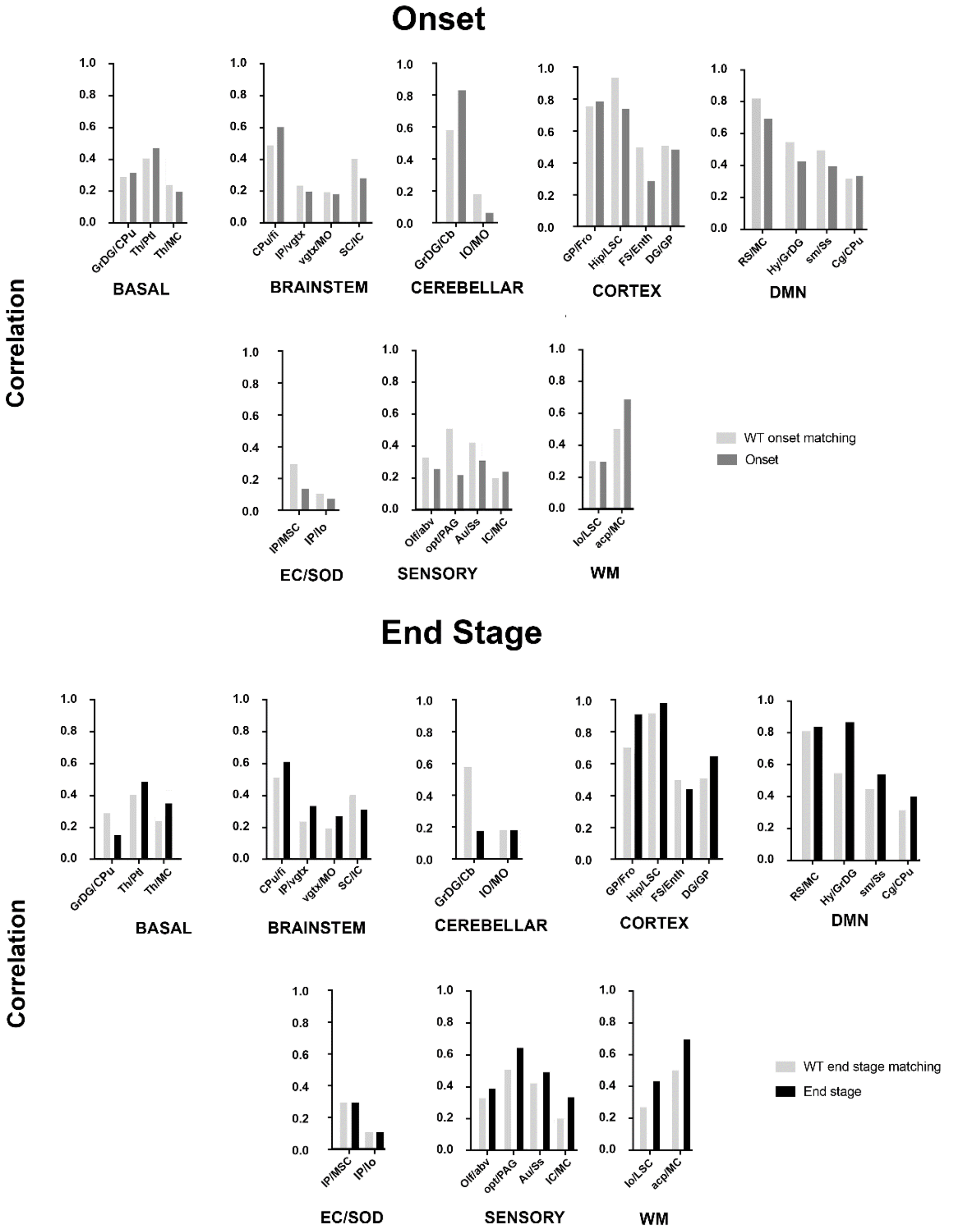

Figure 3.2.4.5 Connectivity strength comparisons between the two disease stages, respectfully to WT control mice FC at the same age. EC/SOD network is defined as pairs of brain regions involved in the enzymatic expression of the superoxide dismutase (EC) and where the hyper intense T2w areas were found in SOD mice at each stage.

GifICA results are shown in the panel below (Fig. 3.2.4.6); mean ICs from SOD mice and WT as controls were superimposed to anatomical rescaled Dorr reference atlas from section 2. ICs changed at onset and end stage in the cortical network; the cerebellar network showed ICs also. At the end stage, an additional IC is found overlapping the DMN but not somatosensory network, while ICs in the thalamic network were present only at onset stage.

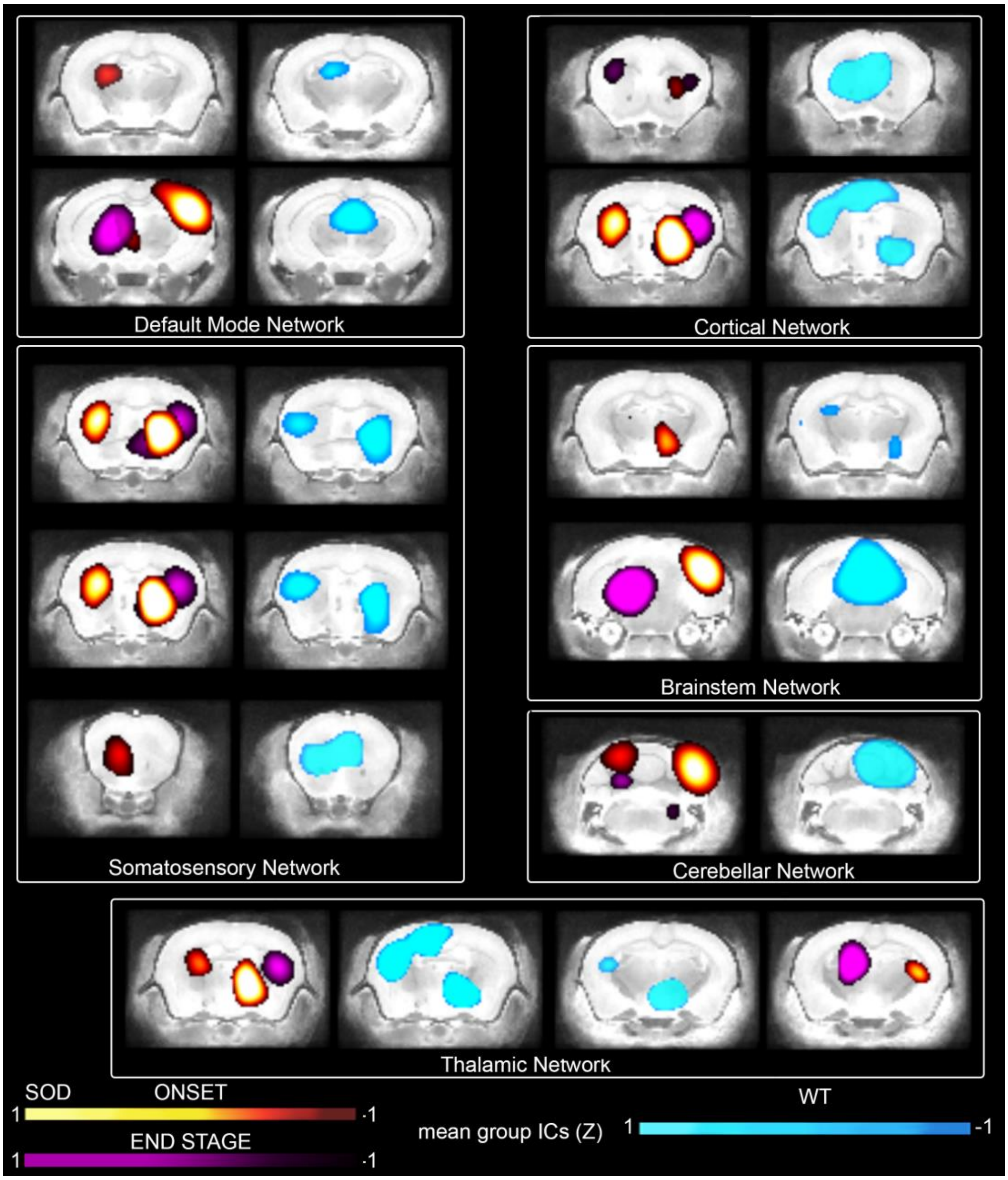

Figure 3.2.4.6 GiftICA ICs for groups at onset (hot) and end stage (violet) SOD mice versus WT (cool color coded) overlapped to the anatomical reference. ICs were Fisher z-score normalized (Z).

4. Discussion

4.1 Autoimmunity induced by adoptive transfer of Th17 cells: considerations about EAE model

The first part of the Results Chapter of the present thesis is dedicated to the findings in ex-vivo brain imaging and histology of the experimental model of EAE by adoptive Th17 cells transfer. Tg 2D2 mouse represents one of the chronic preclinical models initially used for investigation of optic neuritis. Lymphocytes from Tg 2D2 mice express the ability to change CD4+ cell subtype, polarizing them as Th17 precursors in vitro. It was reported that encephalopatogenity of Th17 populations is dependent upon cytokines secretion and can be disease effectors also in ocular inflammation in mice (Che, Chauhan, Shao et al, 2017), suggesting the passage of Th through the blood brain barrier.

In vitro Th17 cells can change the severity of the disease, because they possess the ability to produce also high levels of INF-y/Il-17, as it was assessed in this study by means of cytofluorimetry. This EAE model has features similar to symptoms of chronic MS. In the wide range of disease signs that are present in human MS, this model can reproduce balance problems or dizziness, and brain plaques. The combination of typical and atypical symptoms, previously reported and scored, is suggested by polarization/changing of Th17 into Th1. It is known that presence of Th1 induces EAE typical symptoms, that are related to hind limb paralysis and high level of inflammation in the spinal cord mostly (Domingues, 2010). In this model, neuropathological signs are visibile from the 10th day post injection. Encephalopathogenity of injected Th17 cell is not immediately expressed. This latency in EAE clinical signs suggested the hypothesis of interdepency, in the inflammatory process, of anatomical districts near the site of injection with Th17 cells. Duc et al. in 2019, reported in the same EAE model that gut microbiota can modulate the inflammatory outcome. In this paper was demonstrated that i.p. injected Th17 cells infiltrated the lamina propria in the mice gut, before reaching the CNS. These results could explain the dampering of the EAE symptomps in the used model, i.e. typical signs in mice mixed with atypical, and not always presents with the same intensity within subjects. Noticeable disease signs, that can be scored, are modulated by gut microenvironment in the first days p.i..

Histological findings showed the ability of injected Th17 cells to reach the CNS and recruit CD3 population, and MAC3/CD4 as well. The different cells infiltrates were detected in microphotographs mostly at the cerebellar and medulla oblungata areas, leading to focus on these brain regions while analyzing DTI results.

4.2 MRI correlates in EAE by adoptive transfer of Th17 cells: considerations about advantages and disadvantages of ex-vivo methods.

Neuroimaging findings were obtained in ex vivo fixed samples. Several experimental procedures required careful optimization in order to obtain meaningful results. Reported values from DTI in results section (3.1.3), for different brain areas ex-vivo are lower than in–vivo published ones in mice (Zhang, 2010). Because of overall lower diffusivity, higher b-values were needed to acquire meaningful data in the diffusion sequence with resulting low SNR. Moreover multiple b-values in DWI resulted in long acquisition times and therefore were possible only in ex-vivo experiments.

Another issue is represented by the perfusion procedure. Ex vivo and fixed brain tissues exhibit reduced T_1, T_2, and alterations in diffusivity, comparing the same tissues in vivo. Water relaxation is altered by fixative agents (formalin or PFA) and by tissue lower temperature than a living subject body (Sheperd, Thelwall et al., 2009). This means that fixed specimens, independently of pathology under investigation, compared to in-vivo, have reduced contrast to noise ratio in MRI.

Moreover, post-mortem interval (i.e. the time interval elapsed between sacrifice and tissue fixation) may irreversibly affect the microstructure of the tissue. Therefore, fixation via perfusion occurred at pre-mortem stage, by means of intracardial injection of fixative. However, the risk that the applied pressure of pumping could have induced microscopic damage in brain tissue and therefore introduced artefacts in the MR images remains.

DWI acquired with high number of b values at high magnetic field, showed that only fractional anisotropy (FA) and axial diffusivity (AD) were statistically significant, if measured in large brain areas, healthy mice compared to EAE. ROI based methods gave more evidence of changing of the other metrics, such as T_1 and T_2 times, RD and MD. This could be related to the predominant location of the lesions, medulla oblongata and arbor vitae area.

DWI measurements performed at high resolution showed statistically significant differences between EAE and healthy controls only in the fractional anisotropy (FA) and axial diffusivity (AD) parameters. In T1w and T2w images, the identification of lesions, asymmetrically distributed along the brainstem, was difficult. Moreover, histological results demonstrated high variability of inflammatory load and demyelination in the EAE subjects. Such heterogeneity in the inflammatory load and demyelination is detectable also in the spinal cord.

4.3 RsfMRI methodology at 4.7T: considerations about the overall experimental setup

Preliminary results from low magnetic field, respectfully to the state of the art in preclinical functional neuroimaging, showed that connectivity networks such as DMN, Sensory, Basal, Cerebellar and Brainstem (Liska, Galbusera, Schwarz et al., 2015) can be recovered at 4.7 T.

Major hindrances with EPI acquisition sequences are represented by long TE and image distortions. Acquired BOLD signal is dependent from anaesthesia regime, that was similar to previously reported studies, in which low doses of isoflurane does not affect brain cortical networks (Grandjean, Schroeter et al., 2014).

Physiological parameters were monitored and remained within physiologically acceptable range, despite free breathing (not forced ventilation) of mice.

Medetodimine is a-adrenegic agent (Sinclair, 2003), but may lead to side effects in the long time, that were controlled reducing at 10 minutes the overall EPI acquisition. Combined isoflurane and medetomidine regime seemed to not affect breath rate and oxygenation, between groups, in the two different experiments, probably because of short gaseous anaesthesia induction time.

Functional networks identified by means of FSL MELODIC enlightened significant correlations between cortical areas and somatosensory/brainstem networks. This method was used preliminarly to assess feasibility of 4.7T for resting state experiments. All found networks from functional brain atlas and analysed by means of ICs are preserved, confirming previous study in which stationary functional connectivity at 1.1% isoflurane is still detectable in mice (Bukhari, Schroeter and Rudin, 2018). Spontaneous head movements causes fluctuation of signal that can be excluded as confounding, thanks to FSL/SPM corrections and data cleaning. Two software were used to pre-process, smooth and clean all the datasets. One flexible, SPM combined with GIFTICA, and one less, FSL, combined with MELODIC without differences in pre-processing pipeline, because of the algorithms shared in common between toolboxes. Choice of SPM tool for main experiments with EAE and SOD was made to include more brain areas and select respective functional networks. Moreover FSL is tailored for human brain studies, and focusing on cleaning signal components on BOLD that reflects different conditions comparing to mouse brain. Automation in processing FSL pipeline would require high knowledge of good/bad signal in resting state. In this study, no ventilation to mice was applied. Thus physiological parameters, such as temperature and bpm under anaesthesia should be included in the pre-processing in further studies, with more animals. However, major functional rs mouse brain networks reported in literature, disrespectfully of selected software, can be observed and recovered at 4.7 T.

4.4 rsfMRI correlates in EAE mice by MOG/Ptx immunization

Obtained data suggested that alterations in FC are detectable in EAE mice also at low magnetic field. A general trend toward an increase in FC was observed in EAE mice at the 25th day post induction. Most of the elements in the correlation matrix were below the threshold of significance, while some regions were significantly functionally correlated and differed between the two groups. It is very interesting that FC in the regions that defines cortex network increases in EAE animals (compared to CNT). The anatomical distribution of the region pairs showed that the FC increase was relative to anatomically contiguous brain regions (retrosplenial cortex, enthorinal region, frontal lobe). In particular, a loss in connectivity strength was found in cerebellum – inferior colliculus – motor cortex areas (see fig.3.2.6 in result section, in which Frontal lobe –Thalamus, Motor cortex – inferior colliculus and cerebellum - pairs showed decreased FC). This is consistent with previous studies in which MS patients had both decreased and increased values of FC.

In recently reviewed FC data in MS, specific brain areas of many resting state networks showed that patients with clinically isolated syndrome have a higher FC than in either healthy subjects or relapsing-remitting MS, even though gray matter and white matter integrity are preserved (Tahedi, Levine, Greenlee et al., 2018). These findings are generally interpreted as a compensatory phenomenon: the coherence of cerebral activity increases at the earliest stages of the disease to limit the functional impact of structural damage but is subsequently lost in the late phase as a result of the progression of brain damage. It has been reported that brain reorganization, as expressed by changes in FC, is probably a dynamical process along the disease course and consequently we should consider the possibility that FC alterations could be slower than the evolution of the disease. It is unknown if these alterations could change between relapsing or remitting phase, or when the lesion is active. To date, longitudinal studies on humans are focused on VBM, perilesion area examination by means of other MRI techniques, with more attention on structural changes (Filippi, Rovasi and Rocca, 2004).

4.3 rsfMRI correlates in ALS SOD93A model

The necessity to define new biomarkers in the Amyotrophic Lateral Sclerosis (ALS) disease leads to combine new techniques with the available preclinical model in longitudinal studies. The transgenic line SOD1 (G93A) has histopathological outcomes similar to familiar and sporadic form in human beings, such as neuromuscular dysfunction, axonal and mitochondrial damage in spinal cord, while no significative features were reported in the brainstem and cerebellar/medullar region (Dal Canto and Gurney, 1997). We decided to monitor two stages of the disease, when early and severe motor deficits were accurately defined, to find functional correlates useful in future for non–invasively therapies testing. Moreover, motor neuron circuitry involves cortex and spinal cord. While alterations induced in the spinal cord have been widely investigated also in other neurodegenerative diseases, how the progression of the disease affects cortex is poorly understood. Studies reported in the literature focused on ALS using fMRI and rsfMRI combined to other brain activity measurements. To date, theories on compensatory events in the cortex, as well as inhibitions or dysfunction in some areas were reported (Proudfoot, Bede and Turner, 2019).

The SOD93A ALS model develops motor paralysis because of denervation of the neuromuscular junction. Ventral root axons and loss of alpha motor neurons are involved in the observed motor deficits. In particular, such neurons are located in the ventral tegmental area, (vgtx) and are connected to lower motor neuron circuit. The upper motor neurons, that are in the motor cortex, can receive inputs from long distance, through the corticospinal tract (for an extensive review, see Liang, 2011). These neurons have a long distance input also with thalamo-cortical neurons, as well as they receive cortical inputs (Sheperd, 2013). Upper motor neuron innervate also the spinal cord, but the connection between brain cortex and spinal cord is important to understand the model considered.

At onset stage, our results show connectivity increased towards the cerebellar area, while decreased towards the somatosensory cortex. This could be useful to identify a vulnerability period in the preclinical research, in which prodromal symptoms are not evident, and studying effectiveness of new therapies in the murine ALS model from different perspectives across time. Moreover, BOLD signal correlation loss across networks is more evident at onset than at end stage. It is interesting to note that functional connectivity change is related to the cortex, coupled with midbrain area, in which hyper intense region were detected in T2w images on SOD1 mice. One hypothesis could be the presence of compensatory phenomenon in default mode network and cortex.

Networks revealed by rsfMRI are related to loss of connectivity strength in some pairs of regions, such as dentate gyrus paired with caudate putamen, and cerebellum. Interestingly, an increase in connectivity strength was found for the thalamus-parietal lobe, and cingulate – caudate putamen pairs. These regions are related to brain areas in which extracellular superoxide dismutase (EC-SOD) is expressed (Oury, 1999). In this report, EC-SOD was observed in neurons of the hilar region of the hippocampus (DG), and also histological stainings revealed the same enzyme in tanycytes, a specialized cell population in the median eminence of the hypothalamus (Lechan, Fekete, 2006). One hypothesis correlates BOLD changes in this experiment because of modification of this cell population, because they project towards the 3^{rd} ventricle and contact the cerebrospinal fluid (Mullier, Bouret, 2010). While is know from literature that tanycytes are involved in the hypothalamic-pituitary-thyroid axis in mice (Muellr-Fielitz, Stahr, Bernau et al, 2017), their role remains to be further investigated. Moreover, the brain areas conserved across species involved the thalamic tract, more than the cerebellar areas, playing an important role in the control of movement. The ventral region of thalamus is interconnected with the globus pallidus, pontine nucleus with afferents towards the cerebellum and cortex and somatosensory spinal cord. Moreover, the motor neuron network has projections to the brain towards the ventrolateral hindbrain ("below the cerebellum") to regulate motor functions. It is unknown if the different SOD1 isoform can affect the mouse brain, modifying also connectivity. The loss of connectivity at end stage in the previously reported regions is compatible to neuron loss reported in Caron et al. (idem, 2015), in which additional hyper-intense imaged brain areas were found at higher magnetic field.

5. Conclusions and future developments

The aim of the present thesis was to validate functional biomarkers related to the disease evolution in experimental models of neurodegenerative pathologies. It is well known that in MS patients health status is not correlated to the number of active lesions observed in MRI. The clinical patterns of disease evolution and recovery symptoms are highly variable and scarcely correlated with structural CNS damage, as detected by MRI. It has been hypothesized that this scarce correlation, that has been referred to as clinical/MRI paradox depends on the efficacy of reparative mechanisms and interindividual variations in cortical reorganization and for this reason, attention was devoted to functional studies. An additional experimental model of neurological disease, namely Amyotrophic Lateral Sclerosis, ALS, was considered in the attempt to evaluate the potential usefulness of functional studies for the diagnosis of this pathology.

First it was implemented the protocol for resting state fMRI at 4.7T in healthy mice, then applied to MS and ALS preclinical models. Moreover, preliminary studies at structural level were conducted on Th17-induced EAE model. These experiments were conducted to include, in the future, the rsfMRI protocol in a different model of MS, that possess a higher degree in neuroinflammation and large brain lesions, if compared to the standard MOG-induced EAE. The two EAE models investigated recapitulate different clinical outcomes that are present mostly in chronic MS: a) loss of motor function, spinal cord inflammation (EAE MOG model); b) loss of motor coordination, mild and severe spinal cord inflammation (EAE Th17 transfer).

As far as the structural MRI study is concerned, our results show that diffusion metrics could represent a suitable marker in early stage of the pathology and could be a valuable tool to test new therapeutics if combined with other methods, such as flow cytometry of CD cell types. This need is crucial at present especially for progressive multiple sclerosis (Ontaneda, Thompson, Fox et al., 2017; Bermel, 2017).

In this thesis, a limited number of DTI metrics have been analysed yet. More efforts should be addressed in order to analyse other DTI metrics, including fiber tracking, in the cerebellar and brainstem area in mice. Cerebellum and medulla oblongata, in which most of the lesion were found, represent an important and developed area in mouse brain, as first anatomical connection to the spinal cord. More efforts could be addressed to the study of this area, by means of in-vivo diffusion and rsfMRI, because the medulla contains motor and interneuron populations and in Th17-induced EAE lesions are prominent in that brain portion.

In EAE Th17 transfer model inflammatory foci are driven by CD3/CD4 cells, while in MS patient also a source of inflammation is due to CD8. One hypothesis suggested is the association with Eptstein-Barr virus (Serafini, Rosicarelli 2019) and they represent the predominant population in MS lesions (Hayashi , Morimoto , Burks JS, Kerr et al., 1988).

Because of the hetereogeneity of inflammatory cells solicited by encephalopatogenic Th17, it would be interesting in future to investigate if there are different lesion "stages" in the brain, by means of in-vivo diffusion MRI.

The EAE model induced by MOG peptide has different clinical outcomes. The progression of the disease is slow and lesion are visible at the spinal cord level; moreover, imaging the spinal cord in mouse requires high magnetic field and expertise. In this work we focused on the CNS; we observed ventricle enlargement in anatomical images that suggested an inflammatory response in CNS, compatible to microglia activaction in the presymptomatic stage (Valente, Serratosa et al., 2017). Microglia are the primary immune cells and this cell population can spread in the CNS, explaining the brainstem/cortex network increased connectivity in chronic stage, as a compensatory phenomenon. A deeper investigation on RSN in EAE mice will require higher magnetic fields, always coupled with head coil (at 7T), in order to compare correctly morphometry with rsfMRI. RsfMRI data could be added to MS scoring scale in the clinical field, at the early stages of the disease. A recent report in MS patients combining RSN and T2w, suggests two types of correlation between FC and neurodegeneration (Castellazzi, DeBernard, Melzer et al., 2018). In this study, they suggested that a true compensatory mechanism in humans is related to areas of increased FC in the cuneus, precuneus, and superior frontal gyrus (structures that are not found in the mouse cortex). This means that one part of FC increase could be associated to other factors, as well as not all decreased FC networks are due to neurodegeneration per se. Future research on EAE on these basis will need rsfMRI method combined to morphological/structural study, for example using VBM, at longitudinal level, with acquisition at more time points.

It is known from the literature that modified SOD1 is representative of up to 10% ALS in humans. The autosomal dominant mutation in familial ALS of SOD1 is considered as major contributor in this neuropathology, but is still unclear how the mutant enzyme causes motor neuron degeneration. It has been recognized an early damage in extra motor regions in ALS (Trojisi, Sorrentino et al, 2017).

Thus, focusing on functional connectivity could elicit other questions on ALS pathology progression. Furthermore, there are not methodologies that can diagnose this debilitating disease at early stage, when there are not clinical evident signs. Obtained results could help understanding also pre-onset stage in SOD1, with the help of rsfMRI correlates. Recently, studies focused on early onset signs on SOD1 mice at 8 weeks of age, with subtle abnormalities in gait while striding a treadmill, but habituation of controls to repeated task gave differences between groups (Whooley, 2006). At this age, a true motor dysfunction cannot be detected with the same test (Guillot, 2008), suggesting a difficulty in reproducibility in motor test at pre symptomatic stages, that could be overcome by applying advanced MRI. Also the behaviour during SOD1 lifespan was recently analyzed between different phenotypes (Kreilaus, 2019). Researchers aimed to test several behavioural paradigms before the expected disease onset. Moreover, also spatial memory and conditioning were tested comparing male and female littermates versus WT. Findings suggested different patterns in SOD1 behaviour, recognition memory and response to stimuli before motor impairments. These series of methods could be useful to study mice DMN and memory as variables in SOD1 mice, when compared to controls, and correlate them to resting state networks. It is important for ALS preclinical model to keep in mind that mutant mice yield different genes and should be used to address different research questions.

In conclusion, in this thesis we have implemented rsfMRI methods in mice and obtained preliminary results in two experimental model of brain pathologies, MOG-induced EAE and SOD-1 ALS. Moreover the Th17-induced EAE model has been implemented, histological characterization and structural MRI data obtained.

At the best of our knowledge, rsfMRI has not been applied yet to EAE and ALS experimental models. Results are promising although they need validation at higher magnetic fields. Integration of functional and structural MRI methods could provide innovative surrogate imaging biomarkers that can constitute a platform to test the efficacy of new treatments, or other interventions. Such integration could improve the value of already assessed metrics in EAE and ALS and unravel the pathological progresses, along the disease evolution.

References

Amaro E. Jr, Barke G. J. (2006). Study design in fMRI: Basic principles. Brain and Cognition, 60, 220–232;

Aharonia R., Sasson E., Blumenfeld-Katzir T., Raya E., Sela M., Assaf Y., Arnona R., (2013) Magnetic resonance imaging characterization of different experimental autoimmune encephalomyelitis models and the therapeutic effect of glatiramer acetate. Exp. Neurol., 240, 130-44;

Badadani M, Nalbandian A, Watts GD, Vesa J, Kitazawa M, Su H, Tanaja J, Dec E, Wallace DC, Mukherjee J, Caiozzo V, Warman M, Kimonis VE (2010) VCP associated inclusion body myopathy and paget disease of bone knock-in mouse model exhibits tissue pathology typical of human disease. PLoS One, 5, 10;

Bajic D.,. Craig M. M.,. Mongerson Chandler R., Borsook D. and Becerra L. (2017) Identifying Rodent Resting-State Brain Networks with Independent Component Analysis. Front. Neurosci., 11, 685;

Bateman et al. (2012) Clinical and biomarker changes in dominantly inherited Alzheimer's disease. N. Engl. J. Med., 367, 795-804;

Barkhof F., Filippi M., Miller D.H. (1997) Comparison of MR imaging criteria at first presentation to predict conversion to clinically definite multiple sclerosis. Brain; 120: 2059–2069;

Basser P.J, Pierpaoli C. (1998) A simplified method to measure the diffusion tensor from seven MR images. Magn. Reson. Med. 39,928–934;

Bermel A. (2017) Unravelling neurodegeneration in multiple sclerosis. Comment on Lancet Neurology, 16: 764-767;

Bettelli E., Pagany M., Weiner H.L., Linington C., Sobel R. A. and Kuchroo V. K. (2003).Myelin Oligodendrocyte Glycoprotein–specific T Cell Receptor transgenic mice develop spontaneous autoimmune optic neuritis. J. Exp. Med. 5, 197(9), 1073–1081;

Belloli S., Zanotti L., Murtaj V., Mazzon C.,[7]Di Grigoli G., Monterisi C., Masiello V., Iaccarino L., Cappelli A., Poliani P. L., Salvatore Politi L and Moresco R.M. (2018).^{18}F-VC701-PET and MRI in the in vivo neuroinflammation assessment of a mouse model of multiple sclerosis. Neuroinflammation; 15: 33;

Bielschowsky M. (1903) Zur Histologie der Multiplen Sklerose. Neurol. Centralblatt 22:770–777;

Biomarkers Definitions Working Group (2011). Biomarkers and surrogate endpoints: preferred definitions and conceptual framework. Clin. Pharmacol. Ther., 69, 3, 89-95;
Brett M., Anton J., Valabregue R., Poline J.-B. (2002) Region of interest analysis using an SPM toolbox.8th International Conference on Functional Mapping of the Human Brain, June 2-6, 2002, Sendai, Japan. [abstract] NeuroImage, 16, (2);

Bucher S., Braunstein K.E., Niessen H.G., Kaulisch T., Neumaier M., Boeckers T.M., Stiller D., Ludolph AC. (2007). Vacuolization correlates with spin-spin relaxation time in motor brainstem nuclei and behavioural tests in the transgenic G93A-SOD1 mouse model of ALS. Eur. J. Neurosci. 26(7):1895-901;

Buchwalow I., Samoilova V., Boecker W, Tiemann M. (2011). Non-specific binding of antibodies in immunohistochemistry: fallacies and facts. Scientific Reports, 1, 28;

Biswal, B., Yetkin, F. Z., Haughton, V. M., and Hyde, J. S. (1995). Functional connectivity in the motor cortex of resting human brain using echo-planar MRI. Magn. Reson. Med. 34, 537–541. doi: 10.1002/mrm.1910340409;

Bontempi P., Busato A., Bonafede R., Schiaffino L., Scambi I., Sbarbati A., Mariotti R., Marzola P. (2017). MRI reveals therapeutical efficacy of stem cells: An experimental study on the SOD1(G93A) animal model. Magnetic resonance in medicine, 79:459–469;
Bukhari Q., Schroeter A., and Rudin M. (2018) Increasing isoflurane dose reduces homotopic correlation and functional segregation of brain networks in mice as revealed by resting-state fMRI. Scientific Reports, 8, 10591;

Castellazzi G., Debernard L., Melzer T. R., Dalrymple-Alford J. C., D'Angelo E., Miller D. H., Gandini Wheeler-Kingshott C. A. M., and. Mason D. F. (2018) Functional Connectivity Alterations Reveal Complex Mechanisms Based on Clinical and Radiological Status in Mild Relapsing Remitting Multiple Sclerosis. Front. Neurol., 9, 690;

Caron I., Micotti E., Paladini A., Merlino G., Plebani L., Gianluig F., Modo M., Bendotti C.(2015).Comparative Magnetic Resonance Imaging and Histopathological Correlates in Two SOD1 Transgenic Mouse Models of Amyotrophic Lateral Sclerosis. Plosone| 1:1-19;

Chandran P., Upadhyay J, Markosyan S, Lisowski A, Buck W, Chin C-L, Fox G, Luo F, Day M. (2012). Magnetic resonance imaging and histological evidence for the blockade of cuprizone-induced demyelination in C57BL/6 mice. Neuroscience; 202:446–453;

Cortese R., Collorone S., Ciccarelli O. and. Toosy A. T (2019).Advances in brain imaging in multiple sclerosis Ther. Adv. Neurol. Disord.; 12;

Collins, M. (2016). Electromagnetics in Magnetic Resonance Imaging: Physical Principles, Related Applications, and Ongoing Developments. Morgan & Claypool Publishers. Ch. 1;

Constantin, G., Laudanna, C., Brocke, S. & Butcher, E. C. (1999) Inhibition of experimental autoimmune encephalomyelitis by a tyrosine kinase inhibitor. J. Immunol. 162(2), 1144–1149;

Dal Canto M. C., Gurney. M. E. (1997). A low expressor line of transgenic mice carrying a mutant human Cu,Zn superoxide dismutase (SOD1) gene develops pathological changes that most closely resemble those in human amyotrophic lateral sclerosis. Acta Neuropathol (1997) 93:537–550;

Dietrich O., Heiland S., Sartor K. (2001). Noise correction for the exact determination of apparent diffusion coefficients at low SNR. Magn. Reson. Med. 45, 448–453;

Domingues H. S., Mues M., Lassmann H., Wekerle H., Krishnamoorthy G. (2010) Functional and Pathogenic Differences of Th1 and Th17 Cells in Experimental Autoimmune Encephalomyelitis. PLOS one, 5 (11): e15531;

Duc D., Vigne S., Bernier-Latmani J., Yersin Y., Ruiz F., Gaïa N., Leo S., Lazarevic V., Schrenzel J., Petrova T.V., Pot C. (2019) Disrupting Myelin-Specific Th17 Cell Gut Homing Confers Protection in an Adoptive Transfer Experimental Autoimmune Encephalomyelitis. Cell Rep. 8, 29(2), 378-390;

Falangola MF., Guilfoyle DN., Tabesh A., Hui ES., Nie X., Jensen JH., Gerum SV., Hu C., LaFrancois J., Collins HR., Helpern J.A. (2014) Histological correlation of diffusional kurtosis and white matter modeling metrics in cuprizone-induced corpus callosum demyelination. NMR in Biomedicine, 27, 8, 948–957;

Fjær S, Bø L, Lundervold A, Myhr K-M, Pavlin T, Torkildsen Ø, Wergeland S. (2013). Deep gray matter demyelination detected by magnetization transfer ratio in the cuprizone model. PLoS ONE, 8, 12, e2632.

Filippi M., Rovaris M., Rocca M. A. (2004) Imaging primary progressive multiple sclerosis: the contribution of structural, metabolic, and functional MRI techniques. Multiple Sclerosis Journal , 10, 3;

Fridovich, I. (1986). Superoxide dismutases. Adv. Enzymol. Relat. Areas Mol. Biol. 58, 61–97;

Fogarty M. J., Mu E. W. H., Noakes P. G., Lavidis N.A. and Bellingham M. C.(2016) Marked changes in dendritic structure and spine density precede significant neuronal death in vulnerable cortical pyramidal neuron populations in the SOD1G93A mouse model of amyotrophic lateral sclerosis. Acta Neuropathol. Commun., 4- 77;

Gozzi A., Schwarz, Grandjean J., Canella C., Anckaerts C., Ayranc G. , Bougacha S., Bienert T., Buehlmann D. , Coletta L., Gallino D., Gass N. , Garin C. M., Nadkarni N. A., Hübner N. S., Karatas M., Komaki Y., Kreitz S., Mandino F., Mechling A. E., Sato C., Sauer K., Shah D., Strobelt S., Takata N., Wank I., Wus T., Yahata N., Yeow L. Y., Yee Y., Aoki I., Mallar M. C, Chang W., Dhenain M., Elverfeldt D., Harsan L. , Hess A., Jiang T., Keliris G. A., Lerch J. P., Meyer-Lindenberg A., Okano H., Rudin M., Sartorius A., Van der Linden A., Verhoye M., Weber-Fahr W., Wenderoth N., Zerbi V.,Gozzi A. (2019). Common functional networks in the mouse brain revealed by multi-centre resting-state fMRI analysis. Neuroimage, 205, 166278, 3-11;

Grützkau A., Radbruch (2010). Small but mighty: How the MACS®-technology based on nanosized superparamagnetic particles has helped to analyze the immune system within the last 20 years. Cytometry. 77A: 643647-2010;

Guglielmetti C, Veraart J, Roelant E, Mai Z, Daans J, Audekerke JV, Naeyaert M, Vanhoutte G, y Palacios RD, Praet J, Fieremans E, Ponsaerts P, Sijbers J, der Linden AV, Verhoye M. (2016) Diffusion kurtosis imaging probes cortical alterations and white matter pathology following cuprizone induced demyelination and spontaneous remyelination. NeuroImage. 125, 363–377;

Guillot TS., Asress S.A, Richardson J.R., Glass J.D., Miller G.W. (2008). Treadmill gait analysis does not detect motor deficits in animal models of Parkinson's disease or amyotrophic lateral sclerosis. J Mot Behav. 40(6):568-577;

Gurney ME, Pu H, Chiu AY, Dal Canto MC, Polchow CY, et al. (1994) Motor neuron degeneration in mice that express a human Cu,Zn superoxide dismutase mutation. Science 264: 1772–1775;

Hamilton A.M., Forkert N. D., Yang R., Wu Y., Rogers J. A., Yong V. W. and Dunn J. F. (2019). Central nervous system targeted autoimmunity causes regional atrophy: a 9.4T MRI study of the EAE mouse model of Multiple Sclerosis. Sci. Rep., 9, 8488;

Hampson, M., Peterson, B.S., Skudlarski, P., Gatenby, J.C. and Gor, J.C. (2002). Detection of Functional connectivity using temporal correlations in MR image. Human Brain Mapping, 15,247–262;

Hayashi T., Morimoto C., Burks J.S., Kerr C., Hauser S.L. (1988) Dual-label immunocytochemistry of the active multiple sclerosis lesion: major histocompatibility complex and activation antigens. Ann. Neurol. 24, 523–531;

Hart B.A., Gran B. and Weissert R. (2011). EAE: imperfect but useful models of multiple sclerosis. Trends in Molecular Medicine 17, 3;

Heim B., Krismer F., De Marzi R. and Klaus Seppi (2017) Magnetic resonance imaging for the diagnosis of Parkinson’s disease. J. Neural. Transm. (Vienna). 124,8. 915–964;

Hennig J. A., Friedburg N. H (1986). RARE imaging: A fast imaging method for clinical MR. 3, 6, 823-833;

Hemmer B. and Mühlau M. (2016). Multiple sclerosis in 2016: Immune-directed therapies in MS - efficacy and limitations. Nature Reviews Neurology, 13, 72–74;

Henriques A., Pitzer C., Schneider A.(2010) Characterization of a Novel SOD-1(G93A) Transgenic Mouse Line with Very Decelerated Disease Development. PLoS One, 5,11, e15445;

Hohenfeld, Werner, C. J. and Reetz K.(2018) Resting-state connectivity in neurodegenerative disorders: Is there potential for an imaging biomarker? Neuroimage Clin., 18, 849–870;

Jaeger A., Dardalhon V., A. Sobel R., Bettelli E., Kuchroo K. V. (2009). Th1, Th17, and Th9 Effector Cells induce experimental autoimmune encephalomyelitis with different pathological phenotypes. The Journal of Immunology, 183: 7169–7177;

Jelescu IO, Zurek M, Winters KV, Veraart J, Rajaratnam A, Kim NS, Babb JS, Shepherd TM, Novikov DS, Kim SG, Fieremans E. . (2016) In vivo quantification of demyelination and recovery using compartment-specific diffusion MRI metrics validated by electron microscopy. NeuroImage, 132, 104–114;

Kingsley P.B. (2006) Introduction to Diffusion Tensor Imaging Mathematics: Part III. Tensor Calculation, Noise, Simulations, and Optimization Concepts in Magnetic Resonance Part A,Vol.28A (2), 155–179;

Kreilaus F., Guerra S., Masanetz R., Menne V., Yerbury J., Karl T. (2019). Novel behavioural characteristics of the superoxide dismutase 1 G93A (SOD1G93A) mouse model of amyotrophic lateral sclerosis include sex-dependent phenotypes Genes, Brain and Behavior., e12604;

Krishnan G.P., Gonzáleza O. C., Bazhenov (2018). Origin of slow spontaneous resting-state neuronalfluctuations in brain networks Giri .PNAS, 26, 115;

Lennon V., Wingerchuk D., Kryzer T., et al. (2004) A serum autoantibody marker of neuromyelitis optica: distinction from multiple sclerosis. Lancet, 364:2106–2112;

Liska A., Galbusera A., Schwarz A.J. and Gozzi A. (2015) Functional connectivity hubs of the mouse brain. NeuroImage, 115, 15, 281-291;

Liang H. (2011) Projections from the brain to the spinal cord in the mouse. PhD thesis, School of Medical Sciences, Faculty of Medicine, the University of New South Wales;

Likes R.S. (1979) Moving gradient zeugmatography, Schenectady, N.Y. Patent no. 292 1252 12/1979;

Ljunggren S. (1983). A simple graphical representation of fourier-based imaging methods. Journal of Magnetic Resonance, 54, 338-343;

Logothetis, N.K., Pauls, J., Augath, M., Trinath, T., Oeltermann, A. (2001) Neurophysiological investigation of the basis of the fMRI signal. Nature, 412, 6843, 150-157;

Logothetis Nikos K. (2003). The Underpinnings of the BOLD Functional Magnetic Resonance Imaging Signal. Journal of Neuroscience, 23 (10), 3963-3971;

Mainente A. (2019). Ottimizzazione della pipeline di analisi di dati rsfmri acquisiti su modello sperimentale di sclerosi laterale amiotrofica. Master thesis, University of Verona;

Marques J.P., Kober T., Krueger G., van der Zwaag W., Van de Moortele P., Gruetter R. (2010). MP2RAGE, a self bias-field corrected sequence for improved segmentation and T1-mapping at high field. NeuroImage 49, 1271–1281;

Masamoto, K. & Kanno, I. (2012). Anesthesia and the quantitative evaluation of neurovascular coupling. J. Cereb. Blood Flow Metab., 32, 1233–1247;

Matthew E.C., Serres S., Khrapitchev A. A., Stolp H. B. , Anthony D. C., Talbot K., Turner M.R. and Sibson N. R..(2014). T2-weighted MRI detects presymptomatic pathology in the SOD1 mouse model of ALS Journal of Cerebral Blood Flow & Metabolism (2014) 34, 785–793;

Meiboom, S.; Gill, D.(1958), Modified Spin-Echo Method for Measuring Nuclear-Relaxation Times. Rev. Sci. Instrum. 29, 688–691;

Mennes M., Kelly C., Colcombe S., Xavier Castellanos F., Milham M. P. (2013) The Extrinsic and Intrinsic Functional Architectures of the Human Brain Are Not Equivalent Cerebral Cortex, Volume 23, 1, 223–229;

Merkler D, Boretius S, Stadelmann C, Ernsting T, Michaelis T, Frahm J, Brück W. (2005) Multicontrast MRI of remyelination in the central nervous system. NMR in Biomedicine, 18, 6, 395–403;

Miana-Mena FJ, Munoz MJ, Yague G, Mendez M, Moreno M, Ciriza J, Zaragoza P, Osta R (2005) Optimal methods to characterize the G93A mouse model of ALS. Amyotroph. Lateral Scler. Other. Motor. Neuron. Disord. 6, 55–62;

Minati L, Weglarz WP. (2007).Physical foundations, models, and methods of diffusion magnetic resonance imaging of the brain: a review. Concepts Magn. Reson., 30A,278-307;

Mitchell J.D., Borasio G.D. (2007) Amyotrophic lateral sclerosis. Lancet 369: 2031–2041.

Neary, D., Snowden, J. S. and Mann, D. M. (2000). Cognitive change in motor neurone disease/amyotrophic lateral sclerosis (MND/ALS). J. Neurol. Sci. 180, 15–20;

Niessen H. G., Angenstein F., Sander K., W. S.Kunz, Teuchert M., Albert C. Ludolph, Heinze H., Scheich H., Vielhabera S. (2006). In vivo quantification of spinal and bulbar motor neuron degeneration in the G93A-SOD1 transgenic mouse model of ALS by T_2 relaxation time and apparent diffusion coefficient. Experimental Neurology, 201,2, 293-300;

Ontaneda D., Thompson A.J., Fox R.J., Cohen J.A. (2017) Progressive multiple sclerosis: prospects for disease therapy, repair, and restoration of function. Lancet; 389: 1357–66.

Ogawa, S. & Lee, T. M. (1990) . Magnetic resonance imaging of blood vessels at high fields: in vivo and in vitro measurements and image simulation. Magn. Reson. Med.16,9-18;

Ogura A., Watanabe H., Kawabata K., Ohdake R., Tanaka Y., Masuda M., Kato T., Imai K., Yokoi T., Hara K., Bagarinao E., Riku Y., Nakamura R., Kawai Y., Nakatochi M., Atsuta N., Katsuno M. and Sobue G.(2019). Semantic deficits in ALS related to right lingual/fusiform gyrus network involvement. EBio Medicine., 47, 506–517;

Ontaneda D., Thompson A.J., Fox R.J., Cohen J.A. (2017). Progressive multiple sclerosis: prospects for disease therapy, repair, and restoration of function. Lancet, 389: 1357–1366;

Ourya D., Patrick J.C., Klann E. (1999) Localization of extracellular superoxide dismutase in adult mouse brain. Brain Research, 850, 96–103;

Penny W., Friston K., Ashburner J., Kiebel S., Nichols T.(2011) Statistical Parametric Mapping: The Analysis of Functional Brain Images. London: Academic Press;

Proudfoot M., Bede P. and Turner M. R. (2019) Imaging Cerebral Activity in Amyotrophic Lateral Sclerosis. Frontiers in neurology , 9 ,1148, 8;

Polman C.H. , Reingold S.C., Edan G., Filippi M., Hartung H.P., Kappos L., Lublin F.D., Metz L. M, McFarland H. F., O'Connor P. W., Sandberg-Wollheim M., Thompson A., G. B. Weinshenker and Wolinsky J.S. (2005). Diagnostic Criteria for Multiple Sclerosis: Revisions to the "McDonald Criteria". Ann. Neurol., 58, 840–846;

Segal, B.M. et al. (2008) Repeated subcutaneous injections of IL12/23 p40 neutralising antibody, ustekinumab, in patients with relapsing-remittingmultiple sclerosis: a phase II, double-blind, placebocontrolled, randomised, dose-ranging study. Lancet Neurol. 7, 796–804;

Shah D, Deleye S, Verhoye M, Staelens S, Van der Linden A. (2016). Resting-state functional MRI and [18F]-FDG PET demonstrate differences in neuronal activity between commonly used mouse strains. Neuroimage. ;125:571–577;
Shepherd T.M., Thelwall P.E., Stanisz G.J. and Blackband S. J.(2009) Aldehyde Fixative Solutions Alter the Water Relaxation and Diffusion Properties of Nervous Tissue. Magn. Reson. Med. 62(1), 26–34;
Shepherd, G.M. (2013) Corticostriatal connectivity and its role in disease. Nat. Rev. Neurosci. 14, 278–291;
Singh S., Dallenga T., Winkler A., Roemer S., Maruschak B., Siebert H., Brück W. and Stadelmann C. (2017). Relationship of acute axonal damage, Wallerian degeneration, and clinical disability in multiple sclerosis. Singh et al. Journal of Neuroinflammation, 14-57;

Sinclair, M. D. A review of the physiological effects of alpha2-agonists related to the clinical use of medetomidine in small animal practice. Can. Vet. J. 44, 885–897 (2003);

Song S-K., Yoshino J., Le TQ., Lin S-J., Sun S-W., Cross A.H., Armstrong R.C. (2005) Demyelination increases radial diffusivity in corpus callosum of mouse brain. NeuroImage, 26(1), 132–140;

Sorbara C.D., Wagner N.E., Ladwig A., Nikic I., Merkler D., Kleele T., Marinkovic P., Naumann R., Godinho L., Bareyre F.M., et al. (2014).Pervasive axonal transport deficits in multiple sclerosis models. Neuron., 84, 1183–90;

Stafford JM., Jarrett BR., Miranda-Dominguez O., Mills BD., Cain N., Mihalas S., Lahvis GP., Lattal KM., Mitchell SH., David SV., Fryer JD., Nigg JT., Fair DA. (2014) Large-scale topology and the default mode network in the mouse connectome. Proc Natl Acad Sci U S A. 111, 52, 18745-18750;

Steinbach K. and Merkler D. (2015) Neuropathological Techniques to Investigate CNS Pathology in Experimental Autoimmune Encephalomyelitis (EAE) Methods in Molecular Biology, 1304, 189–209;

Stehling M. K., Turner R. and Mansfield P.(1991) Echo-planar imaging: magnetic resonance imaging in a fraction of a second. Science, 254, 5028;

Strimbu K. and Tavel J. A., What are Biomarkers? (2010) Curr. Opin. HIV AIDS, 5(6): 463–466;

Sun S-W., Liang H-F., Trinkaus K., Cross AH., Armstrong R.C., Song S-K. (2006) Non-invasive detection of cuprizone induced axonal damage and demyelination in the mouse corpus callosum. Magnetic Resonance in Medicine. 55, 2, 302–308;

Sunkin S. M. , Lydia N., Lau C., Dolbeare T., Gilbert T.L., Thompson C.L., Hawrylycz M. and Dan C. (2013) Allen Brain Atlas: an integrated spatio-temporal portal for exploring the central nervous system. Nucleic Acids Research, 2013, 41 996–1008;

Tagge I., O'Connor A., Chaudhary P., Pollaro J., Berlow Y., Chalupsky M., Bourdette D., Woltjer R., Johnson M., Rooney W. (2016). Spatio-temporal patterns of demyelination and remyelination in the cuprizone mouse model. PLoS ONE, 11, 4, 1–24;

Tahedl M., Levine M.S., Greenlee M. W., Weissert R. and Schwarzbach J. V. (2018) Functional Connectivity in Multiple Sclerosis: Recent Findings and Future Directions. Front. Neurol., 9:828;

Talbot, P. R., Goulding, P. J., Lloyd, J. J., Snowden, J. S., Neary, D., and Testa, H. J. (1995). Inter-relation between "classic" motor neuron disease and frontotemporal dementia: neuropsychological and single photon emission computed tomography study. J. Neurol. Neurosurg. Psychiatry 58, 541–547;

Tambalo S., Peruzzotti-Jametti L., Rigolio R., Fiorini S., Bontempi P., Mallucci G., Balzarotti B., Marmiroli P., Sbarbati A., Cavaletti G., Pluchino S., Marzola P.(2015). Functional Magnetic Resonance Imaging of Rats with Experimental Autoimmune Encephalomyelitis Reveals Brain Cortex Remodeling. J. Neurosci. 8, 35, 27, 10088-100100;

Turati L, Moscatelli M, Mastropietro A, Dowell NG, Zucca I, Erbetta A, Cordiglieri C, Brenna G, Bianchi B, Mantegazza R, Cercignani M, Baggi F, Minati L. (2014). In vivo quantitative magnetization transfer imaging correlates with histology during de- and remyelination in cuprizone-treated mice. NMR in Biomedicine, 28, 327–337;

Temple (1999). Are Surrogate Markers Adequate to Assess Cardiovascular Disease Drugs? JAMA, 282, 790-795;

Thiessen JD, Zhang Y, Zhang H, Wang L, Buist R, Del Bigio MR, Kong J, Li X-M, Martin M. (2013) Quantitative MRI and ultrastructural examination of the cuprizone mouse model of demyelination. NMR in Biomedicine, 26, 11, 1562–158;

Tintoré M., Rovira A., Martinez M. Rio J., Díaz-Villoslada P., Brieva L., Borrás C., Grivé E., Capellades J., Montalban X.(2000) Isolated demyelinating syndromes: comparison of different MR imaging criteria to predict conversion to clinically definite multiple sclerosis. Am. J. Neuroradiol. ,21,702–706;

Torkildsen Ø., Brunborg L. A., Myhr K.-M., Bø L. (2008). The cuprizone model for demyelination. Acta Neurologica Scandinavica, 117, 188, 72-76;

Tournier J.D., Mori S., Leemans A. (2011) Diffusion tensor imaging and beyond. Magn. Reson. Med. , 65,1532-1556;

Twieg D. (1983). "The k-trajectory formulation of the NMR imaging process with applications in analysis and synthesis of imaging methods". Medical Physics. 10, 5, 610–621;

Trojsi, F., Sorrentino P., Sorrentino G. and Tedeschi G. (2018). Neurodegeneration of brain networks in the amyotrophic lateral sclerosis–frontotemporal lobar degeneration (ALS–FTLD) continuum: evidence from MRI and MEG studies. CNS Spectr. 23(6):378-387;

Uitdehaag, Bernard M. J (2018) Disability Outcome Measures in Phase III Clinical Trials in Multiple Sclerosis. CNS Drugs, 32, 6, 543–558;

Valente T., Serratosa J., Perpiñá U., Saura J. and Solà C. (2017) Alterations in CD200-CD200R1 System during EAE Already Manifest at Presymptomatic Stages. Front. Cell Neurosci. 11, 129;

Wang, Xu G., Gonzales V., Coonfield M., Fromholt D., Copeland N. G., Jenkins N. A and Borchelt D. R. (2002) Fibrillar Inclusions and Motor Neuron Degeneration in Transgenic Mice Expressing Superoxide Dismutase 1 with a Disrupted Copper-Binding Site. Neurobiology of Disease, 10, 128 –138 ;

Weydt P., Hong S.Y., Kliot M., Moller T. (2003). Assessing disease onset and progression in the SOD1 mouse model of ALS. Neuroreport 14, 1051–1054;

Westphal R., Simmons C., Mesquita B.M., Wood T. C., Williams S. C. R., Vernon A. C., Cash D. (2017). Characterization of the resting-state brain network topology in the 6-hydroxydopamine rat model of Parkinson's disease. PLoS One, 12,3: e0172394.

Wooley C., Sher R. B., Kale. A., W. Frankel,. Cox G. A and. Seburn K. L, (2005). Gait analysis detects early changes in transgenic SOD1(G93A) mice. Muscle Nerve ,1, 43–50;

Wong, P. C., Pardo, C. A., Borchelt, D. R., Lee, M. K., Copeland N. G., Jenkins, N. A., Sisodia, S. S., Cleveland, D. W., & Price, D. L.(1995) An adverse property of a familial ALS-linked SOD1 mutation causes motor neuron disease characterized by vacuolar degeneration of mitochondria.Neuron14,1105–1116;

Wu Q-Z, Yang Q, Cate HS, Kemper D, Binder M, Wang H-X, Fang K, Quick MJ, Marriott M, Kilpatrick TJ, Egan GF. MRI identification of the rostral-caudal pattern of pathology within the corpus callosum in the cuprizone mouse model (2008). Journal of Magnetic Resonance Imaging, 27, 3, 446–453;

Xie H., Chung D., Kura S., Sugimoto K., Aykan S., Wu Y., Sakadžić S., Yaseen M., Boas D., Ayata C. (2019). Differential effects of anesthetics on resting state functional connectivity in the mouse. J. Cereb. Blood Flow Metab., 15, 271678;

Xie M, Tobin JE, Budde MD, Chen C-I, Trinkaus K, Cross AH, McDaniel DP, Song S-K, Armstrong RC. Rostrocaudal analysis of corpus callosum demyelination and axon damage across disease stages refines diffusion tensor imaging correlations with pathological features. Journal of Neuropathology & Experimental Neurology. 2010;69(7):704–716.

Yin H.Z, Nalbandian A., Hsu C.I, Li S., Llewellyn K.J, Mozaffar T., Kimonis V.E., Weiss J.H. (2012) Slow development of ALS-like spinal cord pathology in mutant valosin-containing protein gene knock-in mice. Cell Death Dis. 16; 3:e374;

Zang D. W., Yang Q., Wang Xin H., Egan G., Lopes E. C. and Cheema S. S. (2004). Magnetic resonance imaging reveals neuronal degeneration in the brainstem of the superoxidedismutase 1 G93A G1H transgenic mouse model of amyotrophic lateral sclerosis. European Journal of Neuroscience, 20, 1745–1751;

Zhang J. (2010) Diffusion tensor imaging of the white matter pathology in the mouse brain. Imaging Med. 1, (6), 623-632;

Zhang J, Jones MV, McMahon MT, Mori S, Calabresi PA. (2012). In vivo and ex vivo diffusion tensor imaging of cuprizone-induced demyelination in the mouse corpus callosum. Magnetic Resonance in Medicine, 67, 3, 750–759;

Zhou F., Zhuang Y., Gong H.,. Zhan J, Grossman M. and Wang Z., . (2016) Resting State Brain Entropy Alterations in Relapsing Remitting Multiple Sclerosis PLoS One; 11(1): e0146080;

Zucchi E., Ticozzi N. and Mandrioli J. (2019). Psychiatric Symptoms in Amyotrophic Lateral Sclerosis: Beyond a Motor Neuron Disorder. Front. Neurosci., 13, 175;

Appendix

This section covers the nomenclature, abbreviations and all reagents used for experiments reported in chapter 2.

A0. Abbreviations

2D2 MOG_{35-55} specific TCR

ALS amyotrophic lateral sclerosis

B6SJL-Tg(SOD1*G93A)1Gur/J GH1 transgenic mouse B6SJL crossed, high copy number gene

MRI magnetic resonance imaging

DMN default mode network

DWI diffusion weighted imaging

EAE experimental autoimmune encephalitis

EPI Echo Planar Imaging

FC functional connectivity

FUS fused in sarcoma RNA-binding protein

GE gradient echo

GRE gradient refocusing echo

HE Hematoxylin-Eosin

ICA independent component analysis

IC(s) independent component(s)

IHC immunohistochemistry

i.v. intravenous

i.p intraperitoneal

IR inversion time

LFB Luxol Fast Blue

PFA paraformaldehyde

PTx pertussis toxin

MS multiple sclerosis

RBC red blood cell

RF radiofrequency

rsfMRI resting-state MRI

s.c. subcutaneous

SD standard deviation

SE spin echo

SPM statistical parametric mapping

T1 spin-lattice relaxation time

T2 spin-spin relaxation time

TCR T-cell receptor

TE echo time

Th17 T-helper 17

TR repetition time

A1. Differentiation of T-cell in vitro from 2D2 mice

Adapted from Jaeger A., Kuchroo, 2013. Differentiation of T effector cells, uploaded content from Kuchroo laboratory; http://kuchroolab.bwh.harvard.edu/;

Cell strainer 70um
CD4 T cell isolation kit (130-104-454 ; Miltenyi Biotec)
RBC lysis Buffer (00-4333-57; eBioscience)
FoxP3 transcription factor staining set (00-5523-00, Life technologies)
MACS LS column (130-042-401; Miltenyi Biotec)

Cytokines/antibodies

hIL-2 (130-093-901; Miltenyi Biotec)
mIL-12 (210-12-10UG; Peprotech)
CD45-Amcyan (30-F11 ; 103138 ; Biolegend)
CD3 APC eFluor 780 (145-2C11; 47-0031-82; eBioscience)
CD4 alexafluor 700 (GK1.5; 56-0041-82; eBioscience)
CD44 alexafluor 647 (IM7; 103018; Biolegend)
IL-17A PE/Cy7 (eBio17B7; 25-7177-82; eBioscience)
IFNg FITC (XMG 1.2; 53-7311-82; eBioscience)
RORgT BV421 (Q31-378; 562894; Biolegend)

Reagents

Clone media in DMEM

Sodium Pyruvate	S8636-100ML Sigma	7.5mL
L-Glutamin (200mM)	5-10K00H Bioconcept	5mL
Penicilin-Streptomycin solution	4-01F-00H AMIMED	5mL
NEAA 100x	11140-035 Gibco	5mL
AA Arginine / Asparagine mix	Homemade, see below	5mL
FA Folic Acid solution	Homemade, see below	5mL
VIT Vitamin mix solution	M6985 Sigma	5mL
2-mercaptoethanol (50uM final)	21985-023 Gibco	455uL
FCS	N/A	50mL
DMEM	41965-039	500mL

AA Arginine / Asparagine mix
L-Arginine (11009-25G, Sigma FW: 174,2 g/mol, 0.7mM final) 1,16g
L-Asparagine (A0884-25G, Sigma FW: 132.1g/mol, 0,3mM final): 0.36g
Distilled H_2O up to 100mL

FA Folic Acid solution
Folic acid (F8758-25G, Sigma 14uM final) 0.06g
1N NaOH (A1551.1000, Applichem) 0.5mL
dH2O up to 100mL

MACS Buffer (BSA 0.5%; EDTA 2mM in PBS 1x)
BSA (A3912-100G; Applichem) 2.5g
EDTA 0.5M (46-034-Cl; Corning) 2mL
PBS 1X up to 500mL

FACS Buffer (BSA1% in PBS 1x)
BSA (A3912-100G; Applichem) 5.0g
PBS 1X up to 500mL

A2. EAE MOG/Ptx induced

complete Freund's adjuvant (Becton Dickinson)
Mycobacterium Tuberculosis (Becton Dickinson)
Pertussis toxin

A3. Anaesthetics and usage in animals

Perfusion Surgery in PBS 1M PFA 4%
Ketamine (Ketasol™) 0.6mL
Xylazine (Rompur™) 2% 0.4 mL
NaCl saline solution for injections: add up to 10 mL
Euthanasia
Barbiturates (Pentobarbital™) not diluted, IV or IP above 100mg/kg; sodium pentobarbital 390 mg/ml + sodium phenytoin 50 mg/ml

Hypnotic agents, with anaesthetic and analgesic effects with long time recovery
Agent: Medetomidine in NaCl solution: 0.1%
Antidote: Atipamezole in NaCl solution: 0.01%
Anaestethic gases with low effect of analgesia:
Isoflurane 2-2.5%, in 1lt O_2, accordingly to animal weight.
Isoflurane 1.5%, long time induction (up to 2 hrs) associated to gas vehicles N_2 and O_2 in line.

A4. Histology reagents

Equipment
Oven with adjustable temperature.
Surgical instruments: forceps, fine and blunt forceps, scissors, razor blades.
Glass/plastic ware for histology
Organic solvents: ethanol, isopropanol, isopropyl alcohol, Xylol (UltraClear™ clearing reagent, Avantor, Center Valley, USA)
Humified chamber
Acrylic brain matrix for coronal tissue sections, mouse brain, Alto

Bieschlowski staining

Development solution: liquid formalin (Merck®), 37% 20 mL
100 mL destilled water
0.5g citric acid monohydrate (Merck®)
15uL nitric at 65% (Merck®)
2% sodium thiosulfate pentahydrate (Merck®): 4 gr in 200 mL of distilled water
$AgNO_3$: 250 gr, M = 169.88 (Roth®)
NH_3 at 32% ammonia (Merck®)

LFB-PAS staining

EtOH 100% absolute, then diluted at 90%, 70% in distilled water
LFB solvent blue, 25 gr in acetic acid (ClinTech®)
Schiffs reagent (Sigma Aldrich®)
Mayer’s Hemalum, Merck
Lithium carbonate powder, 250 gr, (Merck®)
Periodic Acid (Sigma Aldrich®)
Xylene solution absolute (UltraClear™)

IHC
After dewaxing:
Antigen retrival: Pascal Citrate pH 6.0 or TRIS EDTA pH9.0;
Washing Buffer 10x : 100mL in 1lt destilled water;
Labelled polymer anti-rabbit HRP (Dako Real);
Substrate Buffer & DAB chromogen (x50) (Dako Real)
Peroxidase Blocking solution (Dako Rea)l;
Antibody diluent (Dako Real);
Antibodies:

Polyclonal rabbit anti-Olig2 IgG
MAC3 Biolegend clone M3/84 coupled with Fab Fragment Fragment Goat anti-mouse IgG;
CD4 Rabbit mAb (Cell signalling Dako D7D2Z), CD3 antimouse (Abcam®)

A.5 Generic Pulse diagrams and nomenclature

A pulse diagram is composed by several parts that combine each other to generate the image. RF indicates the radiofrequency applied, while gradients (G) are added for different purpose to achieve the best spin re-phasing. G_x, G_y, G_z in plane directions could be represented in terms of phase encoding, G_{PE}, or frequency encoding, G_{FE}. Sometimes readout is separated, RO, also called G_{FE} gradient, that is applied when receiver component are turned on. The object is imaged in its frequency encoding, because G_{FE} is active during the formation of the echo.
Signals are generated by resonance effect. Lines represents at each row of the diagram the timeline of the events; often the ADC acquisition part and slice selection, SS, that include the electronical part of the instrument, are involved in the picture. Diagrams can differ in form, but they maintain the concept in a timeline once the method, i.e. the sequence, is applied. As rule of thumb, the shape of the frequency varies in function of the pulse shape (rectangular, short rectangular or block pulses; Gaussian, sinc1, sinc3). The amplitude of the phase encoding gradients, slice excitation, is depicted as length in trapezoidal shape. Negative or positive follows the z-plane, in which the formalism included the static magnetic field, namely B_0. Dashed blocks represents the encoding steps. If the pulse diagram is read in columns, each symbol in the line represents the event that happens at the same time.

T2w

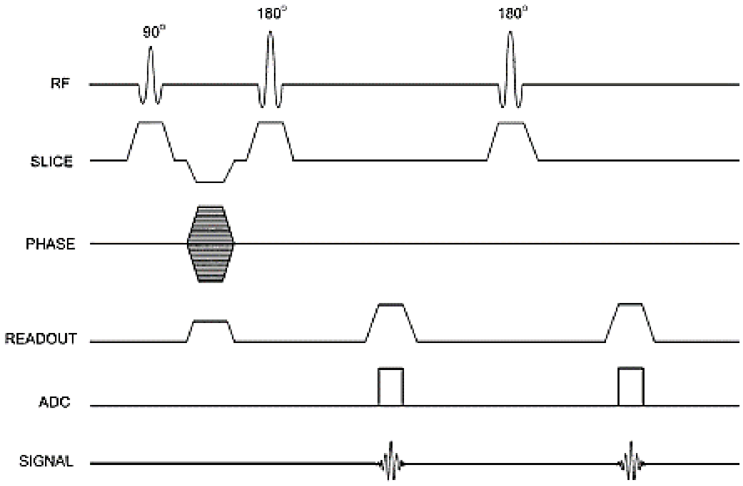

Pulse diagram of multi echo spin echo sequence across time; this representation may slightly vary across literature. All the lines proceed simultaneously in MRI experiment. The RF reflect angles from the reference plane x. Slice is the volume of the object that receives the RF pulses. Phase and readout are the encoding parts, while the ADC operates while the signal is detected (Meiboom, 1958).

T1w

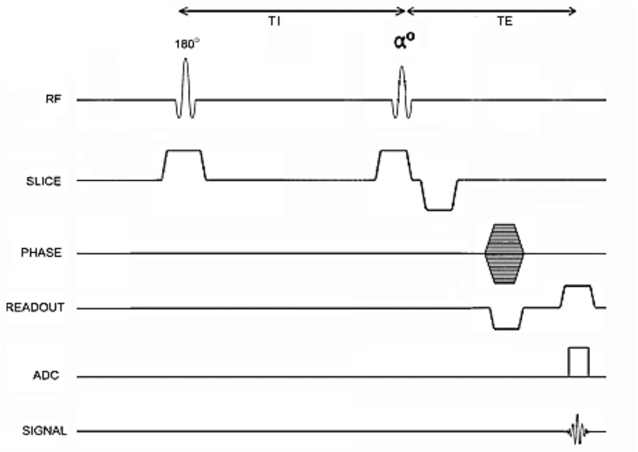

MPRAGE representation in pulse diagram, one single readout is shown. TE: time of echo; TI time of inversion.

EPI

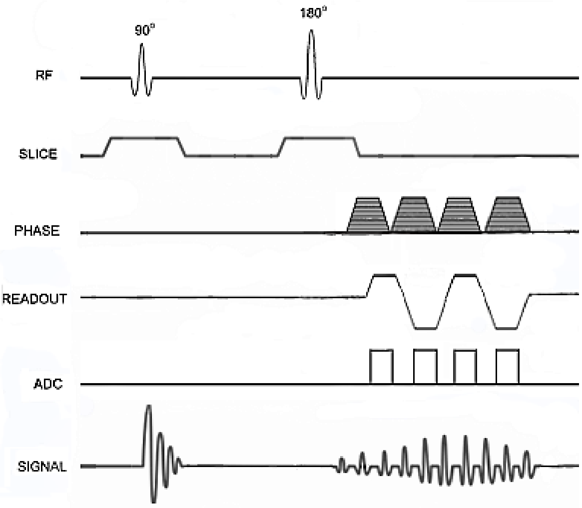

General EPI pulse diagram. The sequences can be slightly modified, by means of other gradients, maintaining its fast imaging feature. Adapted from Lippincott Williams & Wilkins, 2010.

A.6 Tensor imaging, Rician noise correction

DWI relies on physics and mathematics. A series of useful definitions can be found more in detail in literature (see Kingsley, 2006). Here brief concepts are reported for better understanding mertics obtained in this work.

Tensor can be calculated from data acquired by means of sensitizing diffusion gradients in six or more directions. There are two approaches, named B and H matrix extraction: once the tensor is represented as a vector, matrices can extract the apparent diffusion coefficient. The B matrix approach combines the different signal intensities from b directions set, and includes the signal noise vector. The H matrix approach includes normalized gradient components inside, and ADC can be directly calculated from encoding schemes without considering the tensor elements. Either B and H, when weighted by means of least squares, treat their points as acquired accurately. The B matrix approach is more powerful because yield a covariance matrix to optimize DTI parameters, and because the signal decay is non mono-exponential. B results more flexible than H. H matrix method, when b values are more than 6, brings to a non-squared matrix, and the estimate from b=0 average signal is already incorporated inside, meaning that weighted least square fit is not possible because b = 0 images can not be fitted separately.

In both cases, linear least squares fit can be calculated, but noise in DTI data is not fully described by errors. The definition of noise relies in the deviation of a measured variable. Types of noise are round-off errors, lower than acquired values because dependent from digitized signal (voltage). Scatter and variance occurs in biological samples, because of heterogeneity of the object. Other source of errors are introduced from raw data when computed into parameters, such as absorption and dispersion signal.

This means that noise has a magnitude that exihibits a distribution, called Rician, (Dietrich O, Heiland S, Sartor K. 2001; Gudbjartsson and Patz, 1995) and it is taken in account in diffusion anisotropy and respective metrics.

Because biological tissues has also self-diffusion processes, all models used to compute tensor, or diffusion anisotropy indices, are dependent from b factors. Thus the chosen gradient sampling scheme can affect the diffusion values in the obtained images. In this study, noise level were higher and needed further computations to label signals as specific. A future milestone in DWI could be new computational methods myelin fraction, intra-extra axonal signal fractions in diffusion images.

A.7 Table of anatomical regions in mouse brain and abbreviations

A) **Mouse brain regions (*Amg – IP*)**		***A)*** **Mouse brain regions (*lo – vgtx*)**	
Abbreviation	**Long nomenclature**	**Abbreviation**	**Long nomenclature**
Amg	Amygdala	*lo*	Lateral olfactory tract
abv	Arbor vitae of cerebellum	*LSC*	Lateral septal complex/nucleus
aca	Anterior part commissure	*MB*	Midbrain
Acb	Nucleus accumbens	*mlf*	Medial longitudinal fasciculus
acp	Posterior part commissure	*MC*$^{+}$	Motor cortex
Au^{+}	Auditory cortex	*MO*	Medulla oblongata
BF	Basal Forebrain	*MSC*	Medial septum
BNST	Bed nucleus of stria terminalis	*mt*	Mammillothalamic tract
cb	Cerebellum	*OL*	Occipital lobe
Cg	Cingulate anterior	*Olf*	Olfactory bulb
cp	Cerebral peduncle	*opt*	Optical tract
Cpu	Caudate putamen	*PAG*	Periacqueductal grey
Cu	Cuneate nucleus	*Pas*	Parasubiculum
DG	Dentate gyrus	*Pir*	Piriform cortex
Enth	Enthorinal region	*Pn*	Pontine nucleus
fi	fimbria	*Pons*	Pons
Fro	Frontal lobe	*Ptl*	Parieto temporal lobe
Fs	Fundus of striatum	*RC*	Rhinal cortex
fx	fornix	*RS*	Retrosplenial cortex
GP	Globus Pallidus	*SC*	Superior colliculus
GrDG^{+}	Granular layer DG	*sm*	Stria medullaris
hbc	Habenular commissure	*SOIC*	Superior olivary complex
Hi	Hippocampus	*Ss*$^{+}$	Somatosensory cortex
Hy	Hypotalamus	*st*	Stria terminalis
IC	Inferior colliculus	*Th*	Thalamus
IO	Inferior olivary complex	*Tu*	Olfactory tubercle
IP	Inferior cerebellar peduncle	*vgtx*	ventral tegmental area

***B)* Anatomical location**			
GM	**WM**	**Brainstem**	**Cerebellum**
Amygdala	Anterior part of anterior commissure	Inferior colliculus	Arbor vita of cerebellum
Basal Forebrain	Posterior part of the posterior commissure	Superior colliculus	Cerebellar cortex
Bed nucleus of stria terminalis	Posterior commissure	Corticospinal tract/pyramid	Inferior cerebellar peduncle
Caudate/putamen	Cerebral peduncule	Cuneate nucleus	Middle cerebellar peduncle
Enthorhinal area	Corpus callosum	Inferior olivary complex	
Frontal lobe	Fasciculus retroflexus	Medial lemniscus/medial lonngitudinal fasciculus	
Occipital lobe	Fimbria	Pontine nucleus	
Dentate gyrus of hippocampus	Fornix	Superior olivary complex	
Fundus of striatum	Habenular commissure	Periaqueductal grey	
Globus pallidus	Internal capsule	Medulla	
Hippocampus proper	Mammillothalamic tract	Midbrain	
Hypothalamus	Optic tract	Pons	
Lateral septal complex	Stria medullaris	Interpeduncular nucleus	
Mammillary bodies	Stria terminalis	Ventral tegmental decussation	
Medial septal complex			
Nucleus accumbens			
Pre-post parasubiculum			
Striatum granulosum of hippocampus			
Thalamus			

Acknowledgments

My sincere gratitude goes to Prof. Marzola for her patience, support and immense knowledge during these past three years. I am extremely grateful towards Mariotti's and Constantin group in Verona, for their contribution and collaboration.

Besides my advisor, I would like to thank the rest of department of Anatomy Department in the University of Verona, for continuous support in my research, as well as prof. Pot, prof. Merkler and Dr. Daducci that provided me the opportunity to join their team as intern in Switzerland, and gave me the possibility to access research facilities.

Publications

Cisterna, B.; Boschi, F.; Croce, A. C.; Podda, Rachele; Zanzoni, S.; Degl'Innocenti, D.; Bernardi, P... 2018. *Ozone treatment of grapes during withering for Amarone Wine: a multimodal imaging and spectroscopic analysis.*
Microscopy and microanalysis-ISSN:1431-9276, vol. 24 (5), pp.564-573. DOI:10.1017/S1431927618015209.

Barbara Cisterna, Federico Boschi, Anna Cleta Croce, Rachele Podda, Serena Zanzoni, Daniele Degl'innocenti, Paolo Bernardi, Manuela Costanzo, Pasquina Marzola, Viviana Covi, Gabriele Tabaracci, Manuela Malatesta (2018) *Imaging techniques for the evaluation of grapes in withering for amarone wine production.* published contribution http://ilasl.org/index.php/Incontri/article/download/436/412

Rachele Podda, Pietro Bontempi, Alessandro Daducci, Nicolo Sonato, Marta Balietti, Patrizia Fattoretti, Silvia Fiorini, Stefano Tambalo, Flavia Merigo, Pasquina Marzola (2020) *Brain aging investigation in an experimental rodent model of late life: a multi-level MRI characterization at 4.7 T* in preparation